ECAP-2012-027

Time-resolved and position-resolved X-ray spectrometry with a pixelated detector

Zeitaufgelöste und ortsaufgelöste Röntgenspektrometrie mit pixeliertem Detektor

Der Naturwissenschaftlichen Fakultät
der Friedrich-Alexander Universität
Erlangen-Nürnberg

zur

Erlangung des Doktorgrades

Dr. rer. nat.

vorgelegt von

Peter Sievers
aus Nürnberg

FRIEDRICH-ALEXANDER
UNIVERSITÄT
ERLANGEN-NÜRNBERG
NATURWISSENSCHAFTLICHE
FAKULTÄT

PTB

ERLANGEN CENTRE
FOR ASTROPARTICLE
PHYSICS

Als Dissertation genehmigt
von der Naturwissenschaftlichen Fakultät
der Friedrich-Alexander Universität Erlangen-Nürnberg

Tag der mündlichen Prüfung:	07.12.2012
Vorsitzender der Promotionskommision:	Prof. Dr. Johannes Barth
Erstberichterstatter:	Prof. Dr. Gisela Anton
Zweitberichterstatter:	Prof. Dr. Reinhold Müller

Contents

1 Introduction **1**

2 Detector simulation **5**
2.1 Necessity of simulation 5
2.2 Implemented detector setup 6
2.3 Innovations on the simulation tool 7
2.3.1 Detector geometry 7
2.3.2 Detector physics 9
2.4 Verification of simulation 11

3 Spectrometry **17**
3.1 Introduction to the reconstruction method 17
3.2 Position-resolved spectrometry 41
3.2.1 Pixel-by-pixel energy calibration and anode heel effect . 41
3.2.2 Improved global energy calibration 59
3.2.3 Further impacts of a pixel-by-pixel energy calibration . . 60
3.2.4 Spectrometric imaging 65
3.3 Time-resolved spectrometry 67

4 Summary and outlook **81**

Zusammenfassung und Ausblick **85**

A Tabulated Values **89**

B Source code **91**

Bibliography **95**

Danksagung **103**

List of abbreviations and acronyms

Ag	silver
Au	gold
^{241}Am	Americium-241
ASIC	Application-Specific Integrated Circuit
Cu	copper
DAC	Digital Analogue Converter
ECAP	Erlangen Centre for Astroparticle Physics
E_i	Energy of the i-th channel
Gd	gadolinium
GSL	Gnu Scientific Library
GUI	Graphical User Interface
hpGe	high-purity germanium
M_i	Number of counts in the i-th channel od the measurement corresponding to the energy E_i
Mo	molybdenum
NaI	sodium iodine
PCB	Printed Circuit Board
PTB	Physikalisch-Technische Bundesanstalt
ROI	region of interest
ROSI	ROentgen SImulation (German for X-ray simulation)
Si	silicon
SDD	Silicon Drift Detectors
Sn	tin
T_i	Number of photons in the i-th channel of the impinging spectrum corresponding to the energy E_i
THL	energy threshold
THL scan	threshold scan, a sampling of the deposited energy in the sensor by sweeping the energy threshold (THL)
ToA	Time of Arrival
ToT	Time over Threshold
UBM	Under-Bump Metallization
Y	yttrium

1 Introduction

Scientific background

Energy-dispersive spectrometers [FA70] for X- and γ-radiation employing different kinds of sensor materials are widely used, for instance in the determination of X-ray tube spectra, synchrotron light spectra, radioactive material composition, and in astronomy. All those fields of research have in common that the highest achievable energy resolution is preferred but already the requirements on the minimal count rate differ for the mentioned applications. For instance, in the field of radioactive material detection and identification a very low photon flux of $10\,/(\mathrm{s\,cm^2})$ for the Americium-241 (^{241}Am) isotope has to be sufficient [Ans] and, on the other hand, in the field of clinical X-ray tubes the typical photon flux is at about $5 \times 10^9\,/(\mathrm{s\,cm^2})$ (derived from [Bfs03]). Also the demand for the energy range depends on the application of interest – for example: 10 keV to 150 keV in the field of medical imaging, 8 keV to 420 keV in the field of non-destructive-testing [BB93], and 0.35 keV to 2.5 keV in extraterrestrial X-ray astronomy with XMM-Newton [BA+98]. Thus, for energy sensitive measurements different kinds of detectors are used depending on the application and its requirements, for instance scintillator detectors [Mos03] (e.g. CsI(Na) or NaI(Tl)), and semiconductor detectors made of e.g. high-purity germanium (hpGe) [Kha11], CdTe [RS92], or silicon (Si) [LE+96].

Semiconductor detectors are applied in a variety of applications. Their working principle is as follows [Kha11]: A primary particle (photon, electron etc.) being absorbed in the sensor material releases a secondary electron and eventually other secondary particles like Compton photons. Each secondary electron deposits its energy by generating electron-hole pairs along its path in the sensor as long as the energy of this electron is sufficient. By applying a bias voltage, those electron-hole pairs are separated and drifted towards the electrodes of the detector. If the secondary electrons, other secondary particles, and the primary particle do not exit the sensor volume, the overall deposited energy and thus the total energy of the primary particle can be determined from the amount of the released charge. In general, there is the probability that a secondary particle or the primary particle may leave the sensor volume. In such a case the energy of the primary particle would only be partly deposited in the sensor volume. To gain the best in energy resolution, it is desirable that any released secondary particle and the primary particle remain inside the sensor volume.

The detection of each secondary particle is not always feasible. Additionally, the absorption probability of the primary particle – e.g. photons – in the sensor is decreasing with increasing energy. This has the result that the measured energy distribution may differ from the energy distribution of the primary particles. If both the absorption probability and the amount of secondary particles exiting the sensor volume are known for each primary particle in the desired energy range, one can model the energy response of the detector. The measured energy distribution can then be corrected for the energy response – resulting in the energy distribution of the primary particles.

For the detection of photons in the energy range of medical X-ray tubes used for diagnostics (energies from 10 keV to 150 keV) the most common spectrometers are hpGe semiconductor detectors. For reducing electronic noise due to thermal excitation of valence electrons, hpGe detectors have to be cooled with liquid nitrogen to a temperature of 77 K. For measurements presented in this thesis, a cylindrical hpGe detector with a diameter of 25 mm and a thickness of 13 mm has been used. Typical values for the maximal count rate of such a device are about 200 kHz which corresponds to an air kerma rate[1,2] (a measure of the photon flux) of 92 µGy/h. This is a relatively low rate capability compared to typical air kerma rates of 300 µGy/h. Thus, a collimator has to be used for reducing the flux. As a positive effect, the collimation ensures that only the central area of the sensor is hit which minimizes the probability of secondary particles exiting the sensor volume.

In a pixelated detector operated at the same radiation flux, the photons are spread over many pixels of relatively small areas each, and thus, a lower count rate in each pixel is obtained. Considering a detector layout with 256 x 256 pixels, and a pixel pitch of 55 µm, a count rate of 50 kHz per pixel[2] corresponds to an air kerma rate[1] of 3.8 Gy/h. Thus, there is no need to collimate. On the other hand, for such a kind of detector the distribution of the deposited energy differs significantly from the energy distribution of the impinging photons. This is due to processes in the sensor layer – as: Compton scattering of photons or electrons which may then be absorbed in a different pixel, diffusion of the generated charge beyond pixel boundaries, and absorption of fluorescence photons.

The pixelated detectors used in this work – mainly the Timepix detector – are part of the Medipix family. They are being developed in a collaboration of several

[1] The maximum count rate is up to 200 kHz [Ort] which equals a flux of 40 kHz/cm^2. Such a flux corresponds – for the radiation quality N-40 – to an air kerma rate of 92 µGy/h [Ank00].

[2] Theses rates are only theoretical values due to the analogue pile-up, which reduces the maximal count rate.

universities and research institutes worldwide lead by CERN [Med]. From the initial Medipix detector the Medipix2 detector and the Medipix3 detector have now emerged with each increasing functionality. Based on the Medipix2 detector, the Timepix detector has been developed, which has in addition to the pure photon counting mode, two modes for measuring an event time. The Medipix development emerged from the development of detectors used at the Large Hadron Collider into an application for – as the name already indicates – medical imaging. Nowadays the detectors are used in a wide range of applications [Cam11] – for instance: medical imaging, material analysis, nuclear power plant decommissioning, as a photo-tube for optics, in education, and finally again for high energy particle physics. Additionally, in the work presented here the Timepix detector was used for spectrometry.

Objective of research

For the Timepix detector the measured distribution of the deposited energy differs significantly from the energy distribution of the impinging photons. Thus, the measured distribution has to be corrected for the energy response of the detector. The aim of this PhD work was to extend and improve the analysis and deconvolution methods presented in [TT11] in such a way that it enables the possibility of performing both position-resolved and time-resolved spectrometric measurements with the Timepix detector. In this context, the difficulties arose from the small volume of each single detection element – a pixel – and associated with this the low detection efficiency resulting in a low number of counting events. The research has been carried out in collaboration with the Erlangen Centre for Astroparticle Physics (ECAP) and the Physikalisch-Technische Bundesanstalt (PTB) – Department 6.3 (Radiation Protection Dosimetry) and Department 6.2 (Dosimetry for radiation therapy and diagnostic radiology).

Outline of the thesis

Due to the complexity in the spectrum of deposited energy, there has been until now no convenient way of modelling the energy response of the Timepix detector analytically. An attempt of an analytic model for the energy deposition spectrum is given in [UHJ10]. This model neglects fluorescence photons emerging from detector parts and scattering effects and thus seems insufficient for my work. As a solution the detector was implemented in a simulation. The effects of ionization and electron-hole-pair production in the sensor are very well understood and one can simulate them with Monte Carlo methods [Gie; GD08]. Furthermore, with a set of models for the drift [JCOA77], diffusion and repulsion [Kor07]

of the released charge carriers, the distribution of energy deposition can be described. The necessary improvements and adaptions I have made are explained in section 2. After verification of the improvements, I was able to simulate the energy deposition – the detector response (or response function) – at different energies.

With a precisely simulated energy response function one can then calculate the impinging X-ray spectrum by deconvolving the measured energy distribution [MTT+09; TTM+09]. Formerly, two methods – spectrum stripping and pseudo matrix inversion – have been used for energy reconstruction. Both methods suffer from two disadvantages, which I had to solve: The solution of the deconvolution may deliver negative intensities for certain energy channels of the calculated impinging spectrum – this does not make sense physically. Additionally, those methods imprinted strong oscillations – depending on the chosen width of the energy channels – on the deconvolved spectrum. The improvements and results I achieved by employing a different deconvolution method based on Bayesian statistics are shown in section 3.1.

My next aim was to make use of the pixelation of the detector for gaining position-resolved spectra. One application was the measurement of the angular dependency of the anode heel effect[3]. With respect to the measuring time, the photon fluence in each chosen region of interest (ROI) on the pixel matrix was relatively low. Thus, I had to cope with the requirement of dealing with low statistics in the measured data. Furthermore, I had to correct for a drift in the energy response of the Timepix detector along the columns of the pixel matrix. The results and the success of this investigation will be demonstrated in section 3.2.

In contrast to standard hpGe detectors, the Timepix detector has the possibility of delivering timing information of each photon even at high photon flux, as each pixel is operated separately. I have used this feature to measure the change over time of the spectrum emitted while the radiation source was switched on – for both a conventional X-ray tube used for continuous radiation fields and a novel X-ray tube installed at PTB used for pulsed radiation fields. The corresponding results are presented in section 3.3.

[3]The angular-dependent absorption of the generated photons inside the anode of the X-ray tube.

2 Detector simulation

Contents

2.1 Necessity of simulation 5
2.2 Implemented detector setup 6
2.3 Innovations on the simulation tool 7
2.3.1 Detector geometry 7
2.3.2 Detector physics 9
2.4 Verification of simulation 11

2.1 Necessity of simulation

The energy of a photon impinging on a semiconductor detector is determined by measuring the released charge inside the sensor. For spectrometric measurements very accurate detectors in the sense of this energy deposition have to be used. For the Timepix detector [LB+07] (details in appendix, table A.1 and A.2) used in this work this is not guaranteed. A schematic diagram of the detector setup including the sensor layer, the bump-bonds, and the Application-Specific Integrated Circuit (ASIC) is shown in figure 2.1. As shown in figure 2.2 for the impinging radiation of ^{241}Am, the spectrum of the deposited energy in the Si sensor is distorted. This is mainly due to effects like charge-sharing, Compton

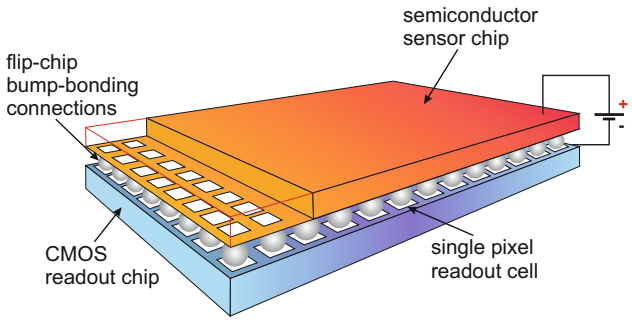

Figure 2.1 Schematic diagram of a Timepix detector – including sensor layer, CMOS readout (ASIC), and as their interconnection the bump-bonds (drawing by Jana Klammer).

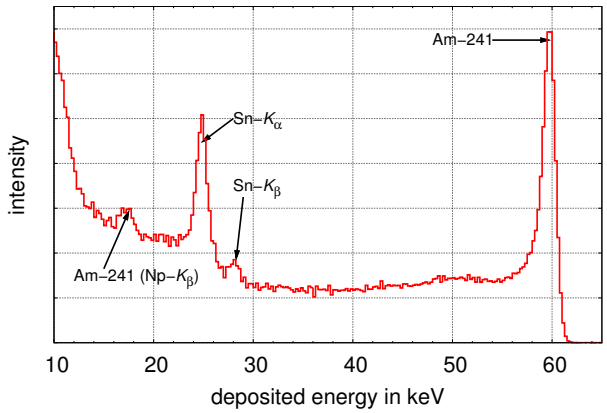

Figure 2.2 Measured distribution of deposited energy for radiation of a ^{241}Am radioactive isotope.

scattering, and absorption of fluorescence photons generated in detector parts (e.g. tin (Sn) of the bump-bonds). These interaction processes of photons with the sensor material are described in detail in [Pod10, chapter 7] and the implementation for the simulation in [Dur08, chapter 5]. Due to this misassignment of energies the impinging spectrum cannot be measured directly and has to be calculated by the deconvolution of the measured data. This is done with a set of monoenergetic response functions. As there is so far no convincing way of modelling them analytically, they have to be simulated. For performing the necessary simulations the Monte Carlo framework ROentgen SImulation (ROSI) [GD08; Dur08] facilitating EGS4 [NHR85] and LSCAT [NH00] has been used. The setup, applied improvements, and comparative measurements will be shown in the following sections.

2.2 Implemented detector setup

For implementing the Timepix detector in the simulation framework ROSI the recently developed C++ class for photon counting detectors has been used. The development and implementation of this detector class was the subject of a PhD thesis by [Dur08]. Table 2.1 and an output of the Graphical User Interface (GUI) (figure 2.3) provide insight on all parts of the detector that have been implemented in the simulation. All layers mentioned have an extra spacing of 1 µm between each of them, to avoid an overlap of materials due to precision limitations in C++. The sensor layer consists of a guard ring (560 µm)

detector part	material	size (W x H x D)/ mm^3
sensor layer	Si	15.2 x 0.303 x 15.2
bump-bond layer	Sn96.5Ag3.5	14.1 x 0.027 x 14.1
ASIC	Si	14.1 x 0.75 x 14.1
ASIC ground plate	copper (Cu)	14.1 x 0.0175 x 14.1
Printed Circuit Board (PCB)	FR-4	79 x 2 x 47

Table 2.1 Implemented detector setup.

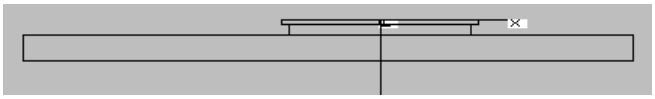

Figure 2.3 Output of the GUI for the implemented detector setup – showing (from top to bottom) the sensor layer, the ASIC, and the PCB.

and two passivation layers (2.8 µm each) at the top and bottom. Thus, only the inner area 14.1 mm x 297.4 µm x 14.1 mm is the effectively used sensitive volume with an applied pixel pitch of 55 µm. The bump-bonds are implemented in the following way: Firstly, a solid block of the bump-bond material is created; secondly, 256 vacuum strips are cut out of it in both the x-direction and the y-direction – resulting in 65 536 rectangular bump-bonds.

2.3 Innovations on the simulation tool

2.3.1 Detector geometry

In a first step the rectangular implementation of the bump-bonds has been replaced with spherical ones. Unfortunately those complex geometries raised the computation time by a factor of ten. This is due to the fact that for each propagation step of a photon the distance to every geometric object inside the simulated world is calculated. As those circular ones have to be set one by one, the number of elements is extended to 65 536 bump-bonds – formerly they could be set by cutting out 512 bars out of a big block of bump-bond material (513 objects). For lowering the computation time back to the normal extent, some changes had to be made to the detector class. A hierarchical multilevel approach of placing the bump-bonds was chosen (table 2.2): In level 1 a set of four-by-four bump-bonds is summarized to a virtual medium – called composite medium. 16 groups of level 1 are then again summarized to a further composite medium –

level	content	size
1	bump-bond	16
2	level 1	16
3	level 2	16
4	level 3	4
5	level 4	4
number of distances (sum of sizes)		56
number of bump-bonds		65 536

Table 2.2 Hierarchical order for placement of bump-bonds.

level 2. This is repeated (with different grouping sizes) until level 5 is reached, resulting in four final composite mediums. Therefore the number of distance calculations was lowered to 56 again. This improves the computation time down to the originating one. Thus, it is now possible to model arbitrary geometric objects as bump-bonds – depending on what fits best to reality.

Secondly, to gain an implementation close to reality more complex geometries of bump-bonds are necessary. Thus, the C++ class for photon counting detectors has been extended for dealing with a new bump-bond class. This new C++ class is in fact a derived class of the composite medium class. This means, instead of positioning a spherical bump-bond (or any other object), an instance of this bump-bond class is set in place. It is now even possible to easily include further materials connected to the bump-bonds. For gaining an electric conductance it is necessary to place electrical contacts on both the sensor and the ASIC. Those contacts are called Under-Bump Metallization (UBM). Thus, a most realistic implementation including the UBM was aimed at. The source code of a bump-bond used in the simulation is shown in (appendix B.1). A comparison of a cross section of the bump-bonds with the ones implemented in the simulation is shown in figure 2.4. By comparing both figures, this newly gained accuracy in implementation of the bump-bonds in the simulation becomes clearly visible. It is now even possible to implement special bump-bonds like so-called copper-pillars as has been already done for the Dosepix detector [WA+11] which is intended for dosimetry applications [MB+09].

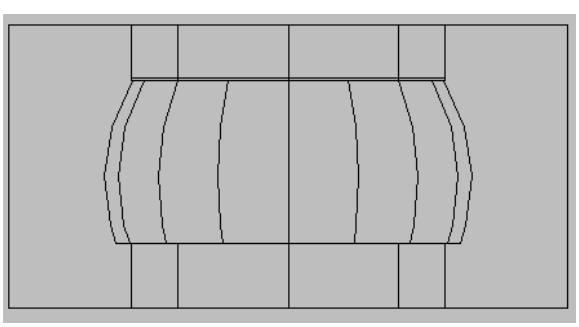

(a) Zoom onto a bump-bond shown in the GUI.

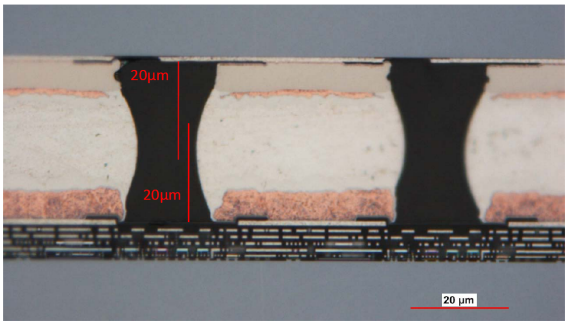

(b) Cross section of a chip assembly of the type used. (private communication with Xavier Llopart)

Figure 2.4 View of the bump-bonds – implemented in the simulation (a) and visible in a cross section (b). The main parts are (from top to bottom): sensor (only in b), top UBM (Ni and thin Cu layer), the bump-bond (SnAg), bottom UBM (Cu), and ASIC (only in b).

2.3.2 Detector physics

Not only the geometry implementations but also some physical aspects of the simulation especially for the transport of the generated charge carriers in the sensor, had to be optimized. The following is, in particular, only valid for silicon used as a sensor material. The drift time t_{drift} is now calculated by numerical integration of the velocity of the drifting charge carrier v_{Q} [JCOA77; Kor07]:

$$v_{\text{Q}}(d) = \mu_0 \cdot E(d) \cdot \left(1 + \left(\frac{\mu_0 \cdot E(d)}{v_{\text{max}}}\right)^{\beta}\right)^{-\frac{1}{\beta}}, \tag{2.1}$$

under consideration of the maximal drift velocity v_{max}, charge carrier mobility μ_0, temperature-dependent exponent β, actual distance to electrode d, and the electrical field strength E:

$$E(d) = \frac{U_{\text{bias}} + U_{\text{depletion}}}{h} - 2 \cdot d \cdot U_{\text{depletion}} \cdot h^{-2}, \tag{2.2}$$

with the applied bias voltage $U_{\text{bias}} = 150\,\text{V}$, the depletion voltage $U_{\text{depletion}}$ of the sensor, and the sensor thickness h. Absolute values are given in table A.3. With the given values, the differences in drift time are shown in figure 2.5 for both neglecting and considering the saturation velocity for both types of charge carriers. It is clearly visible that the saturation velocity has a significant influence

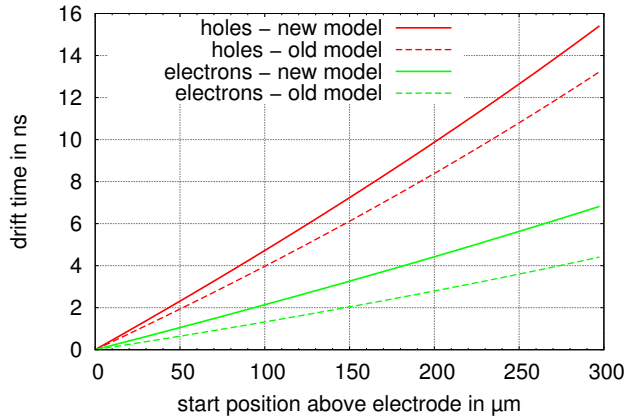

Figure 2.5 Drift times of charge carriers depending on their starting position above the electrode for both electrons (green line) and holes (red line). Solid lines for the new drift time model, dashed lines for the old one.

on the drift time and thus should not be neglected – as it has been done until now.

Furthermore, I partly had to dismiss the formerly introduced cylindrical model for the repulsion of the drifting charge carriers [Kor07]. The implementation of these two models – cylindrical and spherical – is described in detail in [Dur08, section 6.6]. The maximum radius for the cylindrical model is defined by:

$$r_{\text{cyl}}\left(t_{\text{drift}}, q\right) = \sqrt{\frac{\mu_0}{\pi\epsilon\epsilon_0}\frac{q}{l}t_{\text{drift}}}, \tag{2.3}$$

and for the spherical model:

$$r_{\text{sphe}}\left(t_{\text{drift}}, q\right) = \sqrt[3]{3\frac{\mu_0}{4\pi\epsilon\epsilon_0}qt_{\text{drift}}} \tag{2.4}$$

with the generated charge q, the length l for the track of the secondary electron, the permittivity ϵ, and the drift time t_{drift}. These two models describe the repulsion of the charge carriers depending on the track length of the secondary electron (generated by ionization) between two interaction points in the sensor. The longer and straighter the track, the less the probability that the generated charge is influenced by the charge of neighbouring parts of the same track. This is then expressed with the cylindrical model. The shorter and therefore the less straighter the tracks, the more the generated charge is influenced by neighbouring parts of one track. This is then expressed with the spherical model. As the

track length and straightness are correlated with the energy of the secondary electron, the decision of which model to use is made by the energy. Until now there has been a change of the model at a threshold energy $E = 10\,\mathrm{keV}$ of the secondary electron. Below this threshold the spherical model was used, above the cylindrical one. For silicon as a sensor material, this value had to be raised to $E = 40\,\mathrm{keV}$ which actually dismisses the cylindrical model for most cases being analyzed. This threshold energy has been determined empirically by comparing the simulated data to measured ones. This higher value shows that the influence between the charge of the neighbouring tracks was formerly underestimated.

2.4 Verification of simulation

To show the impact of those improvements mentioned, there had to be a dedicated setup to guarantee the reproducibility and comparability for both measurement and simulation. Such a setup is shown in detail in figure 2.6. As the fluorescence target a gadolinium (Gd) foil, irradiated with a 125 kV-tungsten spectrum, was chosen. Figure 2.7 shows the different detector responses simulated for the four stages in improvement of the simulation tool. The starting point is the simulation with quadratic bump-bonds, non-saturated drift velocity and the old threshold energy for the change of the repulsion model (red line). By introducing the new

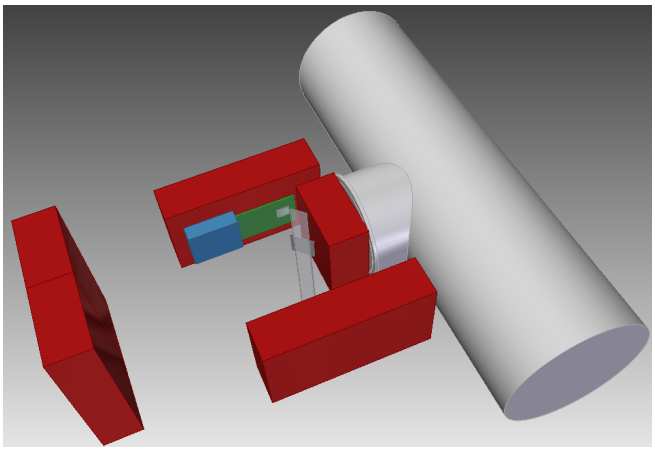

Figure 2.6 Setup for comparison of measurement and simulation. All dimensions are in scale. Indicated parts: X-ray tube in grey, lead shielding in red, the transparent fluorescence target holder, the fluorescence target in silver, USB-readout in blue (not included in the simulation), the PCB in green and finally the detector on the PCB in silver.

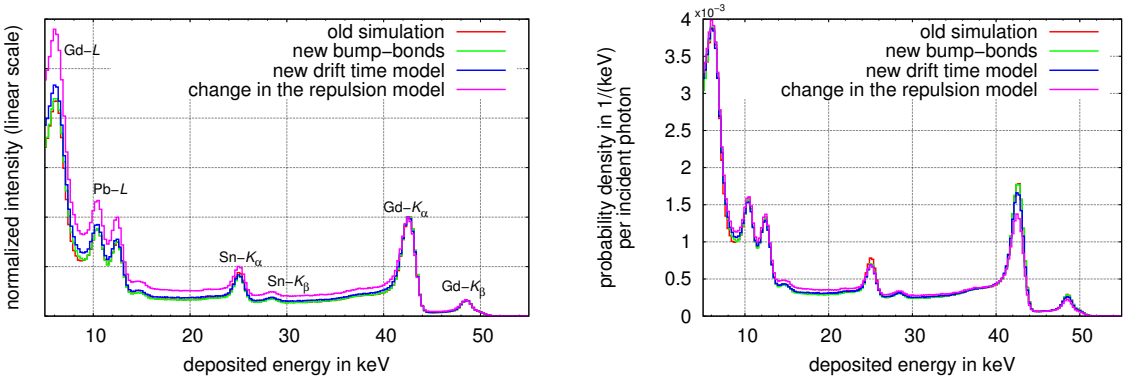

(a) Normalized intensity.

(b) Probability density of energy deposition.

Figure 2.7 Comparison of the distribution of deposited energy for the four improvement stages of the simulation for Gd-fluorescence lines excited by a 125 kV-tungsten spectrum. The curves of figure (a) have been normalized to the full energy peak at $E \approx 42\,\mathrm{keV}$.

bump-bonds, the representation of its fluorescence lines (Sn$-K_\alpha$ and Sn$-K_\beta$) is improved (green line). Furthermore, by considering the saturation velocity of the charge carriers, the charge-sharing content in the energy deposition was extended (blue line) – but still not to the desired amount. By introducing a saturated drift velocity, the drift time is longer and thus the charge carriers have more time to diffuse and to repulse which increases the charge sharing. As a fourth stage, the switching between the two repulsion models was changed to an appropriate threshold (magenta line) which increases the charge sharing to the desired amount.

For comparing those results to a measurements[1] the relative deviance d of the simulated detector response R and the measurement M as a function of the deposited energy E – after normalizing each to the full energy peak at $E \approx 42\,\mathrm{keV}$ – was calculated for all four improvement stages by:

$$d\,(E) = \frac{M\,(E)_{\mathrm{norm.}} - R\,(E)_{\mathrm{norm.}}}{M\,(E)_{\mathrm{norm.}}}. \tag{2.5}$$

In figure 2.8 it is clearly visible that the detector response of the last improvement stage shows the lowest deviations and is in the range of $-50\,\% < d\,(E) < 20\,\%$. The good agreement of this last improvement stage and the measurement is also shown directly for the detector response in figure 2.9. The higher intensity in the

[1] The measurements shown in this chapter were derived after applying a pixel-by-pixel energy calibration – described on page 45ff – on the detector.

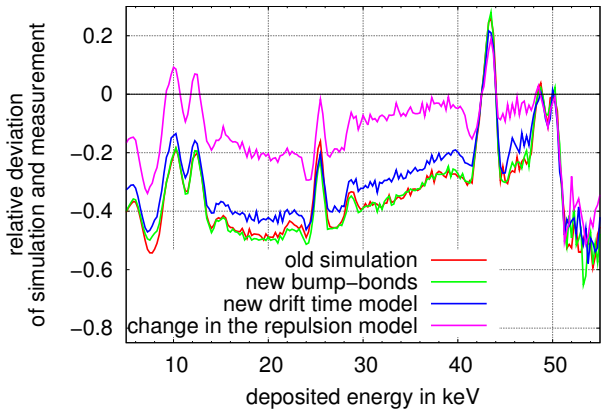

Figure 2.8 Relative deviance of the simulated detector response for all four improvement stages compared to the measurement as a function of the deposited energy.

measurement for the fluorescence lines of Gd$-L$ is due to electronic noise that occurs for the lower energies. For a further analysis and for excluding scattering effects on components in the laboratory, the measurement and simulation of the scattering background have been performed for a similar setup as shown in figure 2.6 but without the PMMA target holder and without the target itself. Taking the difference of the complete measurement (figure 2.9a) and the background results in the energy deposition shown in figure 2.9b. Again it shows a good agreement between simulation and measurement. Those agreements provide assurance that all necessary parts producing scattering are implemented correctly in the simulation.

For a more quantitative analysis of the differences between measurement and the four stages of simulation, the relative intensities of the three most prominent peaks (Gd$-K_\alpha$, Sn$-K_\alpha$ and Sn$-K_\beta$) have been analyzed. Therefore the areas of these peaks above the background have been calculated. The determined background level and its resulting areas are, for instance, indicated in figure 2.10. The relations of all three indicated peaks are then summarized and compared in table 2.3. Looking at the relation of areas for $\frac{\mathrm{Sn}-K_\alpha}{\mathrm{Sn}-K_\beta}$ it clearly shows the positive tendency along the improvement stages towards the values of the measurement. This is also visible in the decreasing relative deviation compared to the measurement. The values for both relations, $\frac{\mathrm{Gd}-K_\alpha}{\mathrm{Sn}-K_\alpha}$ and $\frac{\mathrm{Gd}-K_\alpha}{\mathrm{Sn}-K_\beta}$, initially show a worse tendency after introducing the new bump-bonds, but on finishing all improvement steps a very small deviation between simulation and measurement

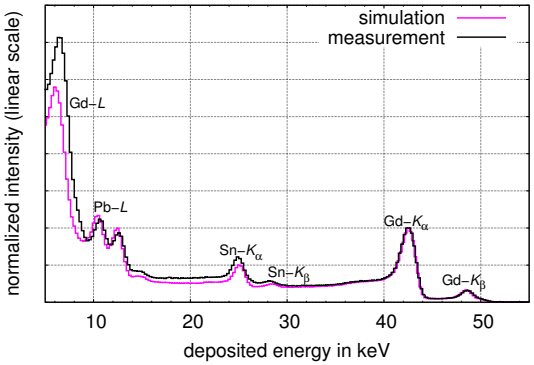

(a) Total deposition spectrum.

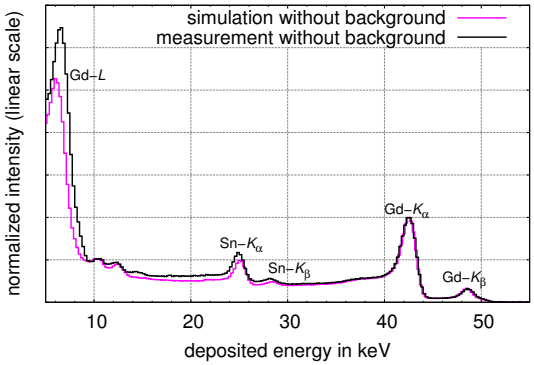

(b) Deposition spectrum, corrected for scattering background.

Figure 2.9 Comparison of the distribution of deposited energy derived by measurement and simulation for Gd-fluorescence lines excited by a 125 kV-tungsten spectrum. Figure (a) shows the distributions derived with the complete setup (figure 2.6) and figure (b) the distributions corrected for the scattering background.

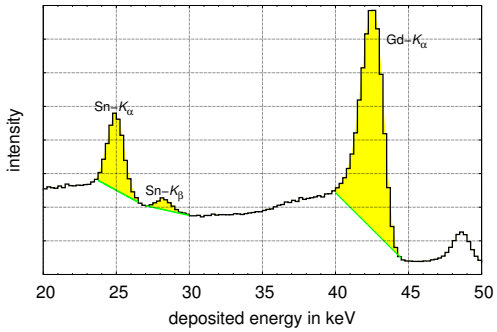

Figure 2.10 Indication of the different areas chosen for quantitative analysis.

	$\frac{\text{Sn}-K_\alpha}{\text{Sn}-K_\beta}$		$\frac{\text{Gd}-K_\alpha}{\text{Sn}-K_\alpha}$		$\frac{\text{Gd}-K_\alpha}{\text{Sn}-K_\beta}$	
	abs.	rel.	abs.	rel.	abs.	rel.
old simulation	5.9	−19 %	4.7	15 %	28	−6.4 %
new bump-bonds	6.2	−14 %	5.5	34 %	34	16 %
new drift time	6.4	−11 %	5.6	35 %	35	21 %
new repulsion	6.9	−4.4 %	4.7	13 %	32	8.4 %
measurement	7.2		4.1		29	

Table 2.3 Relative intensities of the three different peaks for the fluorescence-lines of Gd$-K_\alpha$, Sn$-K_\alpha$, and Sn$-K_\beta$ and their relative deviations compared to the measurement.

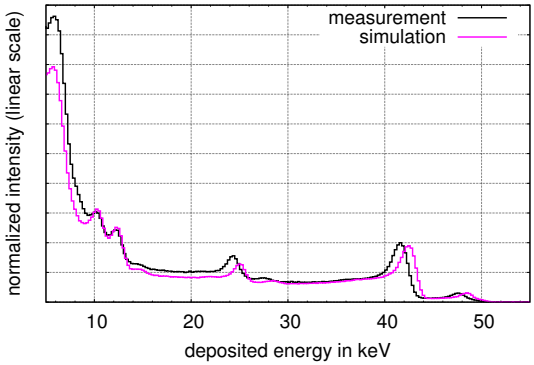

(a) Bias voltage: $U_{\text{bias}} = 75\,\text{V}$.

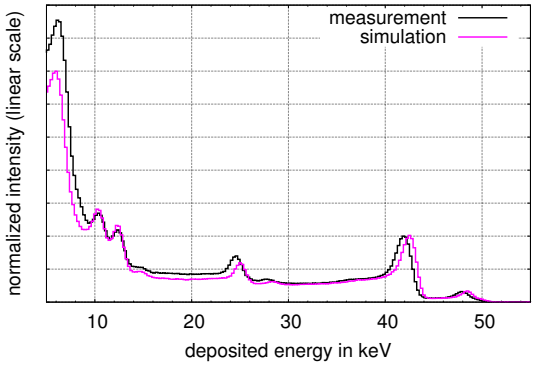

(b) Bias voltage: $U_{\text{bias}} = 100\,\text{V}$.

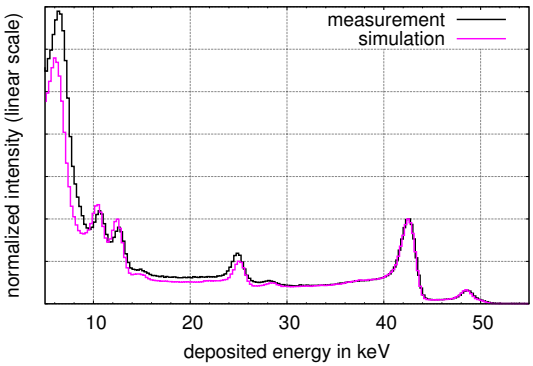

(c) Bias voltage: $U_{\text{bias}} = 150\,\text{V}$ (standard).

Figure 2.11 Comparison of the distribution of deposited energy derived by measurement and simulation for Gd-fluorescence lines excited by a 125 kV-tungsten spectrum at different bias voltages: $U_{\text{bias}} = 75\,\text{V}$ (a), $U_{\text{bias}} = 100\,\text{V}$ (b), $U_{\text{bias}} = 150\,\text{V}$ (c).

could be reached. Finally, all deviations for all three relations shown are at the same magnitude.

As both the drift time model and the threshold energy for the repulsion model have been changed, it was necessary to validate those new implementations. As the repulsion and diffusion are both dependent on the drift time which itself is dependent on the applied bias voltage U_{bias}, the agreement of simulation and measurement was tested for different bias voltages. The results are shown in figure 2.11. Although the factor for normalizing the graph of the simulation has only been calculated once for the one with the bias voltage $U_{\text{bias}} = 150\,\text{V}$, the measurements and simulations show a very good agreement for all three bias

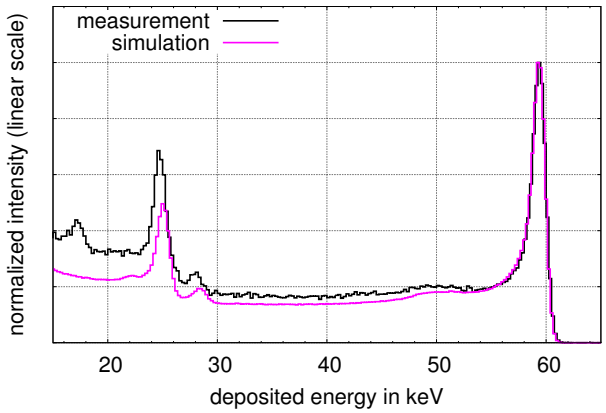

Figure 2.12 Comparison of the distribution of deposited energy derived by measurement and simulation for the radioactive isotope ^{241}Am.

voltages. The discrepancies in energy were expected and are due to the fact, that the energy calibration (page 45) used for all three measurements has been performed at $U_{\text{bias}} = 150\,\text{V}$ only. This shows again the gained accuracy of the simulation and gives the empirical validation that the new threshold energy for choosing the repulsion model is correct.

For a final verification the simulation has also been tested at a different energy for the radioactive isotope ^{241}Am emitting mainly γ-rays at $E = 59.6\,\text{keV}$. These measurements and the simulation have not been performed with the setup shown in figure 2.6, the radioactive isotope has just been placed in front of the detector. The complete emission spectrum of the ^{241}Am-source unfortunately is unknown due to the metal enclosure of this particular radioactive compound. It has also not been determined with the hpGe detector as the flux for this 35 GBq strong radiation source is too high. Therefore, the simulation has been performed mono-energetically at $E = 59.6\,\text{keV}$. Thus, only the energy deposition above $E > 26.34\,\text{keV}$ – a further prominent emission line of ^{241}Am – can be compared. The comparison of simulation and measurement in figure 2.12 shows – with respect to the (unknown) discrepancies of setup and surroundings in measurement and simulation – a good agreement.

All these comparisons have shown the overall correctness and robustness of the simulation. With such a comprehensive simulation tool one can be confident in performing simulations of the monoenergetic response functions, which are needed for the deconvolution of the measured signal into the real impinging spectrum.

3 Spectrometry

Contents

3.1 Introduction to the reconstruction method 17
3.2 Position-resolved spectrometry 41
3.2.1 Pixel-by-pixel energy calibration and anode heel effect 41
3.2.2 Improved global energy calibration 59
3.2.3 Further impacts of a pixel-by-pixel energy calibration 60
3.2.4 Spectrometric imaging 65
3.3 Time-resolved spectrometry 67

3.1 Introduction to the reconstruction method

The deconvolution of the impinging spectrum with the help of simulated detector responses has already been successfully shown in [MTT+09] and [TTM+09]. The methods mentioned there have been limited to high statistics and very coarse energy bin sizes of above 1 keV. For further applications and measurements it was necessary to lower the minimal statistics needed by at least a factor of 10. Firstly, this could be achieved by the direct use of the threshold scan (THL scan) and abundance of its derivative, and secondly, by introducing an iterative deconvolution method – the Bayesian deconvolution. Formerly performed deconvolution methods ([MTT+09] and [TTM+09]) did not consider the uncertainties in the measurement. As those are needed as an exit condition for the iterative deconvolution method, a new extended calibration method including all uncertainties had to be introduced. An excerpt of the C++-source code for the iterative deconvolution process is shown in appendix B.2.

Publication: Bayesian deconvolution applied on measurements with a pixelated detector

In this paper I have given an introduction to the detectors used – the Medipix2 detector and the Timepix detector. The terms THL scan and its derivative are explained in detail. I have also investigated the effects of charge sharing and multiplicity of this particular detector type. These results have found their way

into the newly used deconvolution method based on Bayesian statistics. As it has not been shown completely before, I give a mathematical deviation of this Bayesian deconvolution in a more general way for covering also pixelated detectors. The resulting spectra determined with this deconvolution method are then compared to the formerly used spectrum stripping method. Finally, in comparing the results of my measurements with more established methods, I was able to prove the comparability and stability of this analysis method.
The article is published in the Journal of Instrumentation by IOP Publishing (`http://iopscience.iop.org/1748-0221/`) as:
Peter Sievers et al. 'Bayesian deconvolution as a method for the spectroscopy of X-rays with highly pixelated photon counting detectors'. In: *Journal of Instrumentation* 7.03 (Mar. 2012). DOI: `10.1088/1748-0221/7/03/P03003`;

Contributions of the co-authors:

- running a facility with reference equipment at PTB
- performing the measurements with the hpGe detector
- several discussions about uncertainty propagation and the mathematical derivation of the iterative formula

My own contributions:

- development of an energy calibration method including uncertainty calculations
- Bayesian deconvolution under consideration of effects special to pixelated detectors
- development of a fast analysis tool for performing the deconvolution (code excerpt is given in appendix B.2)
- performing the measurements with the Timepix detector
- performing the analysis

PUBLISHED BY IOP PUBLISHING FOR SISSA MEDIALAB

RECEIVED: *December 6, 2011*
REVISED: *January 16, 2012*
ACCEPTED: *January 30, 2012*
PUBLISHED: *March 9, 2012*

Bayesian deconvolution as a method for the spectroscopy of X-rays with highly pixelated photon counting detectors

P. Sievers,[a,b,1] **T. Weber,**[b] **T. Michel,**[b] **J. Klammer,**[a] **L. Büermann**[a] **and G. Anton**[b]

[a] *Physikalisch-Technische Bundesanstalt (PTB), Bundesallee 100, D-38116 Braunschweig, Germany*

[b] *Radiation Physics Group, Erlangen Centre for Astroparticle Physics (ECAP), University of Erlangen-Nürnberg, Erwin-Rommel-Str. 1, D-91058 Erlangen, Germany*

E-mail: peter.sievers@ptb.de

ABSTRACT: The energy deposition spectrum of highly pixelated photon-counting pixel detectors with a semiconductor sensor layer (e.g. silicon) differs significantly from the impinging X-ray spectrum. This is mainly due to Compton scattering, charge sharing, an energy-dependent sensor efficiency, fluorescence photons and back-scattered photons from detector parts. Therefore, the determination of the impinging X-ray spectrum from the measured distribution of the energy deposition in the detector is a non-trivial task. For the deconvolution of the measured distribution into the impinging spectrum, a set of monoenergetic response functions is needed. Those have been calculated with the Monte Carlo simulation framework ROSI, utilizing EGS4 and including all relevant physical processes in the sensor layer.

We have investigated the uncertainties that spectrum reconstruction algorithms, like spectrum stripping, impose on reconstruction results. We can show that applying the Bayesian deconvolution method significantly improves the stability of the deconvolved spectrum. This results in a reduced minimum radiation flux needed for reconstruction.

In this paper, we present our investigations and measurements on spectrum reconstruction for polychromatic X-ray spectra at low flux with a focus on Bayesian deconvolution.

KEYWORDS: X-ray detectors; Spectrometers; Data processing methods; Hybrid detectors

[1] Corresponding author.

doi:10.1088/1748-0221/7/03/P03003

2012 JINST 7 P03003

Contents

1 Introduction **1**

2 The Medipix2/Timepix detector **2**

3 Charge sharing and multiplicity **3**

4 Deconvolution methods **5**
4.1 Spectrum stripping 5
4.2 Bayesian deconvolution 5
4.3 Energy calibration 7
4.4 Total uncertainty of the measurement 8

5 Results of measurements **10**
5.1 Comparability 11
5.2 Stability 13

6 Conclusion **15**

A Mathematical derivation of the Bayesian deconvolution method **16**

B Tabulated values **18**

2012 JINST 7 P03003

1 Introduction

Spectroscopy of X-ray radiation is a widely used application, for instance in the determination of X-ray tube spectra, synchrotron light spectra, radioactive material composition, and in astronomy. The conventional way of measuring the spectrum with semiconductor devices (e.g. a high purity germanium detector) is to detect the charge carriers released by the impinging photons. As the amount of charge corresponds to the deposited photon energy, it is necessary to collect at least the complete charge of one charge carrier type. Furthermore, in absence of an absorption edge the absorption probability decreases with increasing photon energy. To cope with the requirement of high detection efficiency and energy determination one has to use relatively large and thick semiconductors. This ensures that every photon gets fully absorbed and that any released charge remains within the sensor. Considering the sensor area of such a high purity germanium (hpGe) detector, for instance, it can only be operated at relatively low fluxes.

For pixelated detectors operated at the same radiation flux, the photons are spread over many relatively small areas, and thus, gaining a lower count rate in each pixel. Due to processes in the sensor layer and to electronic noise, the distribution of the deposited energy is distorted (figure 1). This misassignment is mainly caused by Compton-scattered photons getting absorbed in a different

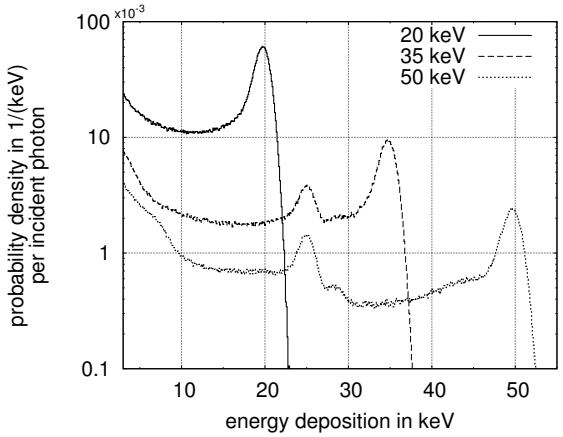

Figure 1. Simulated energy response functions of the detector to monoenergetic X-ray irradiation.

pixel by the diffusion of the generated charge beyond pixel boundaries, by fluorescence photons or by back-scattered photons from detector parts. If the detector setup and the interaction processes in the detector are implemented correctly in a Monte Carlo simulation, the impinging spectrum can be computed by the deconvolution of the measurement [1]. The simulation of the detector response functions has been conducted with the simulation framework ROSI (RoentgenSimulation) [2]. This framework is based on EGS4 with low energy extensions.

The aim of this work is to investigate Bayesian deconvolution for pixelated detectors and its advantages compared to methods like spectrum stripping [1]. We will give a short introduction on the used detector and its calibration. We will provide mathematical detail of the deconvolution method. Our measurements will be compared to the ones performed with hpGe detectors and ionization chambers.

2 The Medipix2/Timepix detector

For the measurements, a Medipix2 detector [3] and a Timepix detector [4] in counting mode, respectively, was used. It consists of an application-specific integrated circuit (ASIC) which has 256×256 pixel cells with a $55\,\mu$m pixel pitch. As sensor material, a silicon layer with a thickness of $300\,\mu$m was bump-bonded to the ASIC. Each pixel cell of the ASIC consists of an analogue and a digital electronics part. In the analogue part of each pixel it is possible to set a global energy threshold E_{dig}. This energy threshold value is transferred via a digital analog converter (DAC) into a reference-voltage. If the voltage pulse caused by the amplified signal of the collected charge is higher compared to this reference voltage, the counter in the digital part of the corresponding pixel gets incremented ([3, section II,A,2] and [4, section 2.1]). By increasing this energy threshold E_{dig} gradually, the distribution D of X-ray photons with respect to their deposited energy in the sensor will be scanned (see figure 2, for example). The number of detected events M as a function of the energy threshold E_{dig} will be referenced as "threshold scan". The relation between the distribution D of the deposited energy and the measurement M is

$$M\left(E_{\mathrm{dig}}\right) = \int_{E_{\mathrm{dig}}}^{\infty} D\left(E\right) dE, \tag{2.1}$$

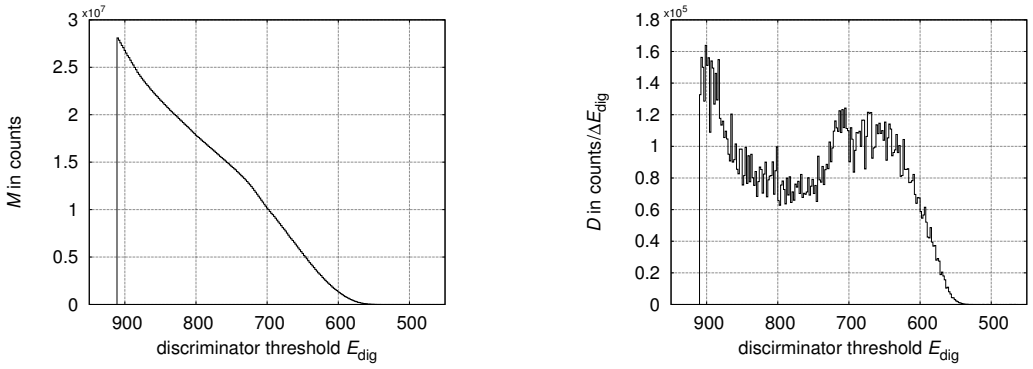

(a) Threshold scan M.

(b) Derivative D of the threshold scan.

Figure 2. Photon detection of the X-ray radiation quality N-40 [5]. (a): number of counts M, (b): derivative D of the function in (a).

where $M\left(E_{\text{dig}}\right)$ denotes the counts taken at a given energy threshold E_{dig} and $D(E)$ is the number of events with an energy deposition E. In a discrete way this equation derives to

$$M_k = \sum_{l=k}^{\infty} D_l \cdot \Delta E_l, \tag{2.2}$$

where k and l are the indices for the discretized energies E_{dig} and E.

The distribution of the deposited energy $\vec{D}$ (figure 2b), the derivative of the threshold scan $\vec{M}$, can be written as a convolution of the "true" impinging spectrum $\vec{T}$ with the matrix $\hat{R}^*$ of the detector response functions [1]:

$$\begin{aligned} \vec{D} &= \hat{R}^* \cdot \vec{T}. \\ D_l &= R^*_{li} T_i. \end{aligned} \tag{2.3}$$

Those R^*_{li} denote the counts per incident photon in the l-th channel caused by a photon of the energy E_i. Substituting equation (2.3) into (2.2) yields

$$\begin{aligned} M_k &= \sum_{l=k}^{\infty} \sum_i R^*_{li} T_i \cdot \Delta E_l \\ &= \sum_i R_{ki} \cdot T_i \\ \vec{M} &= \hat{R} \cdot \vec{T}, \end{aligned} \tag{2.4}$$

with $R_{ki} = \sum_{l=k}^{\infty} R^*_{li} \cdot \Delta E_l$. i and k denote the channel indices of the corresponding histograms. By solving equation (2.4) or (2.3), the impinging spectrum $\vec{T}$ can be calculated. The matrix $\hat{R}^*$ is simulated and an excerpt of three energies is shown in figure 1. The peak at about 25.3 keV is caused by the K_α fluorescence of tin included in the bump-bonds.

3 Charge sharing and multiplicity

During drift of the released charge carriers towards the pixel electrodes of the sensor the size of the charge cloud increases continuously due to diffusion. If the projected area of the charge cloud

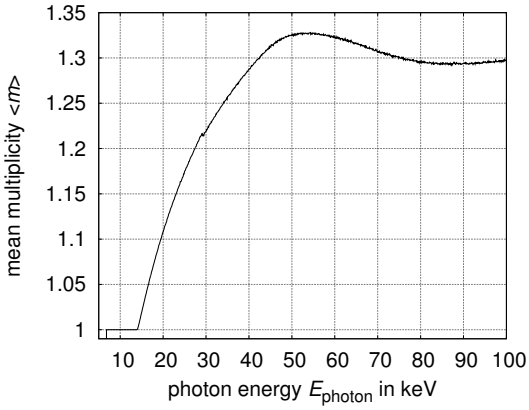

Figure 3. Simulated energy dependency of the multiplicity for monoenergetic irradiation at a threshold of 7.0 keV.

onto the pixel electrode plane exceeds the size of a pixel several pixels might be triggered. This behaviour is called charge sharing as the released charge is shared among neighbouring pixels. A statistical measure for the charge sharing is the average number of triggered pixels per detected photon, which is called mean multiplicity [6]:

$$\langle m \rangle = \frac{\sum_{p=1}^{\infty} p \cdot N_p}{\sum_{p=1}^{\infty} N_p} \tag{3.1}$$

and the average quadratic multiplicity

$$\langle m^2 \rangle = \frac{\sum_{p=1}^{\infty} p^2 \cdot N_p}{\sum_{p=1}^{\infty} N_p}. \tag{3.2}$$

N_p is the number of p-fold events (p triggered pixels). The mean multiplicity includes not only the charge sharing but also the influence of events with two interactions of one photon in the sensor (e.g. Compton scattering with subsequent photoabsorption of the scattered photon). The simulated energy dependency of the multiplicity for monoenergetic irradiation of a Timepix detector is shown in figure 3. The simulated detector parameters were: 300 μm thick sensor, 55 μm pixel pitch and silicon as sensor material. For triggering a second pixel the photon energy E_{photon} has to be at least twice of the threshold energy. Therefore the mean multiplicity $\langle m \rangle$ equals one until the energy E_{photon} exceeds 14 keV. The small dip in the curve is due to the K-edge (29.2 keV) of tin included in the bump-bonds. The multiplicity $\langle m \rangle$ can in general be increased by: decreasing the threshold, smaller pixels or a thicker sensor layer.

Capacitive coupling and charge induction on neighbouring collection electrodes can be neglected for the following two reasons. First, the integration time of the preamplifier (90 – 180 ns) is significantly longer then the maximal drift time (7 – 20 ns) of the charge carrier (in silicon). Second, the effect of charge trapping in silicon, used as sensor material, is negligible as the lifetime (2.5 ms [7]) of the charge carrier is much longer than the maximal drift time. A deeper insight on the thematic of electrode size, capacitive coupling and time dependency of induced signals can be found at [8] and [9].

2012 JINST 7 P03003

4 Deconvolution methods

4.1 Spectrum stripping

The spectrum stripping method is shortly introduced here as we will compare its results to the ones of Bayesian deconvolution later on in this paper. This deconvolution method described in [1] is based on the following assumption: The entries in the highest energy bin of the measurement M_{max} (the following is also valid for the distribution of the deposited energy D) are caused by the number of photons T_{max} with the highest energy in the spectral distribution:

$$T_{\mathrm{max}} = M_{\mathrm{max}} / R_{\mathrm{max,max}}. \tag{4.1}$$

Starting at the highest energy bin, the incoming spectrum can now be reconstructed successively:

$$T_i = \left(M_i - \sum_{k=i+1}^{\mathrm{max}} R_{ik} T_k \right) / R_{ii}. \tag{4.2}$$

In the case of this method the energies channels of the measurement M and the spectrum T have to be the same. Thus the matrix $\hat{R}$ is a square matrix.

4.2 Bayesian deconvolution

As described in [10], the impinging spectrum $\vec{T}$ can be derived from the distribution of the deposited energy $\vec{D}$ by an iterative process called "Bayesian deconvolution". The mathematical derivation including the detection efficiency ε is partly analog to the method applied by the authors of [10] and [11]. For pixelated detectors one has to take into account some more general assumptions:

1. The author of [11] restricts the range of possible values for the detection efficiency ε to $0 < \varepsilon_i \leq 1$. As the effect of multiple counts per one photon (section 3) cannot be neglected we have to state for the detection efficiency τ_i^* of pixelated detectors: $0 < \tau_i^* = \varepsilon_i \cdot \langle m \rangle$. As the absorption probability can be approximate 100 %, especially for low photon energies, and $\langle m \rangle \geq 1$, it is obvious that this "efficiency" τ_i^* can generally be greater then one. Therefore, we introduce $\tau_i^* \equiv \sum_k R_{ki}^*$ as a symbol for the mean number of triggered pixels per incident photon (or regarding the measurement M: $\tau_i = \sum_k R_{ki}$).

2. In publication [10] it is implied that $\sum_i T_i$ equals $\sum_k D_k$ (or $\sum_k M_k$). This predicts that τ_i^* equals 1 which in general is not fulfilled for pixelated detectors. Possible values of τ_i^* for the used Timepix have been plotted in figure 4.

Because of these changes and as we are not using the distribution of the energy deposition, the derivation of the iterative reconstruction equation will be shown in a more general way for completeness. This deconvolution method is based on Bayes' theorem [12]:

$$P(A|B) = \frac{P(B|A)\,P(A)}{P(B)}. \tag{4.3}$$

2012 JINST 7 P03003

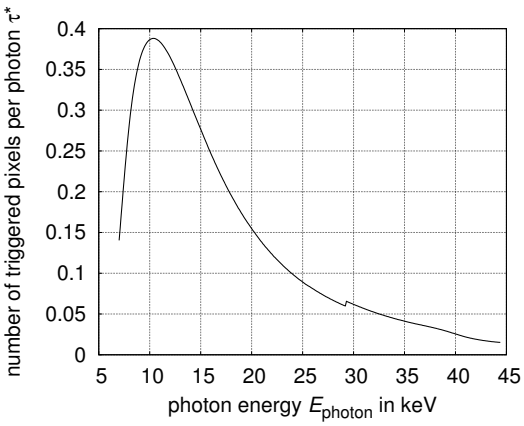

Figure 4. Simulated energy dependency of the τ^* for monoenergetic irradiation.

$P(A|B)$ denotes the probability that the event A will occur under the condition that B is true or has occurred. $P(A)$ or $P(B)$, respectively, denote the total probability of event A or B, respectively. To fit our purposes, Bayes' theorem (eq. (4.3)) can in general be rewritten as:

$$P(T_i|A_k) = \frac{P(A_k|T_i)\,P(T_i)}{P(A_k)}. \tag{4.4}$$

A represents either the measured threshold scan M or its derivative D and T represents the true impinging spectrum. i and k denote the channel indices of the corresponding histograms. The complete derivation shown in section A leads finally to:

$$T_i^{n+1} = \frac{1}{\tau_i^*} T_i^n \sum_k \frac{R_{ki}^* \cdot D_k}{\sum_j R_{kj}^* \cdot T_j^n} \tag{4.5}$$

and

$$T_i^{n+1} = \frac{1}{\tau_i} T_i^n \sum_k \frac{R_{ki} \cdot M_k}{\sum_j R_{kj} \cdot T_j^n}, \tag{4.6}$$

with the iteration index n and the mean number of triggered pixels per incident photon $\tau_i^* = \sum_k R_{ki}^*$ (respective $\tau_i = \sum_k R_{ki}$).

The exit condition for this iterative process is defined in the following. For each iteration step, the "virtual measurement" $\vec{M}_\mathrm{v}$ is computed by the convolution of the detector response functions $\hat{R}$ with the unfolded spectrum $\vec{T}^{n+1}$ of the actual iteration step.

$$\vec{M}_\mathrm{v} = \hat{R} \cdot \vec{T}^{n+1} \tag{4.7}$$

By setting the measurement M into relation to this calculated M_v, one gets a degree of their correlation. This relation is expressed by the χ^2:

$$\chi^2 = \frac{\sum_{i=1}^{N} \left(\frac{M_{\mathrm{v},i} - M_i}{\sigma_\mathrm{total}(M_i)} \right)^2}{N}, \tag{4.8}$$

where N denotes the size of $\vec{M}$. If the condition $\chi^2 \leq 1$ is reached, the iteration process is stopped and the actual $\vec{T}^{(n+1)}$ is regarded as the true impinging spectrum T. For the distribution of deposited

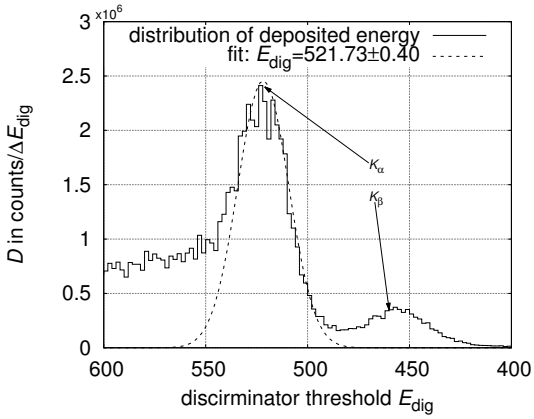

Figure 5. Derivative of a threshold scan measured during irradiation by a Gd K_α-fluorescence source (solid line) and a normal distribution fitted to its full energy peak with $\bar{E}_{\text{dig}} = 521.73$ and $\Delta\bar{E}_{\text{dig}} = 0.40$ (dotted line).

energy D the χ^2 is defined analog:

$$\chi^2 = \frac{\sum_{i=1}^{N} \left(\frac{Dv_i - D_i}{\sigma_{\text{total}}(D_i)} \right)^2}{N} \tag{4.9}$$

To compute the χ^2 (eq. (4.8)), the uncertainties of the measurement σ_{total} have to be taken into account. One main contribution to the uncertainty is caused by the energy calibration of the detector.

4.3 Energy calibration

To translate the energy threshold values E_{dig} to real energies E a calibration has to be performed. Therefore, the detector is irradiated with nearly monoenergetic X-rays. Applicable sources are, for instance, Am-241 or fluorescence lines of Gd, Mo and Cu. For each of them a threshold scan has to be taken. Looking at the derivative of such a threshold scan a normal distribution can be fitted on the full energy peak. For each calibration point the mean of the peak position $\bar{E}_{\text{dig}}$ and and its uncertainty $\Delta\bar{E}_{\text{dig}}$ are computed. For instance, the fit for a Gd K_α-fluorescence is shown in figure 5. By fitting the calibration curve at at least three energies, the threshold calibration can be performed. As we want to take into account the uncertainties $\Delta\bar{E}_{\text{dig}}$ of each calibration point, the function $E_{\text{dig}} = f\left(E_{\text{photon}}\right)$ (equation (4.10)) — the inverse of the required function $E_{\text{photon}} = f\left(E_{\text{dig}}\right)$ — has to be fitted into the calibration values (shown in figure 6a).

$$E_{\text{dig}} = a_0 + a_1 \cdot E_{\text{photon}} \tag{4.10}$$

Therefore, we obtain the uncertainties $var(a_0)$, $var(a_1)$ and $cov(a_0, a_1)$. In the case of the calibration shown in figure 6a the following values are computed:

$$var(a_0) = 4.21, \quad var(a_1) = 1.01 \times 10^{-2}\,\text{keV}^{-2} \quad \text{and} \quad cov(a_0, a_1) = -0.200\,\text{keV}^{-1}.$$

The energy calibration used, is derived by inverting equation (4.10) shown in figure 6b.

$$\begin{aligned} E_{\text{photon}} &= \frac{-a_0}{a_1} + \frac{1}{a_1} \cdot E_{\text{dig}} \\ &= b_0 + b_1 \cdot E_{\text{dig}} \end{aligned} \tag{4.11}$$

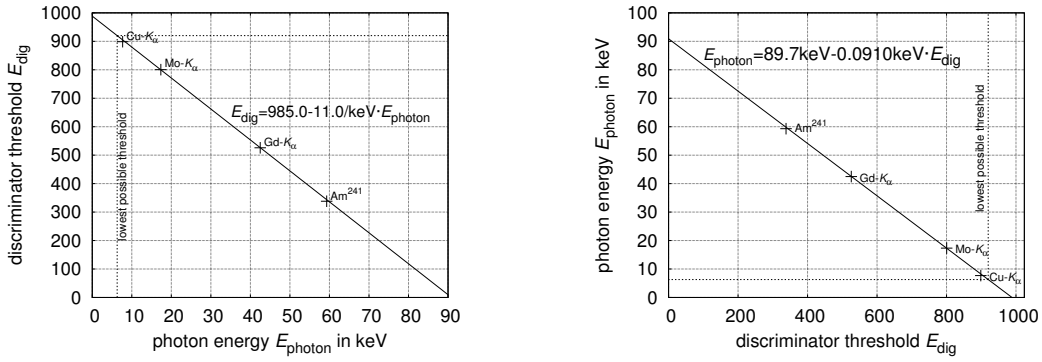

(a) Calibration curve fitted on four energies.

(b) Inverse of the calibration curve.

Figure 6. Calibration curves for the energy calibration.

The propagation of uncertainties is described by the set of equations (4.12).

$$\begin{aligned} var(b_0) &= var(a_0)\cdot b_1^2 + 2\cdot cov(a_0,a_1)\cdot \frac{b_0}{b_1^2} + b_0^2\cdot var(a_1) \\ var(b_1) &= \frac{var(a_1)}{b_1^4} \\ cov(b_0,b_1) &= cov(a_0,a_1)\cdot b_1^3 + var(a_1)\cdot b_0\cdot b_1^3 \end{aligned} \tag{4.12}$$

In our case (figure 6b) the absolute values of these uncertainties are:

$$var(b_0) = 0.428\,\mathrm{keV}^2, \quad var(b_1) = 7.19\times 10^{-7}\mathrm{keV}^2 \quad \text{and} \quad cov(b_0,b_1) = -5.53\times 10^{-4}\mathrm{keV}^2.$$

With these uncertainties, an overall uncertainty for the energy calibration can be obtained.

$$\sigma^2(E) = var(b_0) + 2\cdot\frac{E-b_0}{b_1}\cdot cov(b_0,b_1) + \left(\frac{E-b_0}{b_1}\right)^2\cdot var(b_1) \tag{4.13}$$

With such a threshold calibration the threshold scan shown in figure 2 will be transformed into a calibrated one shown in figure 7. This time the y-axis is plotted in logarithmic scale to show that those oscillations seen in the derivative D (figure 2b and 7b) are not visible in the threshold scan M. The energy resolution of our detector is shown in figure 8. It is defined by the FWHM of the fitted normal distribution (figure 5) for each calibration point.

4.4 Total uncertainty of the measurement

There are two main contributions to the total uncertainty: the statistical uncertainty of the detected number of events σ_{stat} and the energy calibration uncertainty $\sigma(E)$ (eq. (4.13)).

$$\sigma_{stat}(M_i) = \sqrt{M_i} \tag{4.14}$$

In equation (4.14), the effect of multiple counts for one photon (section 3) — e.g. caused by charge sharing — is neglected. If the multiplicity m was known, the statistical uncertainty could be expressed as shown in [6]:

$$\sigma_{stat}(M_i) = \sqrt{\frac{\langle m^2\rangle}{\langle m\rangle}M_i}. \tag{4.15}$$

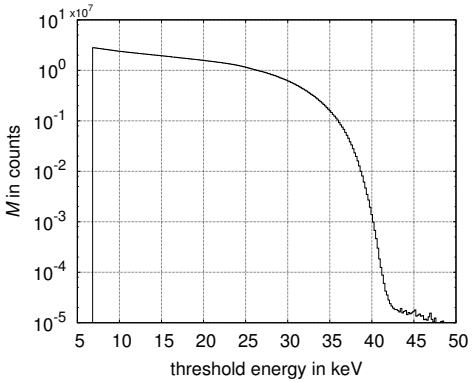

(a) Threshold scan M.

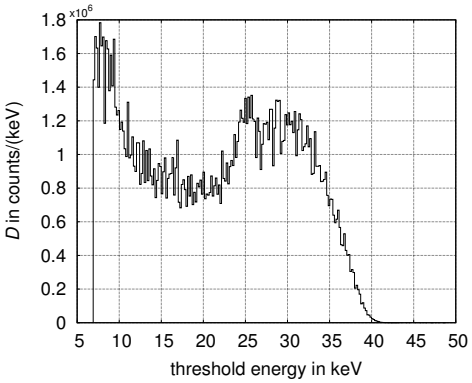

(b) Derivative D of the threshold scan.

Figure 7. Photon detection of the X-ray radiation quality N-40 as shown in figure 2 after threshold calibration. (a): number of counts M, (b): derivative D of the function in (a).

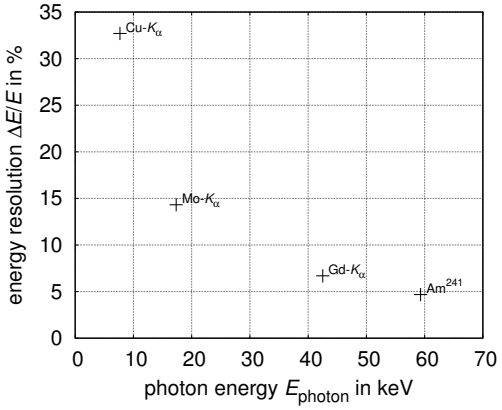

Figure 8. Energy resolution of the used Timepix detector.

Figure 9 (left plot) shows a zoom into a threshold scan with those two uncertainties (σ_{stat} and $\sigma(E)$) plotted. As the uncertainties of the energy axis could not yet be taken into account for the deconvolution, the energy calibration uncertainty $\sigma(E_i)$ has to be transformed to an uncertainty depending on M_i. The calibration uncertainty $\sigma(E_i)$ can be seen as the probability that the counts M_i are misassigned to a neighboring energy channel $E_{i\pm z}$. Therefore we can describe the systematic uncertainty σ_{syst} by a weighted difference of counts in neighboring channels.

$$\sigma_{\text{syst}}(M_i) = \left| \frac{M_{i-1} - M_{i+1}}{E_{i-1} - E_{i+1}} \right| \cdot \sigma(E_i) \tag{4.16}$$

The propagation of the statistical and systematic uncertainty leads to the total uncertainty

$$\sigma_{\text{total}}(M_k) = \sqrt{\sigma^2_{\text{stat}}(M_k) + \sigma^2_{\text{syst}}(M_k)}, \tag{4.17}$$

shown in figure 9 (right plot). As shown in figure 10, the σ_{syst} caused by the calibration uncertainty $\sigma(E)$ (equation (4.16)) is the most significant contribution to the total uncertainty σ_{total}. For

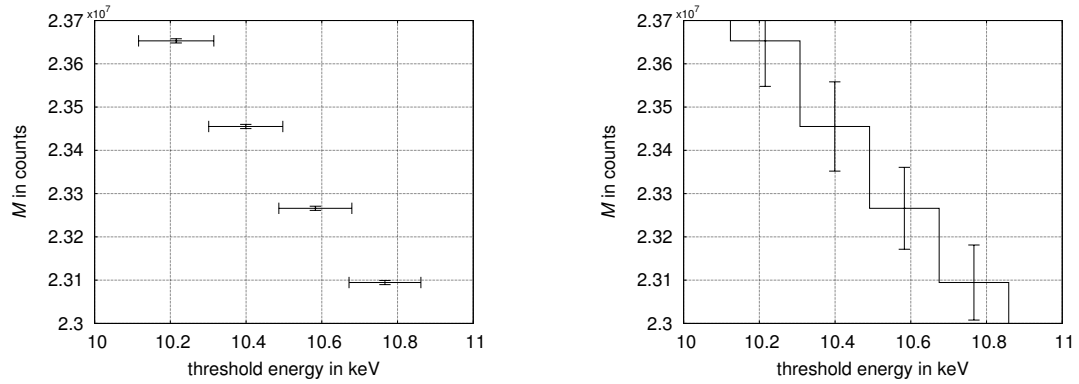

Figure 9. Zoom into the threshold scan shown in figure 7, plotted with its uncertainties σ_{stat} and $\sigma(E)$ (left plot) and its calculated total uncertainty σ_{total} (right plot).

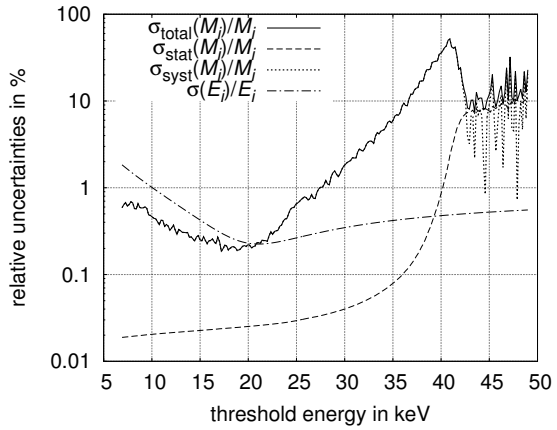

Figure 10. Relative uncertainties of the measured number of counts M_i and the relative uncertainty of the energy calibration. Below 42 keV, the dotted line for σ_{syst} is mostly covered by the solid line of σ_{total}.

completeness, the total uncertainty $\sigma_{\text{total}}(D_k)$ of the distribution $D_k = (M_k - M_{k+1}) \cdot \Delta E_k^{-1}$ of the deposited energy is given by

$$\sigma^2_{\text{total}}(D_k) = \left[\sigma^2_{\text{stat}}(M_k) + \sigma^2_{\text{stat}}(M_{k+1}) + \left(\sigma_{\text{syst}}(M_k) - \sigma_{\text{syst}}(M_{k+1})\right)^2\right] \cdot \Delta E_k^{-2}. \tag{4.18}$$

5 Results of measurements

The result of the deconvolution for the data shown in figure 7 is shown in figure 11. The Timepix detector was irradiated with the X-ray radiation quality N-40 [5] (table 3). The X-ray tube was operated at an anode current of 50 mA. The measurement (the threshold scan) was taken using a Timepix detector under the following conditions: distance between detector and X-ray tube was 2.0 m; step size of the scan $\Delta E_{\text{dig}} = 2$ which corresponds to an energy chanel width of the measurement $\Delta E_{\text{M}} = 0.18$ keV; measuring time per energy threshold 15 s (amounts to 1 h in total); count rate at lowest threshold (6.9 keV) per pixel 28.6 s^{-1} (in total 1.87 $\times$ 10^6 s^{-1}). The channel width of the impinging spectrum ΔE_{T} was arbitrarily chosen as $\Delta E_{\text{T}} = 0.5$ keV. With the used detector

2012 JINST 7 P03003

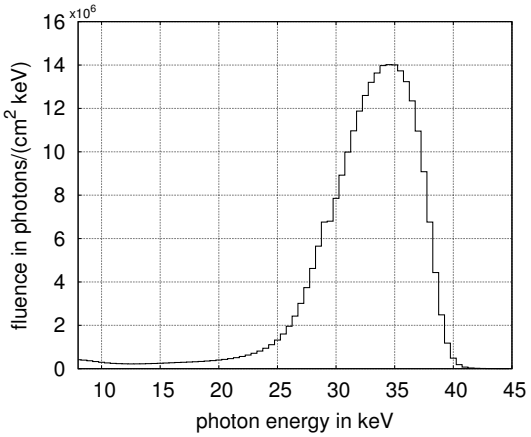

Figure 11. Spectrum of the radiation quality N-40, in absolute values, determined with the Bayesian deconvolution method from the threshold-scan seen in figure 7.

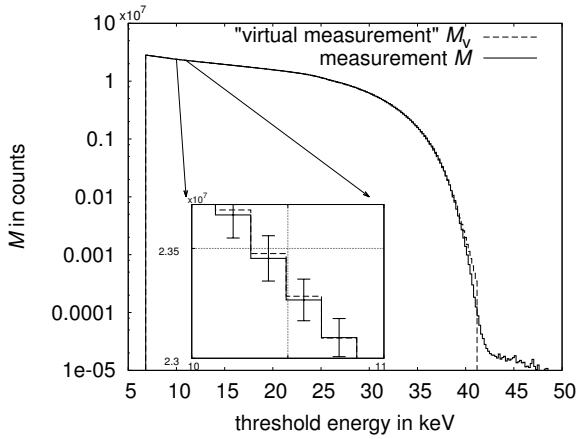

Figure 12. Photon detection of the X-ray radiation quality N-40 and the predicted number of events M_v.

response functions $\hat{R}$, this deconvolved spectrum $\vec{T}$ would result in a "virtual" measurement $\vec{M}_\mathrm{v}$ seen in figure 12. The predicted number of events M_v are calculated by the convolution of the detector response functions $\hat{R}$ with the unfolded spectrum $\vec{T}$. They are in good agreement with the measurement $\vec{M}$ as 77% of the $M_{\mathrm{v},i}$ are within the error range of the M_i.

5.1 Comparability

The reference measurements were taken with a high purity Germanium (hpGe) detector.[1] Those were measured at the same tube voltage (40 kV) but at a different current (0.5 mA) and distance (2.5 m). With these settings the dead time was at about 7.3%. For the comparison, our deconvolved spectrum was corrected for the extra 50 cm of absorption in air (figure 13). The contributions to the deconvolved spectrum at energies below ≈ 25 keV could be due to scattered photons (in air, at surrounding parts/walls, etc.), as our measurement with the Timepix detector was performed

[1] Detector model GLP-25300/13P (Ø = 25 mm, depth = 13 mm), hV module 659, ADC AM MCB 926 and amplifier 671 from the vendor ORTEC operated at: bias: −2 kV; coarse gain: 50; fine gain: 0.9.

2012 JINST 7 P03003

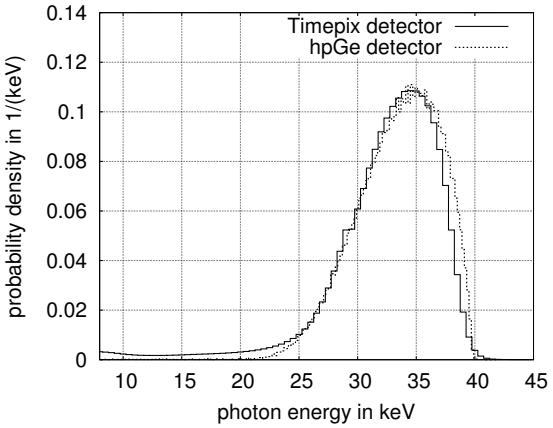

Figure 13. Spectrum of the radiation quality N-40 determined with the Bayesian deconvolution method from data taken with Timepix detector (solid line) and measured with a hpGe detector (dotted line). The graphs have been normalized by their integral.

Table 1. Reference values [13] and calculated half value layers (HVL) of aluminium and copper for the radiation quality N-40 at a reference distance of 2.5 m. The values in brackets are calculated with a cut-off energy at $E_{\min} = 20.0\,\mathrm{keV}$ as proposed in [14].

		PTB DOS-34	Timepix detector	hpGe detector
1st HVL in mm	Al	2.65	2.21	2.71
	Cu	0.086	0.071 (0.083)	0.087 (0.088)
2nd HVL in mm	Al	2.84	2.77	2.91
	Cu	0.093	0.090 (0.092)	0.095 (0.094)

without any collimator (aperture angle 180°). This is opposite to the measurements performed with the hpGe detector as this detector had to be collimated (aperture angle $\approx 0.8°$) because of the flux and for achieving total absorption. Therefore the hpGe detector should not detect any scattered photons. As the half value layers (HVL) are a measure of the conformity of two spectra we calculated them and compared them in table 1 to the reference data given in [5]. The differences for the 1st HVL are due to the discrepancies in the lower energy region ($E < 25\,\mathrm{keV}$) seen in figure 13. The values for the 2nd HVL are in good agreement as the high energy range ($E > 25\,\mathrm{keV}$) shows a good conformity. According to [14, table 3] the 1st HVL varies up to 10% relatively to the values of the ISO-4037 depending on the method of determination. As our measurement is in the same range of deviation ($3.5 - 17.4\%$) it is in good agreement with the theoretical values.

For a comparison of the absolute number of photons, the air kerma rate $\dot{K}_a$ was calculated. The measurement with the calibrated monitor chamber[2] gave a kerma rate $\dot{K}_a = 6.53\,\mu\mathrm{Gys}^{-1}$. By folding the measured fluence spectrum (figure 11) with the interpolated conversion coefficients for air kerma per unit fluence $\frac{K_a}{\Phi}$ [15, table A.1] (table 2), a kerma rate $\dot{K}_a = 6.35\,\mu\mathrm{Gys}^{-1}$ was calculated. As the deviation of those two kerma values is approximate 3%, one can be confident about the correctness of the deconvolved absolute fluence.

[2]Chamber model TM786 from the vendor PTW.

2012 JINST 7 P03003

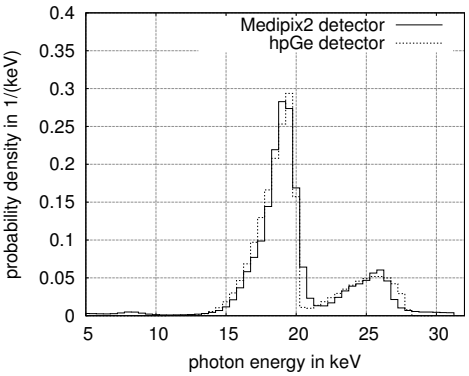

(a) WMH-28 (W-anode; Mo- and Al-filtration).

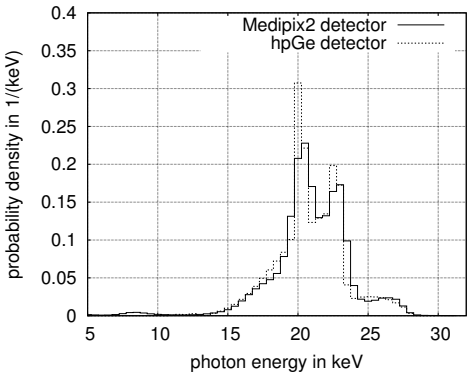

(b) RRH-28 (Rh-anode; Rh- and Al-filtration).

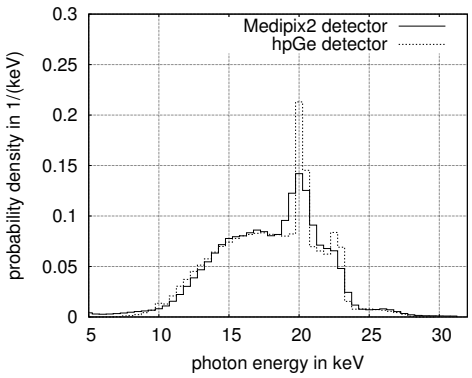

(c) RRV-28 (Rh-anode; Rh-filtration).

Figure 14. Spectrum of different radiation qualities used in mammography (WMH-28 (a); RRH-28 (b); RRV-28 (c)) determined with the Bayesian deconvolution method from data taken with Medipix2 (solid line) and measured with a hpGe detector (dotted line). The graphs have been normalized by their integral.

The preceding measurement was taken with a Timepix. The following three measurements were performed with a Medipix2. Figures 14a to 14c show the deconvolved spectra for a different tube anode and filtering at a tube-voltage of 28 keV (table 3). Those different X-ray radiation qualities (WMH-28, RRH-28 and RRV-28 [16]) are used in mammography. As one can see, the Bayesian deconvolution for the Medipix2 is also in good agreement with the measurement being performed for reference with a hpGe detector. For a better comparison of the steep slopes in the spectrum, the reference measurement in all three plots has been binned to a channel width of $\Delta E_{\mathrm{T}} = 0.5\,\mathrm{keV}$.

5.2 Stability

This Bayesian deconvolution method has also been tested for stability issues regarding the energy channel width of either the measurement ΔE_{M} or the deconvolved spectrum ΔE_{T}. The problem has been encountered in paper [1, figure 7]. Those problems regarding the oscillations in the unfolded spectra after applying the spectrum stripping method (section 4.1 and described in detail in paper [1, chapter 4.1]) could be reproduced (figure 15). In our case, it got even worse because of the low

2012 JINST 7 P03003

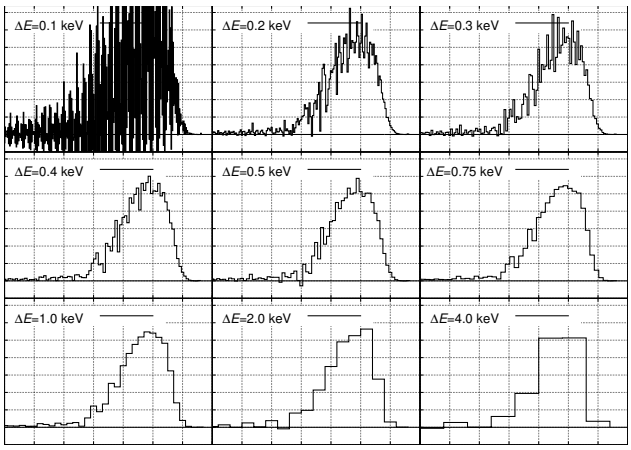

Figure 15. Spectrum of the radiation quality N-40 reconstructed with the spectrum stripping method for different energy channel widths. The ranges for the axes are: X-axis: 10 keV to 45 keV, Y-axis: -5×10^6 to $3.7 \times 10^7 \frac{\text{photons}}{\text{keV}}$.

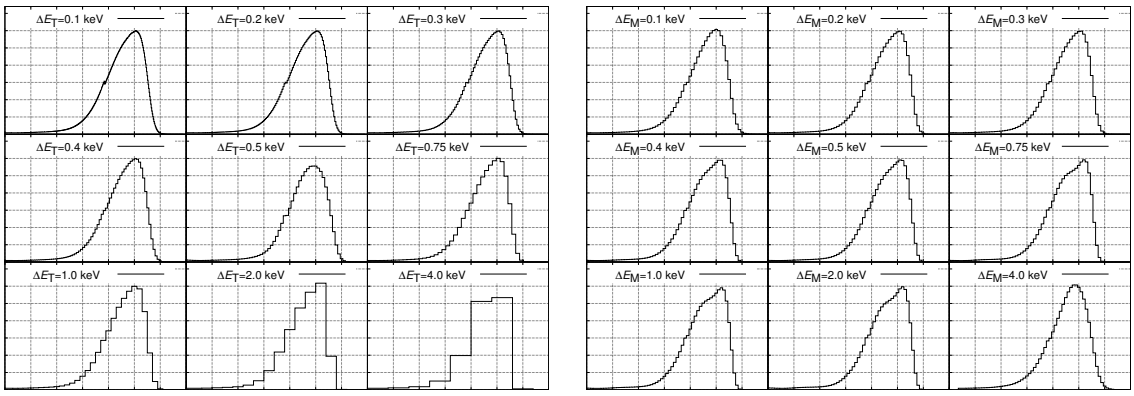

(a) Variable output binning $\Delta E_\text{T} = 0.1\,\text{keV} \ldots 4.0\,\text{keV}$. **(b)** Variable input binning $\Delta E_\text{M} = 0.1\,\text{keV} \ldots 4.0\,\text{keV}$.

Figure 16. Spectrum of the radiation quality N-40 reconstructed with Bayesian deconvolution for different output binning ΔE_T at a constant input binning of $\Delta E_\text{M} = 0.18\,\text{keV}$ (a) and for different input binning ΔE_M at a constant output binning of $\Delta E_\text{T} = 0.5\,\text{keV}$ (b). The ranges for the axes are: X-axis: 10 keV to 45 keV, Y-axis: 0 to $3.7 \times 10^7 \frac{\text{photons}}{\text{keV}}$

statistics in the measurement. For the spectrum stripping, the energy channel widths for input and output have to be the same $\Delta E_\text{M} = \Delta E_\text{T}$.

Bayesian deconvolution is not limited to $\Delta E_\text{M} = \Delta E_\text{T}$, thus different combinations were tested. In the case of figure 16a, the input channel has a fixed width of $\Delta E_\text{M} = 0.18\,\text{keV}$. This value is the direct result of the energy calibration. As the channel width of the reconstructed impinging spectrum is a free parameter, it was varied from $\Delta E_\text{T} = 0.1\,\text{keV} \ldots 4.0\,\text{keV}$. On the other hand, in figure 16b, ΔE_T had been fixed to $\Delta E_\text{T} = 0.5\,\text{keV}$ and the binning of the measurement was varied $\Delta E_\text{M} = 0.1\,\text{keV} \ldots 4.0\,\text{keV}$. All these graphs seen in figures 15 and 16 are based on the same measured input data.

For comparing the 18 graphs seen in figures 16, the impinging spectrum T was summed over discreet energy bins in the range of $12 - 44\,\text{keV}$ for each of them and plotted in figure 17a. The un-

2012 JINST 7 P03003

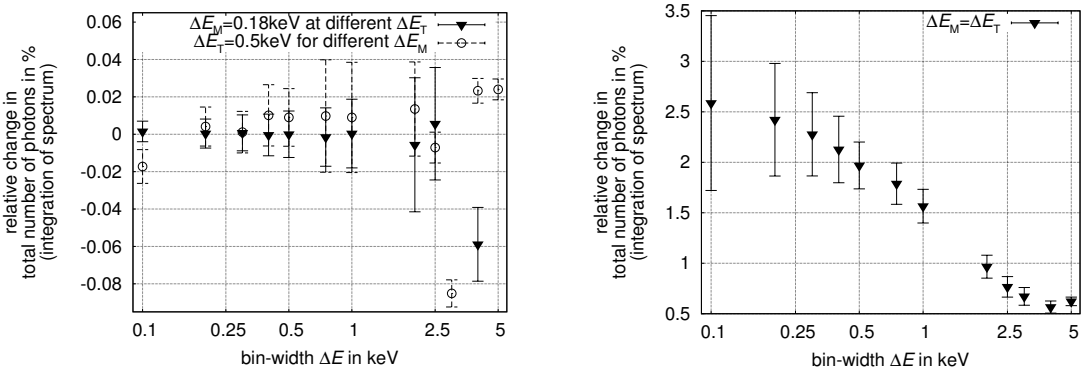

(a) Bayesian deconvolution

(b) Spectrum stripping

Figure 17. Changes in the integral of the spectrum of the radiation quality N-40 relatively to the one deconvolved with the Bayesian method with $\Delta E_{\mathrm{M}} = 0.18\,\mathrm{keV}$ and $\Delta E_{\mathrm{T}} = 0.5\,\mathrm{keV}$ (absolute value: 2.66684×10^8 photons).

certainties have been calculated in the following way: The measurement was pertubated artificially by the statistical error and deconvolution was applied 10000 times on such a pertubated measurement. Therefore we obtained an uncertainty in each bin of the unfolded spectrum and were able to calculate the uncertainty of the integral. For the spectrum stripping method, the calculated integrals are - as expected - in the same range (figure 17b), but as the corresponding spectra (figure 15) don't look reasonable they have not been taken into account any further. As seen in figure 17a, there is only a slight change (less than 0.09%) in the integral of the spectrum. The maximum relative change in the integral between the maximum and the minimum is at approximate 0.12%. It is clearly visible that the variation of the channel width ΔE_{T} has no statistically significant influence on the deconvolution. Even the effect of varying the channel width ΔE_{M} is quite negligible.

6 Conclusion

The Bayesian deconvolution method was applied for the determination of X-ray spectra measured with highly pixelated detectors such as Medipix2 or Timepix. Two different comparative measurements with a Germanium detector and an ionization chamber have been performed. Compared to these measurements our results for both the shape of the deconvolved spectra and also the absolute number of photons show very good agreement (deviations about $3-10\%$). Thus we were able to validate the reliability of this method.

Compared to currently used spectrum deconvolution methods, for example spectrum stripping, Bayesian deconvolution turned out to be more robust and stable. It is shown that the choice of the energy channel width has no significant influence on the deconvolved spectrum in contrast to spectrum stripping.

As the Bayesian deconvolution method used for spectral reconstruction is more stable regarding the minimum flux needed it might be performed in each pixel and therefore be applied for spectral imaging. Possible applications are given in the field of quality assurance for X-ray tubes or in investigating the anode heel effect.

2012 JINST 7 P03003

A Mathematical derivation of the Bayesian deconvolution method

The deconvolution method is based on Bayes' theorem [12]:

$$P(A|B) = \frac{P(B|A)\,P(A)}{P(B)}. \tag{A.1}$$

$P(A|B)$ denotes the probability that the event A will occur under the condition that B is true or has occurred. $P(A)$ or $P(B)$, respectively, denote the total probability of event A or B, respectively. To fit our purposes, Bayes' theorem (eq. (A.1)) can in general be rewritten as:

$$P(T_i|A_k) = \frac{P(A_k|T_i)\,P(T_i)}{P(A_k)}. \tag{A.2}$$

A represents either the measured threshold scan M or its derivative D and T represents the true impinging spectrum. i and k denote the channel indices of our corresponding histograms. Rewriting equation (A.2) leads to

$$P(A_k)\cdot P(T_i|A_k) = P(T_i)\cdot P(A_k|T_i)\,. \tag{A.3}$$

To gain the total probabilities for $P(A_k)$ and $P(T_i)$, both sides of equation (A.3) are summed over i and k, respectively:

$$\begin{aligned}
\sum_i P(A_k)\,P(T_i|A_k) &= \sum_i P(T_i)\,P(A_k|T_i)\\
P(A_k)\underbrace{\sum_i P(T_i|A_k)}_{\lessapprox 1} &= \sum_i P(T_i)\,P(A_k|T_i)\\
P(A_k) &= \sum_i P(T_i)\,P(A_k|T_i)
\end{aligned} \tag{A.4}$$

and

$$\begin{aligned}
\sum_k P(A_k)\,P(T_i|A_k) &= \sum_k P(T_i)\,P(A_k|T_i)\\
\sum_k P(A_k)\,P(T_i|A_k) &= P(T_i)\cdot\underbrace{\sum_k P(A_k|T_i)}_{\equiv\alpha_i>0}\\
P(T_i) &= \frac{1}{\alpha_i}\sum_k P(A_k)\,P(T_i|A_k).
\end{aligned} \tag{A.5}$$

In equation (A.4), the sum $\sum_i P(T_i|A_k)$ is assumed to equal 1. This is true for detectors operating above the electronic noise level. $\sum_i P(T_i|D_k) = 1$, for instance, predicts that every count in the distribution of deposited energy (or in the measurement) is caused by a photon. For the Medipix2/Timepix detector this is true with respect to the lowest used energy threshold E_{dig}.

The link between α_i and the mean number of triggered pixels per incident photon τ_i will be shown further on in equation (A.12). Substituting equation (A.4) into (A.2) yields

$$P(T_i|A_k) = \frac{P(A_k|T_i)\,P(T_i)}{\sum_i P(T_i)\,P(A_k|T_i)} \tag{A.6}$$

2012 JINST 7 P03003

and substituting (A.6) into (A.5) finally yields

$$P(T_i) = \frac{1}{\alpha_i} \sum_k \frac{P(A_k|T_i)\,P(T_i)\,P(A_k)}{\sum_j P(A_k|T_j)\,P(T_j)}. \tag{A.7}$$

As $P(T_i)$ appears on both sides of equation (A.7), an iterative relationship can be devised:

$$P^{(n+1)}(T_i) = P^{(n)}(T_i) \frac{1}{\alpha_i} \sum_k \frac{P(A_k|T_i)\,P(A_k)}{\sum_j P(A_k|T_j)\,P^{(n)}(T_j)}. \tag{A.8}$$

The link between the probabilities $P(T_i)$, $P(M_k)$, and $P(M_k|T_i)$ and their measurable pendants T_i, M_k, and R_{ki} will be shown in the following few equations:

$$P(T_i) = \frac{T_i}{\sum_z T_z} = T_i/\mathbf{T} \tag{A.9}$$

$$P(D_k) = \frac{D_k}{\sum_z D_z} = \frac{D_k}{\mathbf{D}}; \qquad P(M_k) = \frac{M_k}{\sum_z M_z} = \frac{M_k}{\mathbf{M}} \tag{A.10}$$

$$P(D_k|T_i) = \frac{\mathbf{T}}{\mathbf{D}} R^*_{ki}; \qquad P(M_k|T_i) = \frac{\mathbf{T}}{\mathbf{M}} R_{ki} \tag{A.11}$$

$$\alpha_i \equiv \sum_k P(A_k|T_i) \overbrace{=}^{A_k=M_k} \sum_k \frac{\mathbf{T}}{\mathbf{M}} R_{ki} = \frac{\mathbf{T}}{\mathbf{M}} \tau_i. \tag{A.12}$$

Equation (A.11) is a direct consequence of:

$$\sum_i P(M_k|T_i)\,P(T_i) \overbrace{=}^{\text{eq: (A.4)}} P(M_k) \overbrace{=}^{\text{eq: (A.10)}} \frac{M_k}{\mathbf{M}} \overbrace{=}^{\text{eq: (2.4)}} \frac{\sum_i R_{ki} T_i}{\mathbf{M}} = \sum_i \frac{\mathbf{T}}{\mathbf{M}} R_{ki} \frac{T_i}{\mathbf{T}} \overbrace{=}^{\text{eq: (A.9)}} \sum_i \frac{\mathbf{T}}{\mathbf{M}} R_{ki} P(T_i).$$

Substituting equations (A.9)–(A.12) into (A.8) by replacing A_k with either D_k or M_k and assuming $\mathbf{T}^{(n+1)} = \mathbf{T}^{(n)}$ finally yields in equations (A.13) and (A.14):

$$T_i^{n+1} = \frac{1}{\tau_i^*} T_i^n \sum_k \frac{R^*_{ki} \cdot D_k}{\sum_j R^*_{kj} \cdot T_j^n} \tag{A.13}$$

and

$$T_i^{n+1} = \frac{1}{\tau_i} T_i^n \sum_k \frac{R_{ki} \cdot M_k}{\sum_j R_{kj} \cdot T_j^n}, \tag{A.14}$$

with the iteration index n and the mean number of triggered pixels per incident photon $\tau_i^* = \sum_k R^*_{ki}$ (respective $\tau_i = \sum_k R_{ki}$).

2012 JINST 7 P03003

B Tabulated values

Table 2. Monoenergetic conversion coefficients for air kerma per unit fluence [15].

Energy in keV	K_a/Φ in pGycm^2
10	7,43
15	3,12
20	1,68
30	0,721
40	0,429
50	0,323
60	0,289
80	0,307
100	0,371
150	0,599
200	0,856
300	1,38
400	1,89
500	2,38
600	2,84
800	3,69
1000	4,47
1500	6,14
2000	7,55
3000	9,96

Table 3. Filtration and anode types for different radiation qualities ([5] and [16]).

	N-40	WMH-28	RRV-28	RRH-28
anode	tungsten	tungsten	rhodium	rhodium
kVp	40	28	28	28
filtration in mm	4.0 (Al) 0.21 (Cu)	2.0 (Al) 0.06 (Mo)	0.025 (Rh)	2.0 (Al) 0.025 (Rh)

Acknowledgments

This work was carried out within the Medipix Collaboration.

References

[1] T. Michel, P. Takoukam-Talla, M. Firsching, J. Durst, M. Böhnel and G. Anton, *Reconstruction of X-ray spectra with the energy sensitive photon counting detector Medipix2*, *Nucl. Instrum. Meth.* **A 598** (2009) 510.

[2] J. Giersch and J. Durst, *Monte Carlo simulations in X-ray imaging*, *Nucl. Instrum. Meth.* **A 591** (2008) 300.

[3] X. Llopart, M. Campbell, R. Dinapoli, D. San Segundo and E. Pernigotti, *Medipix2: A 64-k pixel readout chip with 55-μm square elements working in single photon counting mode*, *IEEE Trans. Nucl. Sci.* **49** (2002) 2279.

[4] X. Llopart, R. Ballabriga, M. Campbell, L. Tlustos and W. Wong, *Timepix, a 65k programmable pixel readout chip for arrival time, energy and/or photon counting measurements*, *Nucl. Instrum. Meth.* **A 581** (2007) 485.

[5] *ISO 4037-1: X and gamma reference radiation for calibrating dosemeters and doserate meters and for determining their response as a function of photon energy — part I: Radiation characteristics and production methods*, (1996).

[6] T. Michel et al., *A fundamental method to determine the signal-to-noise ratio (SNR) and detective quantum efficiency (DQE) for a photon counting pixel detector*, *Nucl. Instrum. Meth.* **A 568** (2006) 799.

[7] S. Sze, *Physics of Semiconductor Devices*, second edition, Wiley-Interscience (1981).

[8] E. Guni et al., *The Influence of Pixel Pitch and Electrode Pad Size on the Spectroscopic Performance of a Photon Counting Pixel Detector With CdTe Sensor*, *IEEE Trans. Nucl. Sci.* **58** (2011) 17.

[9] B. Kreisler, J. Durst, T. Michel and G. Anton, *Generalised adjoint simulation of induced signals in semiconductor X-ray pixel detectors*, 2008 *JINST* **3** P11002.

[10] T. Kennett, W. Prestwich, and A. Robertson, *Bayesian deconvolution I: Convergent properties*, *Nucl. Instrum. Meth.* **151** (1978) 285.

[11] G. D'Agostini, *A Multidimensional unfolding method based on Bayes' theorem*, *Nucl. Instrum. Meth.* **A 362** (1995) 487.

[12] T. Bayes and R. Price, *An Essay towards Solving a Problem in the Doctrine of Chances. By the Late Rev. Mr. Bayes, F. R. S. Communicated by Mr. Price, in a Letter to John Canton, A. M. F. R. S.*, *Philos. Trans. R. Soc. London* **53** (1763) 370.

[13] U. Ankerhold, *Catalogue of X-ray spectra and their characteristic data - ISO and DIN radiation qualities, therapy and diagnostic radiation qualities, unfiltered X-ray spectra*, Physikalisch Technische Bundesanstalt (2000).

[14] U. Ankerhold and R. Berens, *X Ray Spectrometry of Low Energy Photons for Determining Conversion Coefficients from Air Kerma, Ka, to Personal Dose Equivalent, Hp (10), for Radiation Qualities*, *Radiat. Prot. Dosim.* **81** (1999) 247.

[15] ICRU Report, *Conversion Coefficients for use in Radiological Protection against External Radiation*, volume 57. International Commission on Radiation Units and Measurements, (1994).

[16] L. Büermann, *PTB Radiation qualities for Calibration of secondary standards*, Homepage of PTB http://www.ptb.de/en/org/6/62/625/pdf/strhlq.pdf (visited at 6th December 2011).

2012 JINST 7 P03003

PUBLISHED BY IOP PUBLISHING FOR SISSA MEDIALAB

RECEIVED: *July 16, 2012*
ACCEPTED: *July 20, 2012*
PUBLISHED: *August 13, 2012*

Erratum: Bayesian deconvolution as a method for the spectroscopy of X-rays with highly pixelated photon counting detectors

P. Sievers,[a,b,1] **T. Weber,**[b] **T. Michel,**[b] **J. Klammer,**[a] **L. Büermann**[a] **and G. Anton**[b]

[a] *Physikalisch-Technische Bundesanstalt (PTB), Bundesallee 100, D-38116 Braunschweig, Germany*
[b] *Radiation Physics Group, Erlangen Centre for Astroparticle Physics (ECAP), University of Erlangen-Nürnberg, Erwin-Rommel-Str. 1, D-91058 Erlangen, Germany*

E-mail: peter.sievers@ptb.de

ERRATUM TO: 2012 JINST 7 P03003

The equations below replace equations (4.12) in section 4.3, which contain errors.

$$\begin{aligned} var\,(b_0) &= var\,(a_0)\cdot b_1^2 + 2\cdot cov\,(a_0,a_1)\cdot b_0\cdot b_1^2 + b_0^2\cdot b_1^2\cdot var\,(a_1) \\ var\,(b_1) &= var\,(a_1)\cdot b_1^4 \\ cov\,(b_0,b_1) &= cov\,(a_0,a_1)\cdot b_1^3 + var\,(a_1)\cdot b_0\cdot b_1^3 . \end{aligned} \tag{4.12}$$

This equation has been printed wrongly in the text only, all given values and figures have been calculated with the correct formula (4.12).

[1] Corresponding author.

doi:10.1088/1748-0221/7/08/E08001

2012 JINST 7 E08001

3.2 Position-resolved spectrometry

In the preceding section it is shown that the Bayesian deconvolution is a very competitive tool for calculating the impinging spectrum in both aspects: the absolute photon fluence and the shape of the spectrum. As it even turned out to be very stable in terms of bin sizes and the minimum required photon flux, in the next step I evaluated the possibilities of facilitating small ROIs for the deconvolution of the impinging spectrum. Until now the detector has been calibrated globally. Due to a energy spread of the energy threshold (THL) along the columns of the pixel matrix, it became immanent for the analysis of small ROI to have each pixel energy-calibrated on its own. As a first result the energy resolution improves. This newly developed calibration method has then been applied for measuring the anode heel effect of an X-ray tube.

3.2.1 Pixel-by-pixel energy calibration and anode heel effect

Publication: Pixel-by-pixel energy calibration and anode heel effect

In this paper I have given an introduction to the Timepix detector and to the anode heel effect that has been analyzed. Furthermore, I developed a new pixel-by-pixel energy calibration that also improves the energy resolution by about 40 %. Next, the measurement setup and the resulting spectra are shown. I was able to demonstrate the angular dependence of the absorption of photons in the anode of the X-ray tube on both the shape of the X-ray spectrum emitted and on the absolute kerma rate. An impact of aging effects of the anode on the heel effect could not be observed.
This work is published in the Journal of Instrumentation by IOP Publishing (`http://iopscience.iop.org/1748-0221/`) as:
Peter Sievers et al. 'Improving the spectral resolution of a highly pixelated detector by applying a pixel-by-pixel energy calibration for investigating the spectral properties of the anode heel effect'. In: *Journal of Instrumentation* 7.07 (July 2012). DOI: `10.1088/1748-0221/7/07/P07011`;

Contributions of the co-authors:

- running a facility with reference equipment at PTB
- performing the comparative measurements with the image plate
- scientific discussion

My own contributions:

- development of a pixel-by-pixel energy calibration method
- development of an analysis tool for calculating the intensities of a THL scan and their uncertainties for a given ROI
- performing the measurements with the Timepix detector
- performing the analysis

PUBLISHED BY IOP PUBLISHING FOR SISSA MEDIALAB

RECEIVED: *May 16, 2012*
ACCEPTED: *June 12, 2012*
PUBLISHED: *July 9, 2012*

Improving the spectral resolution of a highly pixelated detector by applying a pixel-by-pixel energy calibration for investigating the spectral properties of the anode heel effect

P. Sievers,[a,b,1] **J. Klammer,**[a] **T. Michel,**[b] **O. Hupe**[a] **and G. Anton**[b]

[a] *Physikalisch-Technische Bundesanstalt (PTB), Bundesallee 100, D-38116 Braunschweig, Germany*

[b] *Radiation and Detector Physics, Erlangen Centre for Astroparticle Physics (ECAP), University of Erlangen-Nürnberg, Erwin-Rommel-Str. 1, D-91058 Erlangen, Germany*

E-mail: peter.sievers@ptb.de

ABSTRACT: The energy deposition spectrum measured with highly pixelated photon-counting pixel detectors with a semiconductor sensor layer (e.g. silicon) differs significantly from the impinging X-ray spectrum. This is the main disadvantage compared to commonly known X-ray spectrometers, e.g. high purity Germanium (hpGe) detector. On the other hand, those hpGe-detectors have a lack of spatial resolution and can not be used for energy-resolved imaging. In case of measurements with highly pixelated detectors, a set of monoenergetic detector response functions is needed for the deconvolution of the measured distribution into the impinging spectrum.

We have investigated the possibility of applying a pixel-by-pixel calibration on a highly pixelated detector for gaining a higher energy resolution and for lowering the minimal flux needed for the deconvolution. As a result it is now possible to utilize small ROIs of the pixel matrix for the deconvolution. With this analysis method the detector enables spectral X-ray imaging of high photon rates. This is in particular shown for the angular dependency of the anode heel effect on the emitted spectrum.

KEYWORDS: Data processing methods; X-ray detectors; Spectrometers; X-ray generators and sources

[1] Corresponding author.

doi:10.1088/1748-0221/7/07/P07011

2012 JINST 7 P07011

Contents

1 Introduction **1**
1.1 Anode heel effect 2
1.2 Timepix detector 2

2 Applied methods **2**
2.1 Energy calibration 2
2.2 Setting ROIs and their uncertainties 4
2.3 Deconvolution 4

3 Results of the new energy calibration **5**

4 Measurement of the heel effect **6**
4.1 Measurement setup 6
4.2 Resulting spectra 7
4.3 Aging effects of the anode 10

5 Conclusion **10**

A Details of the fitting procedure **11**

2012 JINST 7 P07011

1 Introduction

Spectrometry of X-ray radiation is a widely used application, for instance, in the determination of X-ray tube spectra, synchrotron light spectra, radioactive material composition, and in astronomy. The conventional way of measuring the spectrum with semiconductor devices (e.g. a high purity germanium detector) is to detect the charge carriers released by the impinging photons. As the amount of charge corresponds to the deposited energy, it is necessary to collect at least the complete charge of one charge carrier type. Furthermore, in the absence of an absorption edge the absorption probability decreases with increasing photon energy. To cope with the requirements of high detection efficiency and energy determination one has to use relatively large and thick semiconductors. This ensures that every photon gets fully absorbed and that any released charge remains within the sensor. As those detectors are not pixelated, one has no spatial resolution. In case of the anode heel effect one would have to perform multiple measurements under different angles. In that case there are a lot of alignment problems (collimation etc.) and therefore a comparison of the absolute fluence is hard to achieve.

In contrast, pixelated detectors have a spatial resolution and they can be operated at the full radiation flux without any collimation, which avoids the alignment problems. Therefore, the spectral properties at different angles can be measured within one single measurement.

If the detector setup and the interaction processes in the detector are implemented correctly in a Monte Carlo simulation, the impinging spectrum can be computed by the deconvolution of the measured data [1]. The simulation of the detector response functions has been conducted with the simulation framework ROSI (RoentgenSimulation) [2]. This framework is based on EGS4 with low energy extensions.

One aim of this work is to introduce a fast and reliable method for a pixel-by-pixel energy calibration. This is the most crucial part for gaining the advantage of the pixelation and thus the spatial resolution.

1.1 Anode heel effect

In most standard X-ray equipment for medical applications X-ray tubes with rotating anodes and low anode angles are used. In an X-ray tube the emitted electrons from the cathode hit the anode and release, according to the applied acceleration voltage, photons in different depths of the anode material. Passing along the anode, taking different paths, the released photons experience more or less self-absorption due to the anode geometry. As a result, the anode heel effect is more pronounced for low anode angles (rotating anodes), than for larger anode angles (stationary anodes). The influence of the anode heel effect on the dose rate distribution of the radiation field increases with decreasing mean energy, and can increase furthermore as the anode surface roughens due to the effects of aging [3].

1.2 Timepix detector

For the measurements described in this paper, a Timepix detector [4] in counting mode was used. It consists of an application-specific integrated circuit (ASIC) which has 256 x 256 pixel cells with a 55 μm pixel pitch. As a sensor material, a silicon layer with a thickness of 300 μm was bump-bonded to the ASIC. Each pixel cell of the ASIC consists of an analogue and a digital electronics part. In the analogue part of each pixel it is possible to set a global energy threshold E_{dig}. This energy threshold value is transferred via a digital analog converter (DAC) into a reference voltage. If the voltage pulse caused by the amplified signal of the collected charge is higher compared to this reference voltage, the counter in the digital part of the corresponding pixel gets incremented ([5, section II,A,2] and [4, section 2.1]). By increasing this energy threshold E_{dig} gradually, the distribution D of X-ray photons with respect to their deposited energy in the sensor will be scanned:

$$M\left(E_{\mathrm{dig}}\right) = \int_{E_{\mathrm{dig}}}^{\infty} D\left(E\right) dE. \tag{1.1}$$

This procedure is described in detail in [1].

The problem with this method is that a globally set threshold E_{dig} is translated into a different reference voltage and therefore represents a different corresponding energy in each pixel. This makes it impossible to analyze small ROIs with a global energy calibration.

2 Applied methods

2.1 Energy calibration

For applying a pixel-by-pixel energy calibration, the method proposed in [1, section 4.3] has to be slightly changed. Firstly, the distribution of deposited energy $\vec{D}$ could no longer be used for

2012 JINST 7 P07011

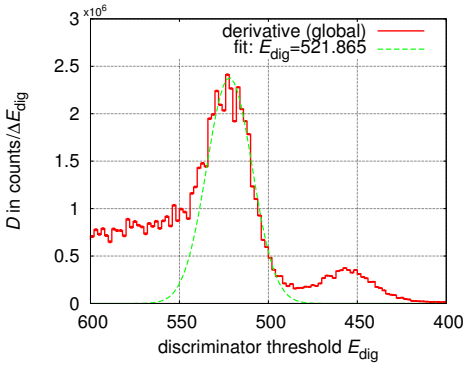

(a) Derivative shown for the total pixel matrix and a normal density function fitted to its full energy peak with $\bar{E}_{\mathrm{dig}} = 521.87$ (green dashed line).

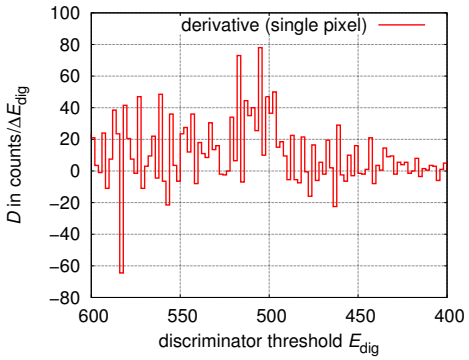

(b) Derivative shown for a single pixel.

Figure 1. Derivative of a threshold scan measured during irradiation by a Gd K_α fluorescence source (red line) for the total pixel matrix (a) and for a single pixel (b).

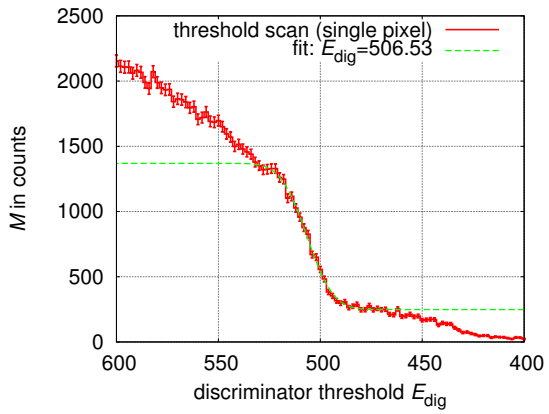

Figure 2. Threshold scan for a single pixel measured during irradiation by a Gd K_α fluorescence source (red line) and a normal distribution function (equation (2.1)) fitted to its full energy peak with $\bar{E}_{\mathrm{dig}} = 506.53$ (green dashed line).

fitting a normal density function on the full energy peak as it has been done for the global calibration (figure 1a). This is due to the very low statistics in a single pixel causing a lot of oscillations in the derivative (figure 1b). This problem can be solved by fitting a normal distribution function $f\left(E_{\mathrm{dig,pixel}}\right)$ directly on the measured signal of a single pixel:

$$f\left(E_{\mathrm{dig,pixel}}\right) = c_{1,\mathrm{pixel}} \cdot \left(0.5 + 0.5 \cdot \mathrm{erf}\left(\frac{E_{\mathrm{dig,pixel}} - \bar{E}_{\mathrm{dig,pixel}}}{\sqrt{2} \cdot \sigma_{\mathrm{pixel}}}\right)\right) + c_{0,\mathrm{pixel}}. \tag{2.1}$$

The fitting parameters are: the mean position $\bar{E}_{\mathrm{dig,pixel}}$, the peak width σ_{pixel}, the offset $c_{0,\mathrm{pixel}}$ and the slope $c_{1,\mathrm{pixel}}$. The result of such a fit is shown in figure 2. Secondly, this fit of a normal

2012 JINST 7 P07011

distribution function and the final fit of the calibration curve

$$E_{\text{photon}} = b_{0,\text{pixel}} + b_{1,\text{pixel}} \cdot E_{\text{dig,pixel}} \tag{2.2}$$

have to be performed in an automated way for each pixel.

The detailed fitting procedure including flowcharts can be found in appendix A.

2.2 Setting ROIs and their uncertainties

In general the offset $b_{0,\text{pixel}}$ and the slope $b_{1,\text{pixel}}$ of the calibration line vary from pixel to pixel and thus the energy channel width ΔE_{pixel} is not constant over the pixel matrix although the ΔE_{dig} is. To compensate this, all pixels of a chosen ROI have to be rebinned to the same energy channel width ΔE_{ROI}. Afterwards the corresponding bins of the new histograms are summarized, which results in a single measurement $\vec{M}_{\text{ROI}}$ for the complete ROI.

This rebinning process is also done for the standard deviation $s\left(M_{i,\text{pixel}}\right) = \sqrt{M_{i,\text{pixel}}}$ in a quadratic way and for the systematic calibration uncertainty $u\left(E,\text{pixel}\right)$ (equation (A.5)) in a linear way. This results in the global deviations $s\left(M_{i,\text{ROI}}\right)$ and $u\left(E_i,\text{ROI}\right)$ of the chosen ROI. The calibration uncertainty $u\left(E_i,\text{ROI}\right)$ can again be seen as the probability that the counts $M_{i,\text{ROI}}$ are misassigned to a neighbouring energy channel $E_{i\pm z}$. Therefore, we can describe the systematic uncertainty $u\left(M_{i,\text{ROI}}\right)$ by a weighted difference of counts in neighbouring channels:

$$u\left(M_{i,\text{ROI}}\right) = \left|\frac{M_{i-1,\text{ROI}} - M_{i+1,\text{ROI}}}{E_{i-1} - E_{i+1}}\right| \cdot u\left(E_i,\text{ROI}\right). \tag{2.3}$$

The propagation of the standard deviation and the systematic uncertainty leads to the total uncertainty

$$u_{\text{total}}\left(M_{i,\text{ROI}}\right) = \sqrt{s\left(M_{i,\text{ROI}}\right)^2 + u\left(M_{i,\text{ROI}}\right)^2}. \tag{2.4}$$

The calculated $\vec{M}_{\text{ROI}}$ and its total uncertainty $\vec{u}_{\text{total,ROI}}$ are then used for the deconvolution process.

2.3 Deconvolution

For the deconvolution a Bayesian approach was chosen, as it turned out to be very stable and reliable [1, section 5]. The iterative formula used is:

$$T^{n+1}_{i,\text{ROI}} = \frac{1}{\tau_i} T^{n}_{i,\text{ROI}} \sum_k \frac{R_{ki} \cdot M_{k,\text{ROI}}}{\sum_j R_{kj} \cdot T^{n}_{j,\text{ROI}}}, \tag{2.5}$$

with the iteration index n, the mean number of triggered pixels per incident photons $\tau_i = \sum_k R_{ki}$ and i, k, j denoting the channel index of the measurement $\vec{M}_{\text{ROI}}$ and the impinging spectrum $\vec{T}_{\text{ROI}}$ of the chosen ROI.

The exit condition for this iterative process is defined in the following. For each iteration step, the "virtual measurement" $\vec{M}_{\text{v,ROI}}$ is computed by the convolution of the detector response functions $\hat{R}$ with the unfolded spectrum $\vec{T}^{n+1}_{\text{ROI}}$ of the actual iteration step:

$$\vec{M}_{\text{v,ROI}} = \hat{R} \cdot \vec{T}^{n+1}_{\text{ROI}}. \tag{2.6}$$

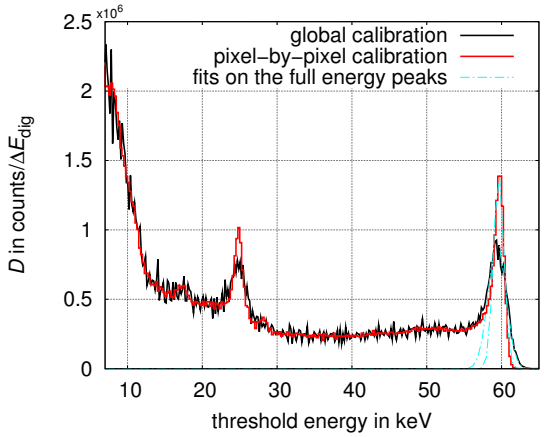

Figure 3. Derivative of a threshold scan measured during irradiation of Am-241. Both graphs are for the same measured data.

If the condition

$$\chi^2 = \frac{\sum_{i=1}^{N} \left(\frac{M_{\mathrm{v},i,\mathrm{ROI}} - M_{i,\mathrm{ROI}}}{u_{\mathrm{total}}(M_{i,\mathrm{ROI}})} \right)^2}{N} \leq 1 \tag{2.7}$$

is reached, the iteration process is stopped and the actual $\vec{T}^{(n+1)}$ is regarded as the true impinging spectrum T.

3 Results of the new energy calibration

As a direct consequence of the pixel-by-pixel calibration, the energy resolution of the measured threshold scan, or the distribution of deposited energy, respectively, can be improved. This is, for instance, shown in figure 3 for the irradiation with an Am-241 source. A normal density function was fitted on the full energy peaks for both the global analysis and the single-pixel analysis (section 2.2). In both cases the complete detector pixel matrix was set as the analyzed ROI. For the global calibration one derives a $FWHM = 2.8\,\mathrm{keV}$ ($FWHM/E = 4.6\%$) and for the pixel-by-pixel calibration those values can be lowered to $FWHM = 1.6\,\mathrm{keV}$ ($FWHM/E = 2.7\%$). In this case of the peak at $E_{photon} = 59.6\,\mathrm{keV}$ there is an improvement in energy resolution of about 42%. As it is also possible to determine the energy resolution directly by the fitting parameters of equation (2.1), the change in energy resolution depending on the energy of the calibration points is shown in figure 4a:

$$\Delta E/E = \frac{\sum_{\mathrm{pixel}} b_{1,\mathrm{pixel}} \cdot \sigma_{\mathrm{pixel}}}{N_{\mathrm{pixel}}} \cdot \frac{2 \cdot \sqrt{2 \ln 2}}{\bar{E}_{\mathrm{photon}}}. \tag{3.1}$$

Figure 4b shows the energy-dependent improvement of the energy calibration. The visible increase of the improvement for higher energies is due to the fact that the thresholds of all pixels have been equalized at the noise floor (at low energies) and therefore the pixel to pixel spread increases towards higher energies. This spread, being visualized by the effective threshold given for a global set threshold at a corresponding energy of 42.5 keV, is, for instance, shown in figure 5. The reason for this behaviour is a voltage drop of the reference voltage along the columns of the pixel matrix.

2012 JINST 7 P07011

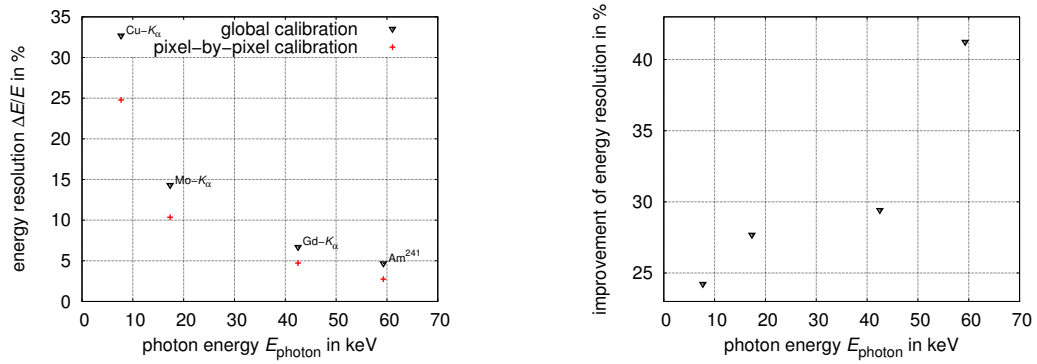

(a) Energy resolution of the Timepix detector used.

(b) Improvement of the energy resolution.

Figure 4. Comparison of the energy resolution of the detector calibrated globally and pixel-by-pixel in absolute numbers (a) and relative (b).

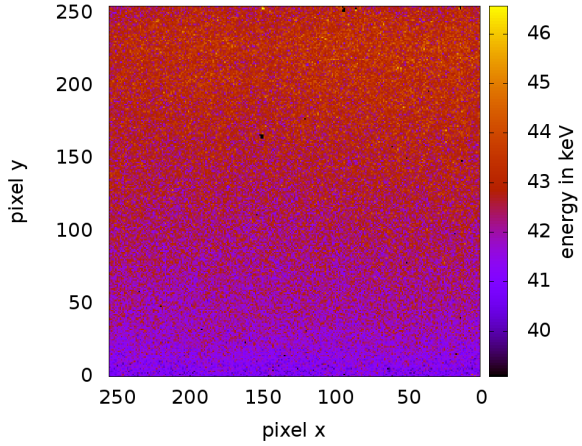

Figure 5. Effective energy threshold of each pixel for the global set threshold $E_{\mathrm{dig}} = 522$ that corresponds globally to an energy of 42.5 keV.

4 Measurement of the heel effect

4.1 Measurement setup

With those methods it is now possible to measure the influence of the anode heel effect on the emitted spectrum. The X-ray tube examined is a Siemens Megalix [3]. The anode angle α of this tube is $\alpha = 8°$. The detector was placed at the nearest possible position towards the focus to cover a high angular range. Due to the enclosure of the tube and other parts (ionization chamber, filters etc.) the minimal distance is 32 cm. Due to the detector dimensions of 14.08 x 14.08 mm^2 this distance corresponds to a maximal angular range of $\pm 1.26°$. To cover a wider range, the detector was shifted perpendicularly to the beam axis to different positions. Those positions and the analyzed angles β are indicated in figure 6. As there should only be a lateral change in the spectrum caused by the heel effect, one should not see a spectral change in one column (see [3, figure 6]). Therefore, all of the 256 pixels in one column have been used. To gain higher statistics in

2012 JINST 7 P07011

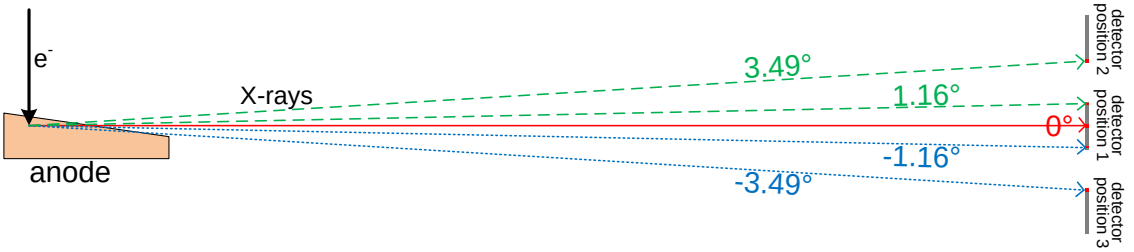

Figure 6. Setup for the measurement of the anode heel effect with a Timepix detector. All dimensions are in scale except those for the anode. The small red dots at the detector mark the effective columns used of the detector (660 μm), this results in an effective area of $0.66\,\text{x}\,14.08\,\text{mm}^2 = 9.293\,\text{mm}^2$.

Table 1. Settings of both the X-ray tube and Timepix detector.

radiation quality	N-40	X-40
tube voltage in kV	40	40
filtration	4.0 mm (Al) 0.21 mm (Cu)	intrinsic
current	15 mA	0.5 mA
mean energy $\bar{E}$	33.3 keV	n.n.
total measuring time per detector position	42 min	42 min
measuring time per threshold and position	10 s	10 s

the measurement, the sum of 12 columns was taken. This gives an ROI of in total $12 \cdot 256\,\text{pixel} = 3072\,\text{pixel} \mathrel{\widehat{=}} 0.66 \cdot 14.08\,\text{mm}^2 = 9.293\,\text{mm}^2$. Due to this lateral spread each given angle β has a width of $\approx \pm 0.06°$. All further results shown are corrected for the resulting difference in distance and area. The parameters of the settings for the X-ray tube and the detector are given in table 1.

4.2 Resulting spectra

For the three positions marked in figure 6, a threshold scan has been taken and analyzed for the five marked ROIs. In a first step a radiation quality N-40 [6] has been analyzed. The deconvoluted spectra can be seen in figure 7 using the three positions and figure 8 for a single detector position. In both figures 7a and 8a the increasing drop in intensity due to a higher self absorption towards lower angles is clearly visible. The expected shift of the mean energy $\bar{E}$ towards higher energies by lowering the angle β is barely visible in the normalized spectra (figure 7b and 8b). For a quantitative analysis of the intensity, the air kerma rate $\dot{K}_\text{a}$ was calculated by folding the measured fluence spectrum with the interpolated conversion coefficients for kerma per unit fluence $\frac{K_\text{a}}{\Phi}$ [7, table A.1]. Those calculated values for the different angles are given in table 2. The indicated statistical uncertainty has been calculated by applying the deconvolution 10 000 times on the measurement $\vec{M}$, which has been pertubated by its standard deviation.

The comparison of the calculated relative change in air kerma rate and an intensity profile measured with an image plate[1] [3, figure 6] are shown in figure 9. Although the measured intensity

[1] Type: BAS-MS 2040, Fujifilm.

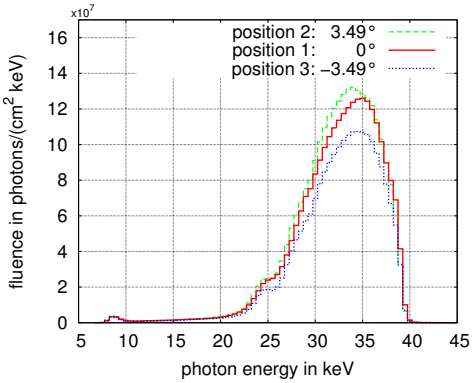

(a) Absolute fluence spectrum.

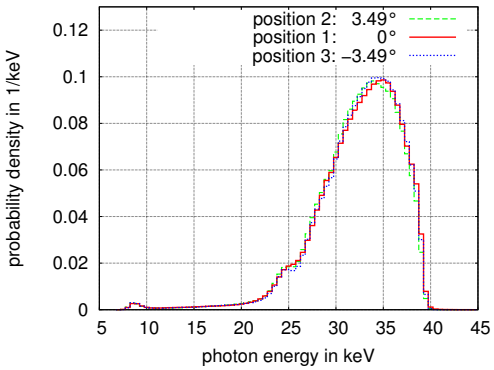

(b) Normalized spectrum.

Figure 7. Spectrum of the radiation quality N-40 determined with the Bayesian deconvolution method for different angles measured at three detector positions indicated in figure 6 in absolute values (a) and normalized (b).

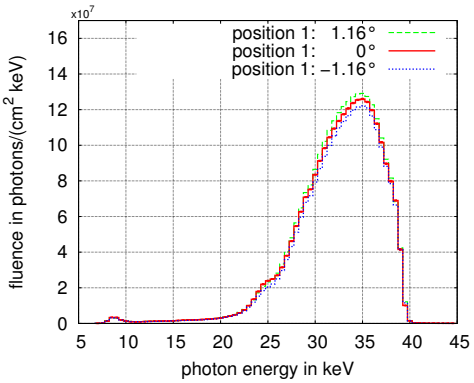

(a) Absolute fluence spectrum.

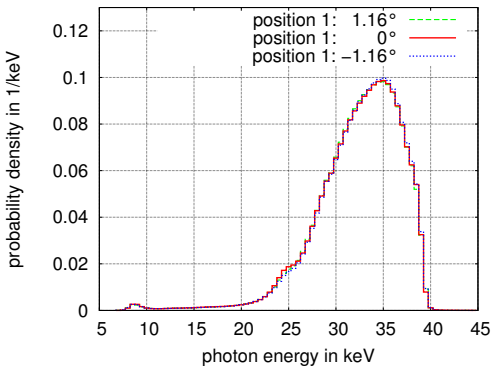

(b) Normalized spectrum.

Figure 8. Spectrum of the radiation quality N-40 determined with the Bayesian deconvolution method for different angles measured at a single detector position indicated in figure 6 in absolute values (a) and normalized (b).

Table 2. Determined absolute values for the analyzed radiation quality N-40 at different beam angles β and the relative changes to $\beta = 0°$.

beam angle	mean energy $\bar{E}$	rel. change of $\bar{E}$	air kerma rate $\dot{K}_a$	rel. change of $\dot{K}_a$
3.49°	32.3 ± 0.04 keV	(-1 ± 0.2) %	331 ± 0.2 mGy/h	(6 ± 0.1) %
1.16°	32.4 ± 0.03 keV	(0 ± 0.1) %	321 ± 0.2 mGy/h	(2.9 ± 0.08) %
0.00°	32.4 ± 0.04 keV		312.1 ± 0.18 mGy/h	
−1.16°	32.5 ± 0.03 keV	(0 ± 0.2) %	298 ± 0.2 mGy/h	(-4.6 ± 0.08) %
−3.49°	32.5 ± 0.05 keV	(0 ± 0.2) %	262 ± 0.2 mGy/h	(-16.1 ± 0.09) %

2012 JINST 7 P07011

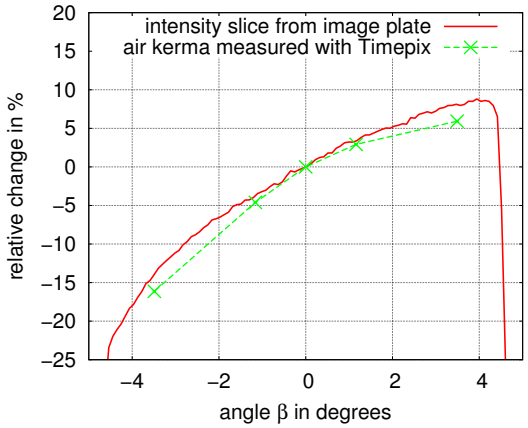

Figure 9. Comparison of the relative change in intensity distribution measured with an image plate and in air Kerma rate calculated with the deconvolved spectra measured with a Timepix detector - both for the radiation quality N-40.

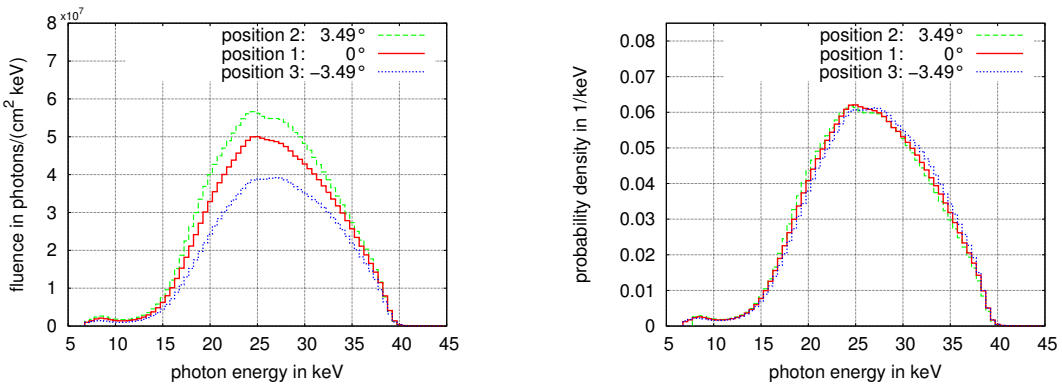

(a) Absolute fluence spectrum.

(b) Normalized spectrum.

Figure 10. Spectrum of unfiltered radiation X-40 determined with the Bayesian deconvolution method for different angles measured at three detector positions indicated in figure 6 in absolute values (a) and normalized (b).

and the calculated kerma rate are quite different quantities, they show a good agreement in their relative change.

As the N-40 radiation quality is a filtered one (table 1), the effect of the self absorption in the anode is suppressed as both filtrations have a higher effect towards the lower energies. To compensate this and for getting a maximal impact of the heel effect on the spectrum, an unfiltered X-ray radiation quality (X-40) was chosen for further investigations. The resulting spectra are shown in figures 10 and 11. Again the increasing drop of intensity towards lower angles is very distinct and consistent with the values for the kerma rate given in table 3. As the heel effect is significantly pronounced compared to the N-40 radiation quality, even the energy shift is clearly visible in the normalized spectra seen in figures 10b and 11b. The absolute and relative values for the energy shift are given in table 3. By comparing the relative change in kerma rate and energy

2012 JINST 7 P07011

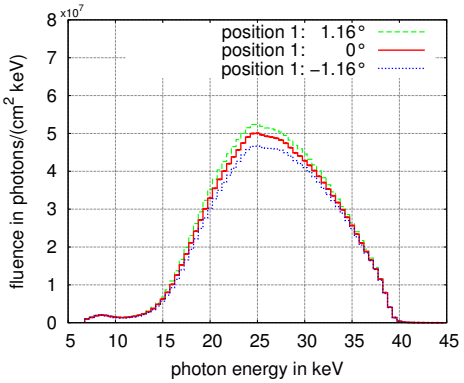

(a) Absolute fluence spectrum.

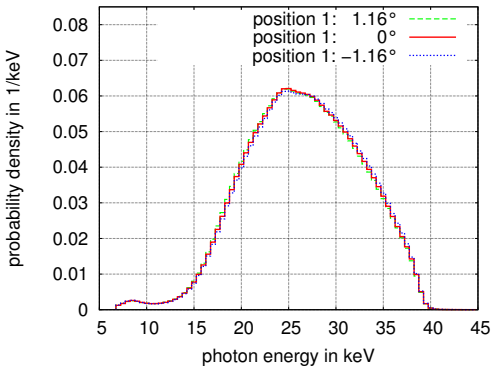

(b) Normalized spectrum.

Figure 11. Spectrum of unfiltered radiation X-40 determined with the Bayesian deconvolution method for different angles measured at a single detector position indicated in figure 6 in absolute values (a) and normalized (b).

Table 3. Determined absolute values for the analyzed unfiltered radiation quality X-40 at different beam angles β and the relative changes to $\beta = 0°$.

beam angle	mean energy $\bar{E}$	rel. change of $\bar{E}$	air kerma rate $\dot{K}_a$	rel. change of $\dot{K}_a$
3.49°	26.3 ± 0.01 keV	(-0.9 ± 0.06) %	371.8 ± 0.07 mGy/h	(16.0 ± 0.03) %
1.16°	26.5 ± 0.01 keV	(-0.3 ± 0.06) %	339.0 ± 0.07 mGy/h	(5.8 ± 0.03) %
0.00°	26.5 ± 0.01 keV		320.5 ± 0.06 mGy/h	
−1.16°	26.7 ± 0.01 keV	(0.4 ± 0.06) %	299.4 ± 0.06 mGy/h	(-6.6 ± 0.03) %
−3.49°	26.9 ± 0.01 keV	(1.2 ± 0.06) %	247.8 ± 0.05 mGy/h	(-22.7 ± 0.03) %

shift (tables 2 and 3), the self-absorption of the anode has a higher impact on the spectrum for the unfiltered radiation than for the filtered N-40 quality.

4.3 Aging effects of the anode

For testing the assumption as to whether the aging of the anode (roughening of the surface) has an impact on the heel effect, the measurements for the unfiltered radiation quality X-40 were repeated sequentially. The first measurements started at $\approx 5.6\%$ of the expected tube lifetime[2] after all tests and adjustments had been accomplished. The last measurement (23.08.2011) was taken at 11.0% of the lifetime. For both mean energy $\bar{E}$ (figure 12b) and kerma rate $\dot{K}_a$ (figure 12a) no impact of a possible anode aging on the anode heel effect can be observed during this time interval.

5 Conclusion

In this paper we have shown that a pixel-by-pixel energy calibration of a highly pixelated detector performs very well and that it is reliable without a high computing effort. It is in particular shown for the Timpix detector but should in general be adoptable for a wide range of detectors. A di-

[2]The accumulated stress of the tube is arbitrarily calculated and compared to a value given by the vendor.

2012 JINST 7 P07011

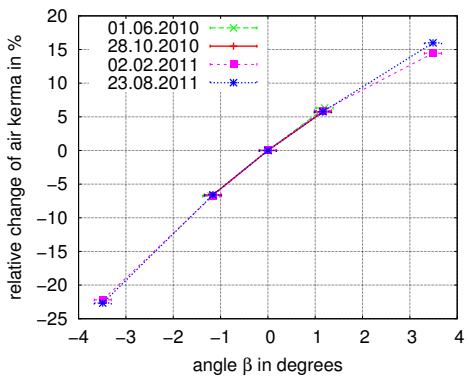

(a) Change in air kerma rate $\dot{K}_a$.

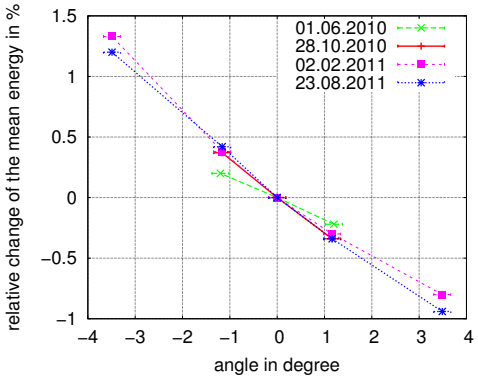

(b) Change in mean energy $\bar{E}$.

Figure 12. Relative changes of the air kerma rate $\dot{K}_a$ (a) and the mean energy $\bar{E}$ (b) measured for an unfiltered X-ray quality X-40 at different times. The error bars at the x-values are due to an expected uncertainty in positioning the detector at the same lateral position of 1 mm.

rect consequence of such a calibrated detector is an improvement in energy resolution — for the Timepix detector up to 42%.

Secondly, it is now possible to carry out real spectrometric imaging by deconvolution of the spectra of small ROIs down to 4 by 4 pixels [8]. In this paper we have focused on the investigation of the anode heel effect. It was possible to show the impact of the self-absorption on the fluence spectrum, both for the shift of the mean energy and for the absolute kerma rate. An impact of aging effects on the heel effect could not be observed.

Those kind of measurements can be used in the field of quality assurance — for improving X-ray tubes and for designing new filter geometries to reduce the impact of the anode heel effect in the field of medical imaging.

A Details of the fitting procedure

In the following the detailed fitting procedure of the energy calibration mentioned in section 2.1 is described.

In the first step the position of the fluorescence line $\bar{E}_{\text{dig,pixel}}$ and its variance $s^2\left(\bar{E}_{\text{dig,pixel}}\right)$ have to be determined for each pixel separately. This has to be done for each chosen calibration energy. Secondly, the calibration line is fitted on at least three calibration points.

The fitting procedure for a single calibration point will be shown with the example of the Gd K_α fluorescence. At a first step, the corresponding energy is being determined by fitting the calibration function

$$f\left(E_{\text{photon}}\right) = c_1 \cdot \left(0.5 + 0.5 \cdot \text{erf}\left(\frac{\bar{E}_{\text{photon}} - E_{\text{photon}}}{\sqrt{2} \cdot \sigma_{\text{simulation}}}\right)\right) + c_0 \tag{A.1}$$

on the simulated detector response (first blue paragraph in figure 13). This associated photon energy $\bar{E}_{\text{photon}}$ is the same for all pixels. The exact fitting behaviour is the same as the one for a single pixel. In a next step the threshold scan is loaded and for each of the 65 536 pixels the calibration fit is performed (figure 13, second blue box).

2012 JINST 7 P07011

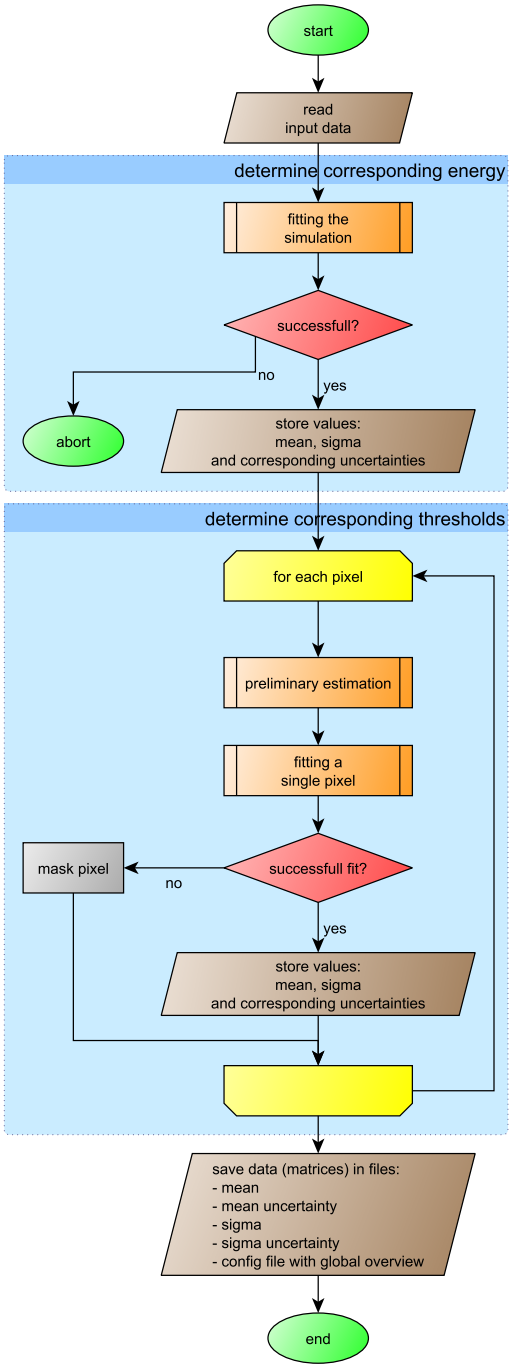

Figure 13. Flowchart of an overview of the implemented pixel-by-pixel fitting procedure. The details of the preliminary estimation and the pixel-by-pixel fit (the same as the fit for the simulation) are shown in figure 14.

2012 JINST 7 P07011

As the pixel-to-pixel spread of the $\bar{E}_{\text{dig,pixel}}$ can be up to ± 100 there has to be an initial estimation for a starting value of the fitting process. This is illustrated in the flowchart of figure 14a. Firstly, the global peak position $\bar{E}_{\text{dig,global}}$ is passed to the fitting routine. Secondly, the threshold scan is rebinned to $\Delta E_{\text{dig,pixel}} = 20$ in a threshold range of $1.1 \cdot \bar{E}_{\text{dig,global}} - 200$ to $0.9 \cdot \bar{E}_{\text{dig,global}} + 200$.[3] Then the derivative $\vec{D}_{\text{range,rebinned}}$ of this range is calculated. The position of the maximum of this derivative $\vec{D}_{\text{range,rebinned}}$ is taken as the starting value $\bar{E}_{\text{dig,pixel}}$ for the fit of the normal distribution function.

After the preliminary estimation is accomplished, the initial threshold scan of the pixel is used, and the fit is applied on it with the formerly calculated starting values:

$$f\left(E_{\text{dig,pixel}}\right) = c_{1,\text{pixel}} \cdot \left(0.5 + 0.5 \cdot \text{erf}\left(\frac{E_{\text{dig,pixel}} - \bar{E}_{\text{dig,pixel}}}{\sqrt{2} \cdot \sigma_{\text{pixel}}}\right)\right) + c_{0,\text{pixel}}. \tag{A.2}$$

This process is illustrated in the flowchart of figure 14b. The threshold range in this case is from $\bar{E}_{\text{dig,pixel}} + 20$ to $\bar{E}_{\text{dig,pixel}} - 30$. The reason for the asymmetric ranges is to avoid an overemphasis of the charge sharing contribution towards lower energies (respective higher threshold values). The fit and the update of the range is repeated until the peak position is fixed and does not change any more ($\left|\bar{E}_{\text{dig,pixel}} - \bar{E}_{\text{dig,pixel,old}}\right| \leq 0.0001$). The resulting fit is, for instance, shown in figure 15.

Then the program moves on to the next pixel. After the fit could be applied to all pixels, the values of interest are saved in a file. These values are, for instance, the global energy $\bar{E}_{\text{photon}}$, the peak position $\bar{E}_{\text{dig,pixel}}$, its variance $s^2\left(\bar{E}_{\text{dig,pixel}}\right)$ and for calculating the energy resolution (equation (3.1)) the peak width σ_{pixel}.

This whole fitting procedure for a single calibration point and all 65 536 pixels takes less than 20 min on a single 3 GHz CPU core of a standard Intel processor.

The second step is the same as the one for the global energy calibration [1, section 2.1] with the slight change that it is performed for every pixel. By fitting the final calibration curve on at least three energies, the threshold calibration can be performed. As we want to take into account the variances $s^2\bar{E}_{\text{dig,pixel}}$ of each calibration point, the function $E_{\text{dig,pixel}} = f\left(E_{\text{photon}}\right)$ (equation (A.3)) — the inverse of the required function $E_{\text{photon}} = f\left(E_{\text{dig,pixel}}\right)$ — has to be fitted into the calibration values:

$$E_{\text{dig,pixel}} = a_{0,\text{pixel}} + a_{1,\text{pixel}} \cdot E_{\text{photon}}. \tag{A.3}$$

Therefore, we obtain in the fitting process for each pixel the variances $s^2\left(a_{0,\text{pixel}}\right)$, $s^2\left(a_{1,\text{pixel}}\right)$ and the covariance $\text{cov}\left(a_{0,\text{pixel}}, a_{1,\text{pixel}}\right)$. The energy calibration used, is derived by inverting equation (A.3):

$$\begin{aligned} E_{\text{photon}} &= \frac{-a_{0,\text{pixel}}}{a_{1,\text{pixel}}} + \frac{1}{a_{1,\text{pixel}}} \cdot E_{\text{dig,pixel}} \\ &= b_{0,\text{pixel}} + b_{1,\text{pixel}} \cdot E_{\text{dig,pixel}}. \end{aligned} \tag{A.4}$$

Again the overall energy uncertainty caused by the calibration uncertainties derives to

$$\begin{aligned} u^2\left(E, \text{pixel}\right) = s^2\left(b_{0,\text{pixel}}\right) &+ 2 \cdot \frac{E - b_{0,\text{pixel}}}{b_{1,\text{pixel}}} \cdot \text{cov}\left(b_{0,\text{pixel}}, b_{1,\text{pixel}}\right) \\ &+ \left(\frac{E - b_{0,\text{pixel}}}{b_{1,\text{pixel}}}\right)^2 \cdot s^2\left(b_{1,\text{pixel}}\right). \end{aligned} \tag{A.5}$$

[3] These ranges are empirical values gained from measurements.

2012 JINST 7 P07011

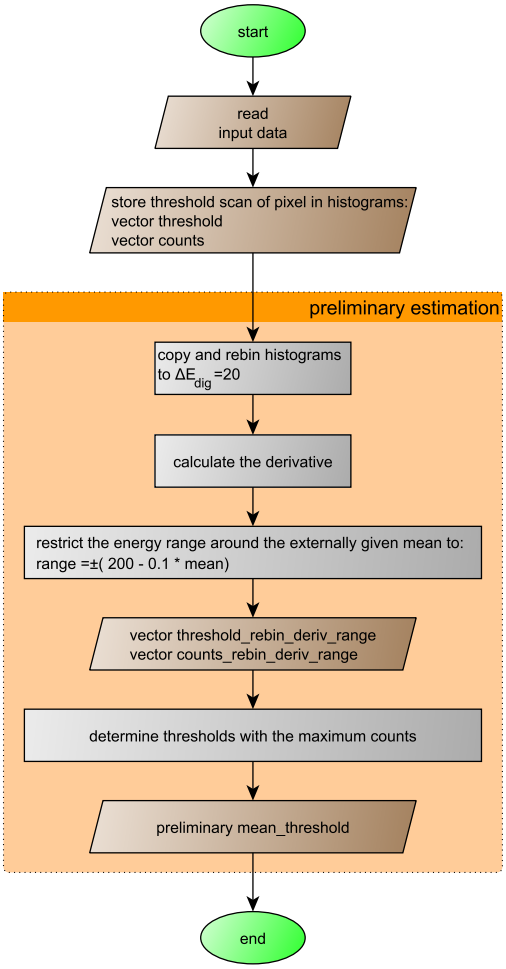

(a) For each pixel a preliminary estimation of the peak position $\bar{E}_{\mathrm{dig,pixel}}$ is performed. It uses the derivative of the threshold scan in a very rough binning $\Delta E_{\mathrm{dig}} = 20$ and at a predefined range.

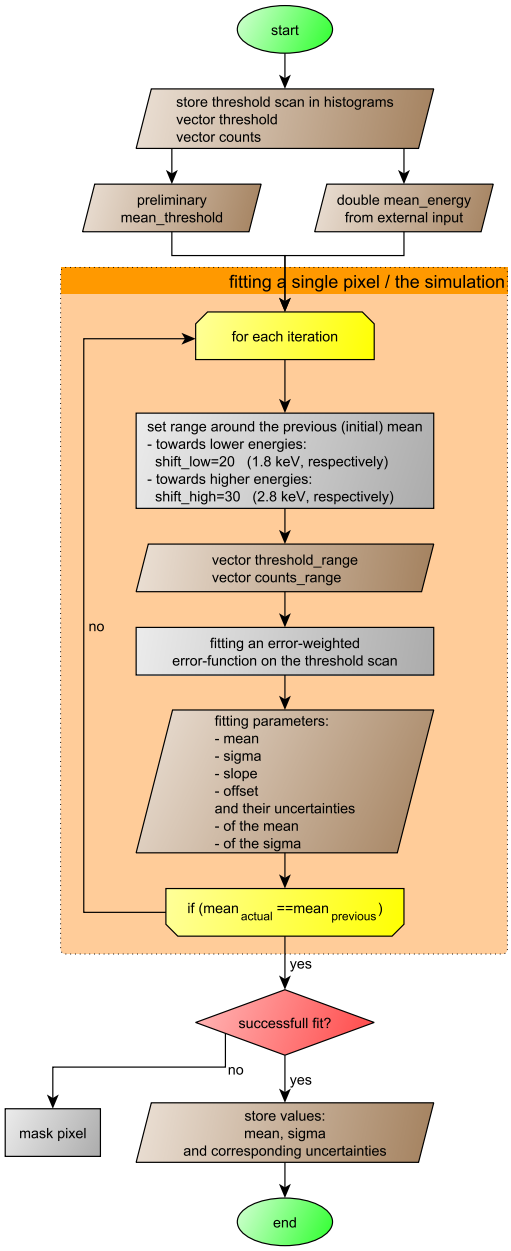

(b) After the preliminary estimation (left figure) a normal distribution function is fitted on the measured threshold scan.

Figure 14. Detailed flowcharts for the preliminary estimation (a) and the pixel-by-pixel fitting procedure (b).

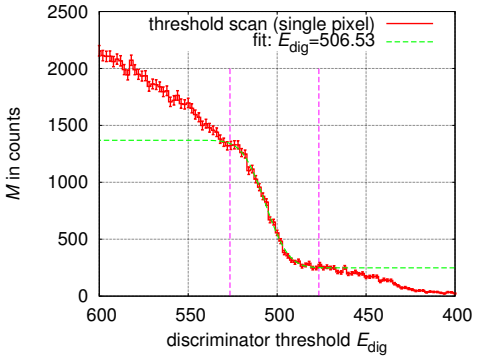

Figure 15. Threshold scan for a single pixel measured during irradiation by a Gd K_α fluorescence source (red line), a normal distribution function (equation A.2) fitted to its full energy peak with $\bar{E}_{\mathrm{dig}} = 506.53$ (green dashed line) and the final boundaries for the fitting range (magenta dashed line).

Acknowledgments

This work was carried out within the Medipix Collaboration.

References

[1] P. Sievers, T. Weber, T. Michel, J. Klammer, L. Büermann and G. Anton, *Bayesian deconvolution as a method for the spectroscopy of X-rays with highly pixelated photon counting detectors*, 2012 *JINST* **7** P03003.

[2] J. Giersch and J. Durst, *Monte Carlo simulations in X-ray imaging*, *Nucl. Instrum. Meth.* **A 591** (2008) 300.

[3] J. Klammer, J. Roth and O. Hupe, *Novel reference radiation fields for pulsed photon radiation installed at PTB*, *Radiat. Prot. Dosimetry* (2012) 1.

[4] X. Llopart, R. Ballabriga, M. Campbell, L. Tlustos and W. Wong, *Timepix, a 65k programmable pixel readout chip for arrival time, energy and/or photon counting measurements*, *Nucl. Instrum. Meth.* **A 581** (2007) 485.

[5] X. Llopart, M. Campbell, R. Dinapoli, D. San Segundo and E. Pernigotti, *Medipix2: A 64-k pixel readout chip with 55-μm square elements working in single photon counting mode*, *IEEE Trans. Nucl. Sci.* **49** (2002) 2279.

[6] ISO 4037-1: *X and gamma reference radiation for calibrating dosemeters and doserate meters and for determining their response as a function of photon energy – part 1: Radiation characteristics and production methods*, (1996).

[7] ICRU Report, *Conversion Coefficients for use in Radiological Protection against External Radiation. Volume* **57**, International Commission on Radiation Units and Measurements, (1994).

[8] P. Sievers, T. Schneider, T. Michel and G. Anton, *X-ray spectroscopy with photon counting imaging detectors such as Timepix*, in *2011 IEEE Nuclear Science Symposium Conference Record*, (2011) pg. 1826–1828.

3.2.2 Improved global energy calibration

In the preceding publication the global energy resolution is mentioned in figure 4 (page 49), but no mathematical derivation has been given on how it is calculated. This can be derived by an extended global energy calibration. The global energy calibration method mentioned in the first publication on page 26 has the disadvantage that pixels with a higher count rate are overemphasized compared to those with a lower one. Knowing this, the problem is to guarantee an overall homogeneous intensity of photon flux over the total pixel matrix. This can – in most cases – not be assured.
As soon as a pixel-by-pixel energy calibration has been performed one can derive a global energy calibration from the calculated fitting parameters of equations A.1 and A.2 on pages 54ff. The mean threshold

$$\bar{E}_{\mathrm{dig,global}} = \frac{1}{N} \sum_{\mathrm{pixel}=1}^{N} \bar{E}_{\mathrm{dig,pixel}}, \tag{3.1}$$

its fitting uncertainty

$$s\left(\bar{E}_{\mathrm{dig,global}}\right) = \frac{1}{N} \sum_{\mathrm{pixel}=1}^{N} s\left(\bar{E}_{\mathrm{dig,pixel}}\right), \tag{3.2}$$

and the corresponding photon energy $\bar{E}_{\mathrm{photon}}$ of each calibration energy are then used for the fitting of the calibration curve (equation 4.10 on page 26).

The global energy resolution as shown for comparison in figure 4 on page 49 has been calculated the following way:

$$\frac{\Delta E}{E} = \sqrt{b_{1,\mathrm{global}}^2 \,\mathrm{var}\left(\bar{E}_{\mathrm{dig,pixel}}\right) + \left(\frac{1}{N} \sum_{\mathrm{pixel}=1}^{N} b_{1,\mathrm{pixel}} \sigma_{\mathrm{pixel}}\right)^2} \cdot \frac{2\sqrt{2\ln 2}}{\bar{E}_{\mathrm{photon}}}, \tag{3.3}$$

with $\mathrm{var}\left(\bar{E}_{\mathrm{dig,pixel}}\right) = \frac{1}{N-1} \sum_{\mathrm{pixel}=1}^{N} \left(\bar{E}_{\mathrm{dig,pixel}} - \bar{E}_{\mathrm{dig,global}}\right)^2$ and b_1 the slope of the final calibration curve.

With this energy calibration method the spread of intensity of the radiation field used for calibration no longer has an impact on the derived calibration values itself – only on the uncertainties of the fit parameters.

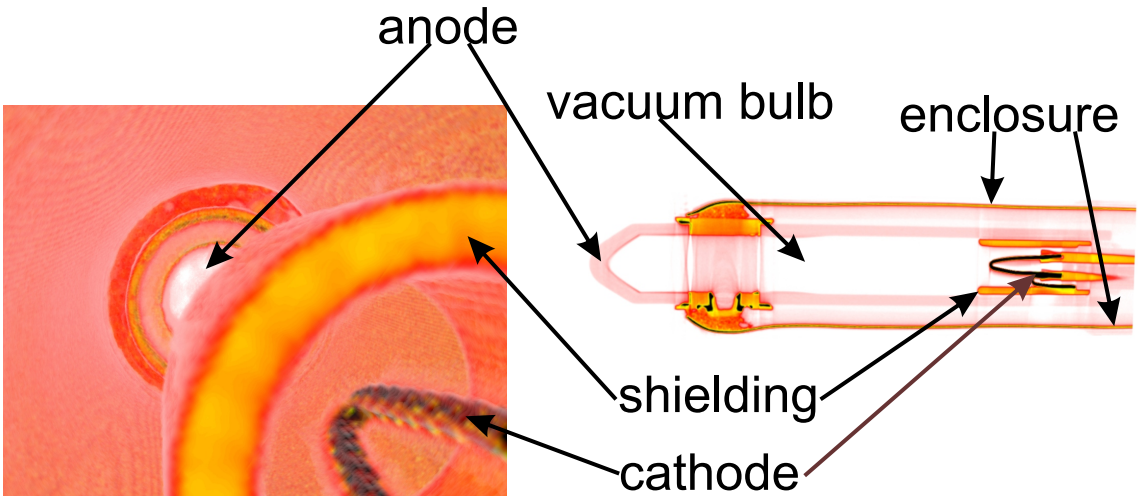

(a) 3D rendered view from cathode towards anode.

(b) View of the XZ-plane.

Figure 3.1 Image of the type of X-ray tube being used for spectrometry taken with a µCT. This image was taken by Frank Nachtrab (Fraunhofer Development Center X-Ray Technology EZRT, Fürth).

3.2.3 Further impacts of a pixel-by-pixel energy calibration

Some further implications of the pixel-by-pixel energy calibration will be shown with the example of a therapeutic X-ray source used for brachytherapy[1] [SA+10]. A µCT image of this particular X-ray tube is shown in figure 3.1. For an impression of the very small dimension, the whole diameter – enclosure to enclosure – of this X-ray tube is only about 2.8 mm. The parameters for setup, source and detector are summarized in table 3.1.

Relative uncertainties of the measurement

All analyses shown in the following figures (3.2-3.4 and 3.6a) have been performed on the basis of one single measurement. In figure 3.2 the relative uncertainties analyzed for different sizes of ROI are shown – analogue to the ones shown in figure 10 on page 29, but now for a pixel-by-pixel calibrated detector. It is shown that for the smallest ROI the most significant contribution to the total uncertainty $u_{\text{total}}\left(M_{i,\text{ROI}}\right)$ is the statistical uncertainty $s\left(M_{i,\text{ROI}}\right)$. By increasing

[1] Axxent®HDR X-ray source from the vendor Xoft [Xof; LP+08]

parameter	value
anode material	yttrium (Y)
tube voltage	50 kV
anode current	100 µA
distance detector-source	1 m
bias voltage of sensor U_{bias}	150 V
total measuring time	20 min
measuring time per THL	3 s

Table 3.1 Settings and parameters for both X-ray tube and Timepix detector.

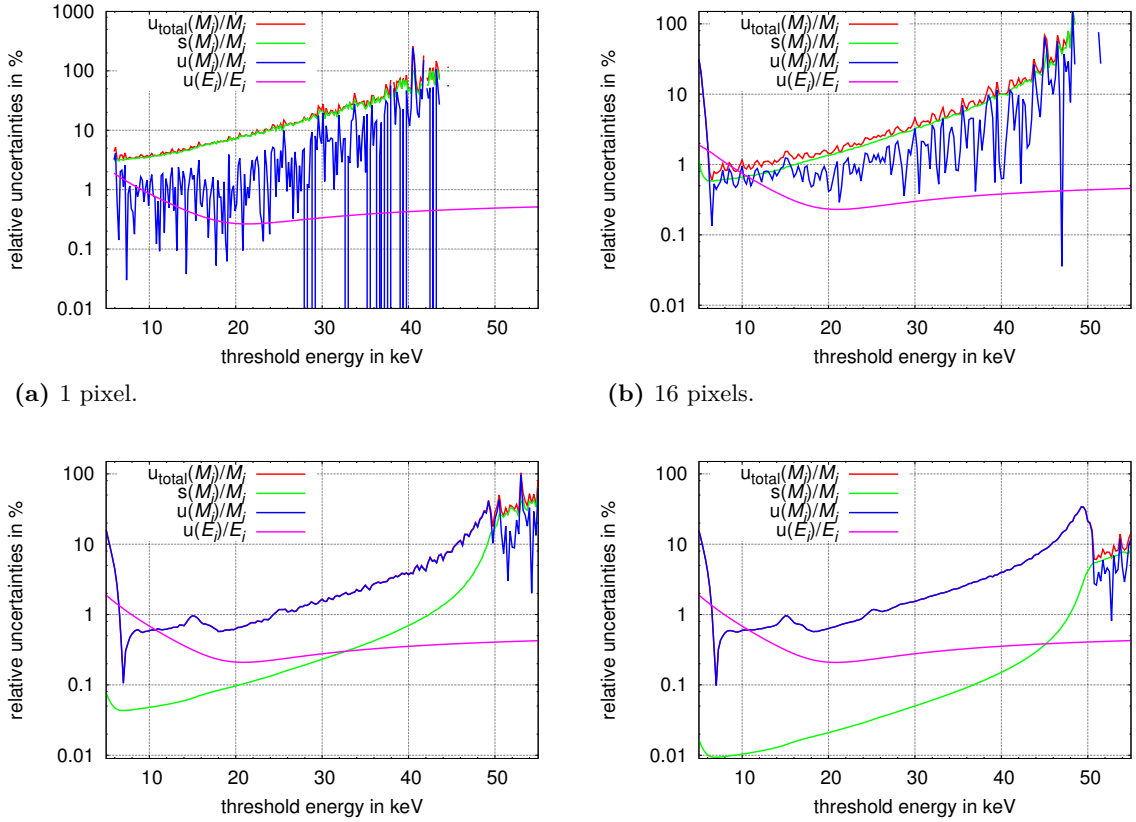

(a) 1 pixel.

(b) 16 pixels.

(c) 3 072 pixels (12 rows).

(d) 65 536 pixels.

Figure 3.2 Relative uncertainties of a THL scan derived by applying a pixel-by pixel energy calibration for different sizes of the analyzed ROI: one single pixel (a), 4 x 4 pixels (b), 12 x 256 pixels (c) and the total pixel matrix (d).

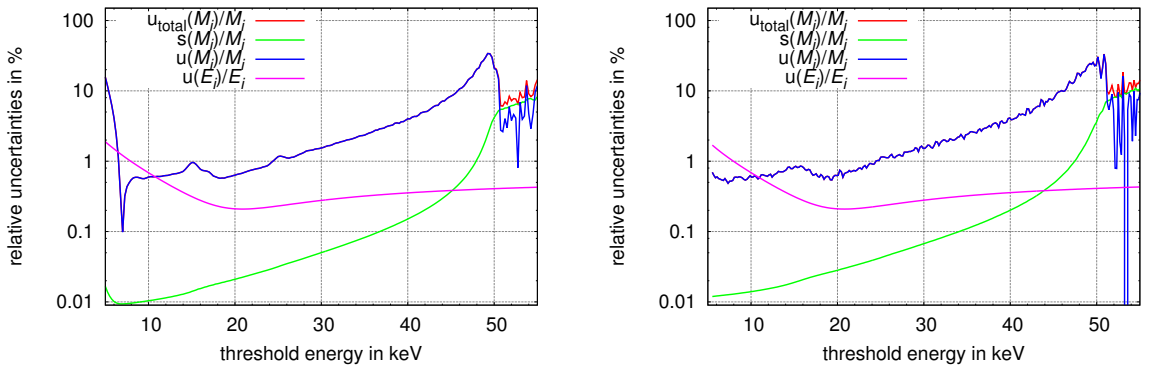

(a) pixel-by-pixel calibrated

(b) globally calibrated

Figure 3.3 Relative uncertainties of the same THL scan derived by applying both a pixel-by-pixel energy calibration (a) and a global energy calibration (b).

the size of the analyzed ROI, the relative statistical uncertainty decreases and the systematic uncertainty $u\left(M_{i,\mathrm{ROI}}\right)$ becomes the most prominent one. The statistical uncertainty in this case is the only one that is dependent on the size of the ROI. All other (systematic) uncertainties are almost constant. The oscillations visible in the systematic uncertainty $u\left(M_{i,\mathrm{ROI}}\right)$ for the very small ROI are due to the method of calculation (equation 2.3 on page 47) as it creates a correlation between the neighbouring channels and thus is not independent of statistical fluctuations. As the total uncertainty for analyzing the total pixel matrix is dominated by the systematic uncertainty, there is no difference between a pixel-by-pixel calibrated (figure 3.3a) or a globally calibrated (figure 3.3b) detector visible in the analyzed uncertainties.

Energy resolution

Although theoretically an improvement in energy resolution in the measured data of about 25 % (figure 4b on page 49) at an energy $E = 15.9\,\mathrm{keV}$ is possible by applying a pixel-by-pixel energy calibration compared to a global one, there is only an improvement of about 10 % seen in the deconvolved spectrum (figure 3.4). This is due to the fact that the abort condition for the Bayesian deconvolution is still dominated by the systematic uncertainty derived by the energy calibration (figure 3.3). The absolute values for the energy resolution are summarized later on in table 3.2.

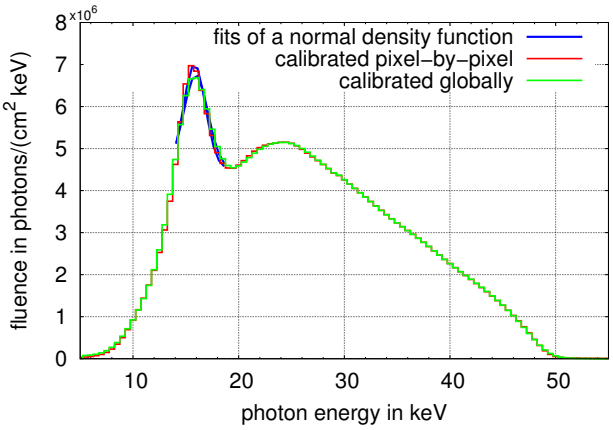

Figure 3.4 Emission spectrum – derived by deconvolution of the measured THL scan – of Axxent HDR X-ray source shown in figure 3.1, for both global and pixel-by-pixel energy calibration.

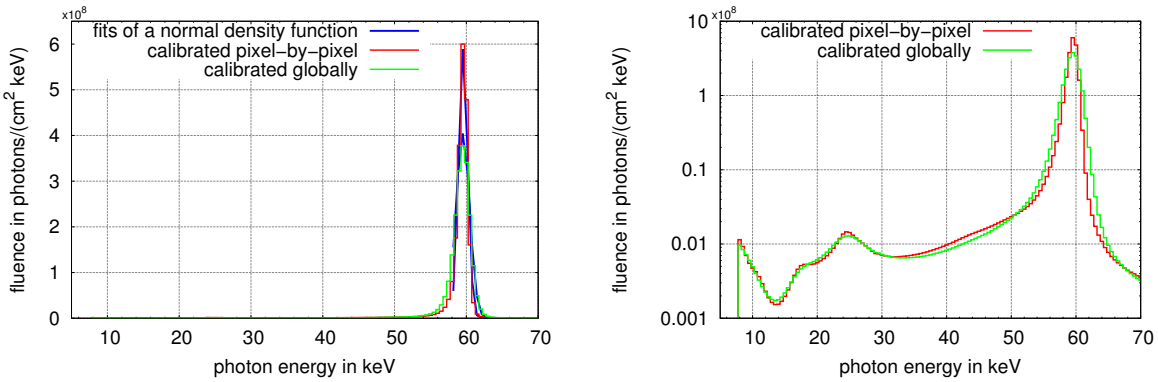

(a) linear scale.

(b) logarithmic scale.

Figure 3.5 Emission spectrum – derived by deconvolution of the measured THL scan – of the radioactive isotope ^{241}Am, for both global and pixel-by-pixel energy calibration.

The influence of the deconvolution on the energy resolution has also been tested for a slightly higher energy at $E = 59.6\,\text{keV}$. In this case the detector has been irradiated with photons from an ^{241}Am radioactive source. In the deconvolved spectrum (figure 3.5a) an improvement in energy resolution is already visible, comparing both calibration methods. The absolute values are summarized later on in table 3.2. For the spectrum derived after pixel-by-pixel calibration, further emission lines appear (figure 3.5b) at 26.3 keV and Np $- L_\beta$ fluorescence line at 17.5 keV.

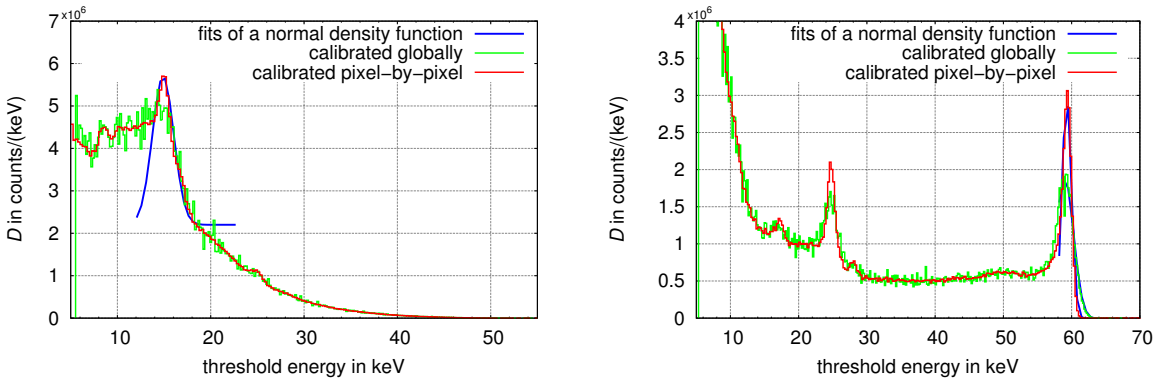

(a) Axxent HDR X-ray source.

(b) Radioactive source ^{241}Am.

Figure 3.6 Distribution of deposited energies D – derivative of the THL scan – for both radiation sources, Axxent HDR X-ray source (a) and ^{241}Am isotope (b), and for both calibration modes.

The calculated resolution values derived by fitting a normal density function at the peaks in the deconvolved spectrum are now compared to those derived by the derivatives of the THL scans. The derivatives of both measurements are shown for both calibration modes in figure 3.6. The results of the fits are summarized in table 3.2. As a conclusion, two remarkable things are pointed out:

	FWHM		improvement
	global	pixel-by pixel	
Yttrium K_α fluorescence at $E = 15.9\,\text{keV}$:			
derivative of THL scan	—	2.71 keV	—
deconvolved spectrum	2.69 keV	2.41 keV	10 %
^{241}Am radioactive source at $E = 59.6\,\text{keV}$:			
derivative of THL scan	3.06 keV	1.63 keV	47 %
deconvolved spectrum	2.24 keV	1.49 keV	33 %

Table 3.2 Energy resolution derived by fitting a normal density function on the peaks of either the deconvolved spectrum or on the derivative of the THL scan (figures 3.4, 3.5a and 3.6).

Firstly, the improvement in energy resolution between the two calibration methods as seen for the energy deposition spectrum could only be transported partly into the deconvolved spectrum. This is due to the fact that the abort condition for the Bayesian deconvolution is still biased by the systematic uncertainty de-

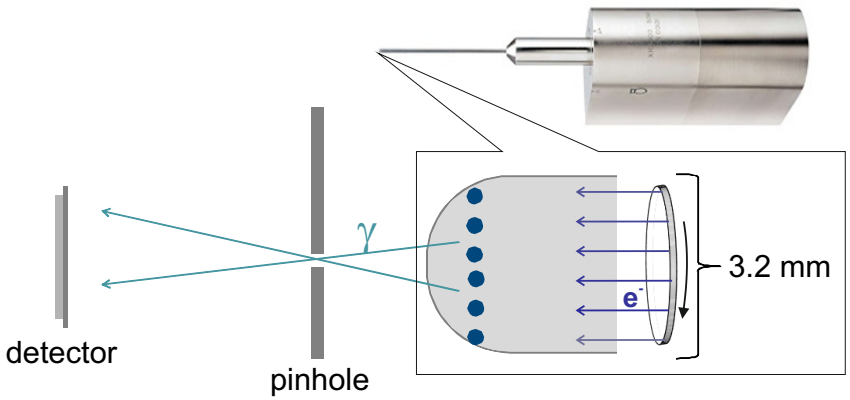

Figure 3.7 Schematics of the setup for measuring the focal spots of the Intrabeam X-ray source (not to scale). At the very left, the Timepix detector; in the centre, the pinhole with a thickness of 1 mm and a diameter of 50 µm; inside the enlarged image on the right, a zoomed-in view of the tip of the acceleration tube is shown. Inside this tube an electron beam is moving. The blue circles represent the focal spots, where the beam hits the gold anode.

rived by the energy calibration.
Secondly and more importantly, the energy resolution of the deconvolved spectrum is in the same order as for the energy deposition spectrum. This demonstrates that both the exit condition for the iterative process is set correctly and the calculated uncertainties are in the right magnitude.

3.2.4 Spectrometric imaging

The measurements of the anode heel effect presented in section 3.2.1 have shown promising results by facilitating ROIs of the size 12 x 256 pixels. Going one step further to even smaller ROIs, it is possible to do real position-resolved spectrometric measurements [SSMA11]. As an application I measured the focal spots of the Intrabeam X-ray source from the vendor Carl Zeiss [Zei] with a pinhole camera. In figure 3.7 and table 3.3, the schematics and parameters of the measurement setup are shown. The images of the focal spots (figures 3.8) were taken using the camera obscura principle. Sixteen spots aligned in a circle became visible (figure 3.8a). This result was confirmed by the vendor. Inside the cylinder of this tube there is a moving electron beam focusing at certain points – the sixteen focal spots. In this image (figure 3.8a) of the focal spots, a lower intensity in the spots at the bottom than at the top has been observed. This was a hint for a misalignment of the circle of focal spots. In a second measurement, the

parameter	value
anode material	gold (Au)
tube voltage	50 kV
anode current	40 µA
diameter of pinhole	50 µm
distances:	
detector-pinhole	200 mm
pinhole-tube	100 mm
magnification	2.00
total measuring time	4 h 28 min
measuring time per THL	60 s
bias voltage of sensor U_{bias}	150 V

Table 3.3 Settings and parameters for both the Intrabeam X-ray source and the Timepix detector.

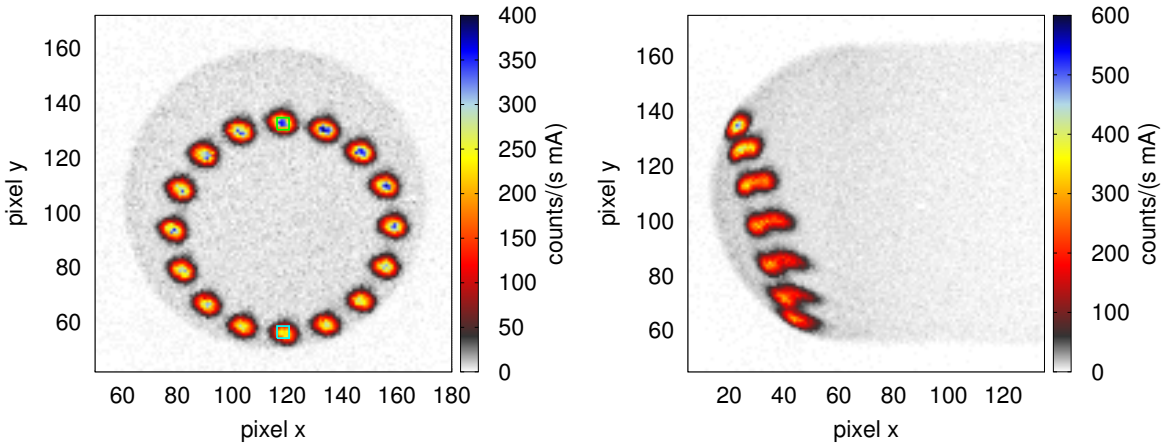

(a) Frontal view.

(b) Side view.

Figure 3.8 Images of the focal spots of the Intrabeam X-ray source in a frontal view (a) and a side view (b). In the frontal view the two rectangles (only barely visible) at the top and bottom spot mark the further investigated ROIs.

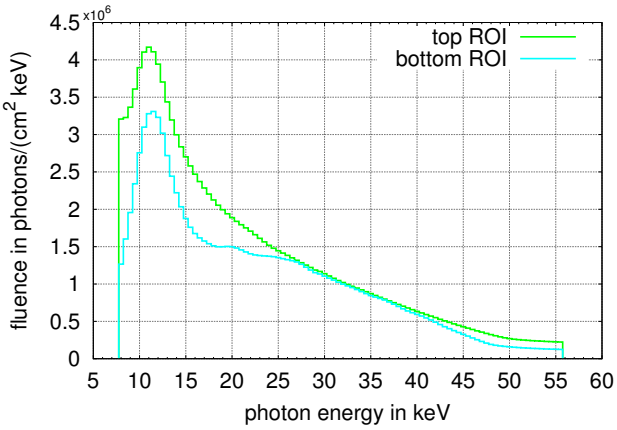

Figure 3.9 Emission spectra – derived by deconvolution of the measured THL scan – of the Intrabeam X-ray source, for both ROIs indicated in figure 3.8a.

X-ray tube was rotated by 90° and the misalignment became visible (figure 3.8b). The higher intensity visible in the side view is due to the fact that two or more focal spots are lying behind each other and their intensities are partly added. For the spectrometric analysis two ROIs have been set, one at the very top spot and one at the very bottom – indicated in figure 3.8a. For those two chosen focal spots the emission spectra (figure 3.9) have been calculated by the deconvolution of the corresponding THL scans. The difference in intensity (figure 3.8a) is in good agreement with the difference between the deconvolved spectra of the two indicated ROIs. The active instrumented area of each ROI is $4.8 \times 10^{-4}\,\mathrm{cm}^2$. This is only a tiny fraction compared to the mentioned hpGe detectors with an active area of $4.9\,\mathrm{cm}^2$. The demonstrated simultaneous measurement of spectra in multiple ROIs is an important innovation as compared to the established spectrometry systems (e.g. hpGe detectors).

3.3 Time-resolved spectrometry

The aim of the preceding sections was to extend the analysis to gain position resolution of the deconvolved spectra. The aim of the work in this section is to verify that there is no change over time in the emission spectrum of a newly installed X-ray source at PTB [KRH12]. On the one hand, I have shown that I developed a very competitive analysis procedure by facilitating the Bayesian deconvolution and the pixel-by-pixel energy calibration. On the other hand, our recent measurements have shown, that it is possible to measure – with a

Timepix detector operated in Time of Arrival (ToA) mode – the time shape of very short X-ray pulses (< 200 ns) [BS+09] with a sampling of 10 ns. For gaining both timing and spectral information, both methods were combined to receive time-resolved spectra. The results for both a conventional X-ray tube and for the new development are shown in the following.

Publication: Time-resolved spectrometry

In this publication I give an introduction to the difficulty of being able to perform type tests within pulsed radiation fields. I performed the needed measurements for verification of the stability of the emission spectrum of a newly developed tube over time. In contrast to formerly shown measurements I did not receive a THL scan directly but for each set THL I got the change in intensity over time. By rearranging all measured data points I was able to receive time-resolved THL scans. These have then been deconvolved into time-dependent spectra with Bayesian deconvolution. The measurements and analyses are shown for both a conventional X-ray tube and a newly installed X-ray source operated in "grid-pulsing" mode. For the conventional one I was able to validate my setup and the method as the results looked as expected. For this new X-ray source, I was then able to validate that the variation in the spectra emitted during the rise time of an X-ray pulse is on a very low time scale and negligible.
The manuscript is accepted for publication in the Journal of Instrumentation by IOP Publishing (`http://iopscience.iop.org/1748-0221/`) as:
Peter Sievers et al. 'Time-resolved spectrometry for the characterization of a reference field for pulsed radiation'. In: *Journal of Instrumentation* (Manuscript accepted for publication);

Contributions of the co-authors:

- running a facility at PTB with the new X-ray reference equipment operated in "grid-pulsing" mode
- performing measurements with a diode for proving the stability of the radiation pulses in grid-pulsing mode
- discussion of results and their implications.

My own contributions:

- combining the two detector methods – measuring in ToA mode and in parallel performing a threshold scan
- performing the measurements with the Timepix detector at PTB and in the lab at ECAP
- developing and performing the analysis.

RECEIVED: *August 23, 2012*
REVISED: *September 7, 2012*
ACCEPTED: *September 17, 2012*
PUBLISHED: *in preparation*

Time-resolved spectrometry for the characterization of a reference field for pulsed radiation

Peter Sievers[a,b*], **Jana Klammer**[a], **Oliver Hupe**[a], **Thilo Michel**[b] **and Gisela Anton**[b]

[a] *Physikalisch-Technische Bundesanstalt (PTB), Bundesallee 100, D-38116 Braunschweig, Germany*
[b] *Radiation and Detector Physics, Erlangen Centre for Astroparticle Physics (ECAP), University of Erlangen-Nürnberg, Erwin-Rommel-Str. 1, D-91058 Erlangen, Germany*

E-mail: peter.sievers@ptb.de

ABSTRACT: The investigation of the spectral change during a radiation pulse is of high interest. The aim of the work presented is to prove that the emitted X-ray spectrum of a novel X-ray tube [1], developed at PTB as a reference field for pulsed photon radiation, has no time dependency of the spectral distribution during the pulse. Nowadays X-ray tubes are pulsed by switching on and off the HV generator. Therefore, they have a rising edge of about 600 µs until the pre-set acceleration voltage (e.g. 60 kV) is reached. In contrast, the newly developed X-ray tube reduces the rise and fall time by up to a factor of 10 or 60, respectively. This was achieved by designing the X-ray tube as a triode. The X-ray emission of this tube can be switched on and off by switching only the quite low voltage of the additional grid while the high voltage remains constantly on.
For the measurements we used a Timepix detector [2] operated in Time of Arrival (ToA) mode. Additionally, the adjustable analogue threshold was swept through. With such a measurement over multiple X-ray pulses we obtained information about the timing and the energy distribution of the emitted photons during the rise time of the HV generator.
The real impinging spectrum was gained by the deconvolution of the time-resolved measured threshold scan. Such a deconvolution is necessary due to the blurring of the energy information in the pixelated sensor by effects like charge sharing or Compton scattering. For the deconvolution the Bayesian approach [3] was chosen as it turned out to be very stable even for low statistics in the measurements.
For the novel X-ray tube it is now possible to confirm that the full acceleration voltage is reached quite instantaneously and therefore no spectral change can be observed.

*Corresponding author

Contents

1. Introduction **1**
1.1 Pulsed radiation 2
1.2 Timepix detector 2

2. Applied Methods **3**
2.1 Mode of detector operation 3
2.2 Deconvolution 4

3. Time-resolved spectrometry **4**
3.1 Measurement setup 4
3.2 Measured data 5
3.3 Deconvolved spectra 6

4. Conclusion **7**

1. Introduction

Spectrometry of X-ray radiation is a widely used application, for instance, in the determination of X-ray tube spectra, synchrotron light spectra, radioactive material composition, and in astronomy. The conventional way of measuring the spectrum with semiconductor devices (e.g. a high purity germanium detector) is to detect the charge carriers released by the impinging photon. As the amount of charge corresponds to the deposited photon energy, it is necessary to collect at least the complete charge of one charge carrier type. Furthermore, in the absence of an absorption edge the absorption probability decreases with increasing photon energy. To cope with the requirement of high detection efficiency and energy determination one has to use relatively large and thick semiconductors. This ensures that every photon is fully absorbed and that any released charge remains within the sensor. As those detectors suffer of a very low rate capability, they cannot be used for measuring the spectral change in time of an X-ray pulse. Pixelated detectors with an application-specific integrated circuit (ASIC) capable of delivering timing and energy information simultaneously are more appropriate for this task as the photon flux is spread over many relatively small pixel areas. Due to the effects correlated to the pixelation of the sensor (e.g. Charge sharing, Compton scattering, etc.) the measured distribution of deposited energy is blurred and distorted.
If the detector setup and the interaction processes in the detector are implemented correctly in a Monte Carlo simulation, the energy response functions can be modelled. Those detector responses have been calculated with the simulation framework ROSI [4, 5], utilizing EGS4 and including all relevant physical processes in the sensor layer. The impinging spectrum can then be computed by the deconvolution of the measured data [3].
The aim of this work is to present a method for time-resolved spectrometry. As an application of this method we will show the spectrometry of X-ray pulses generated conventionally by generator pulsing and in contrast with our novel X-ray equipment in grid pulsing mode.

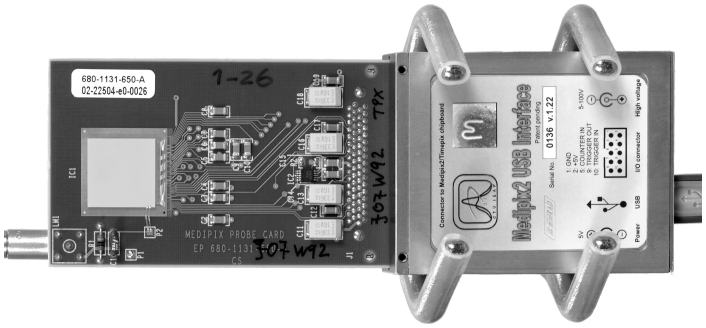

Figure 1. Photograph of the Timepix detector, which is mounted on the PCB, and the USB readout [8]. On the very left the plug for the bias voltage can be seen. Next to it the grey rectangular area is the sensor of the Timepix detector. On the right-hand side of the image the USB readout is shown.

1.1 Pulsed radiation

Pulsed photon radiation is widely used in medical investigations or at customs and airports. In these fields pulsed radiation is applied for high image quality even when the object is in motion. The great advantage of pulsed radiation compared to continuous radiation, which is used for calibrations, is the fact that one short radiation pulse with a rather high dose rate per pulse might be sufficient for an image of high quality with nearly no in-motion unsharpness. There are two general ways of generating a radiation pulse with X-ray equipment – a generator-controlled mode and a grid-controlled mode. In most applications the less expensive generator-controlled mode is used. Generator control means that the high voltage generator of the X-ray equipment is switched on and off to generate a radiation pulse. In terms of grid control the voltage is applied constantly to the tube while a small voltage on a grid inside the X-ray tube is switched to permit the electron flow from the cathode to the anode – the working principle known as a triode.
Depending on the mode of generation the pulse rising and falling times may differ significantly due to the capacities of the electric connections and their time-consuming discharges. The longer rising and falling times at generator pulsing may lead to a shift in the mean energy E_{mean} during the pulse, and to a time dependency of the emitted spectrum, respectively. Therefor, the mean energy E_{mean} strongly depends on the pulse duration and more precisely on the ratio of pulse-peak duration and the rising and falling times. For defined investigations, such as type testing of dosemeters according to [6, 7], only one parameter is permitted to be changed, for instance, the pulse duration, but not the mean energy E_{mean} of the pulse.
The novel X-ray equipment for pulsed photon radiation at PTB [1] works in a grid-controlled mode but can also be switched to a generator-controlled mode as well. This condition allows the investigation of the two common generation modes for radiation pulses.

1.2 Timepix detector

For the measurements of the emitted X-ray spectrum a Timepix detector [2] (figure 1) was used. It consists of an ASIC which has 256 x 256 pixel cells with a 55 µm pixel pitch. As the sensor material, a silicon layer with a thickness of 300 µm was bump-bonded to the ASIC. Each pixel cell of the ASIC consists of an analogue and a digital electronics part. In the analogue part of each

pixel it is possible to set a global energy threshold E_{dig}. This energy threshold value is transferred via a digital analog converter (DAC) into a reference voltage. If the voltage pulse caused by the amplified signal of the collected charge is higher compared to this reference voltage, the counter in the digital part of the corresponding pixel is incremented [2, section 2.1]. By increasing this energy threshold E_{dig} gradually, the distribution D of X-ray photons with respect to their deposited energy in the sensor will be scanned:

$$M\left(E_{\mathrm{dig}}\right) = \int_{E_{\mathrm{dig}}}^{\infty} D\left(E\right) dE. \tag{1.1}$$

This procedure is described in detail in [3].

2. Applied Methods

2.1 Mode of detector operation

In this work the detector was operated in the time of arrival (ToA) mode. Hereby, the time interval starting with the preamplifier pulse exceeding the threshold and ending by a given stop signal is measured by counting the number of clock cycles (figure 2). This gives timing information relative to the end of the frame. In the case of this work the stop signal is given by an external trigger from the X-ray generator. Within this mode it is possible to measure the time course of very short $\approx 200\,\mathrm{ns}$ X-ray pulses at a clock frequency of 100 MHz [9]. In the work presented here we were interested in having look at the rising edge of relatively long pulses of 1 ms to 10 ms. Thus, the clock was operated at 10 MHz which gives a maximal time frame of 1.18 ms as the counter inside the pixel is limited to a maximum value of 11 810. As a second impinging photon would be ignored within this method, it is necessary to reduce the radiation flux to an appropriate extend which can be monitored beforehand in the standard counting mode of the detector.
In order to obtain energy and time information of a radiation pulse, the time course has been measured in this ToA mode at multiple energy thresholds. As a consequence of this method, one has to use multiple pulses – at least as many pulses as thresholds. To achieve higher statistics even more radiation pulses are necessary. Thus, the reproducibility of each X-ray pulse is a requirement for the applicability of this method, as the mean spectrum per time frame is measured. This has to be verified by a continuous monitoring of the trigger signal.
The energy dependent threshold scans have been determined in the following way. For each time

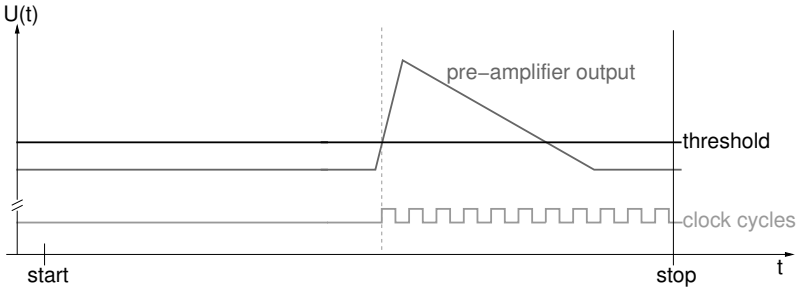

Figure 2. Scheme of the ToA mode of the Timepix detector for gaining information about the time course of a radiation pulse by measuring the duration from the pre-amplifier's rising edge until the end of the frame, given by a (external) trigger signal.

frame t of interest an empty histogram for the threshold scan $\vec{M}_t$ was assigned. If the measured time value of a pixel is in between the time frame t the counter inside the corresponding $M_{i,t}$ is incremented by one. The corresponding energy channel i for a given energy threshold was determined by applying a pixel-by-pixel energy calibration [10]. Thus the total pixel matrix was used globally for this kind analysis.

2.2 Deconvolution

For the deconvolution of the measured distribution a Bayesian approach was chosen, as it turned out to be stable and reliable [3, 10]. The iterative formula used is:

$$T_i^{n+1} = \frac{1}{\tau_i} T_i^n \sum_k \frac{R_{ki} \cdot M_k}{\sum_j R_{kj} \cdot T_j^n}, \tag{2.1}$$

with the iteration index n, the mean number of triggered pixels per incident photons $\tau_i = \sum_k R_{ki}$ and i, k, j denote the energy channel index of either the measurement $\vec{M}$ (the threshold scan) or the impinging spectrum $\vec{T}$. The matrix $\hat{R}$ describes the simulated detector responses to monoenergetic irradiation.
The exit condition for this iterative process is defined in the following. For each iteration step, the "virtual measurement" $\vec{M}_\mathrm{v}$ is computed by the convolution of the detector response functions $\hat{R}$ with the deconvolved spectrum $\vec{T}^{n+1}$ of the actual iteration step:

$$\vec{M}_\mathrm{v} = \hat{R} \cdot \vec{T}^{n+1}. \tag{2.2}$$

If the condition

$$\chi^2 = \frac{\sum_{i=1}^{N} \left(\frac{M_{\mathrm{v},i} - M_i}{u_\mathrm{total}(M_i)} \right)^2}{N} \leq 1 \tag{2.3}$$

is reached, the iteration process is stopped and the actual $\vec{T}^{(n+1)}$ is regarded as the true impinging spectrum T.

3. Time-resolved spectrometry

3.1 Measurement setup

The above mentioned need of reproducibility was assured by a reference measurement with an oscilloscope of either a diode signal for the grid pulsing or directly of the generator voltage for the generator pulsing. The actual applied parameters for both the generator pulsing and the grid pulsing are indicated in table 1. The settings for the previously performed measurements in grid pulsing mode could not be adopted for the measurements in generator pulsing mode as they turned out to be unstable in terms of the reproducibility of the X-ray pulses. In both cases the Transistor-transistor logic (TTL) signal provided by the X-ray generator was facilitated. For the measurement of the generator pulsing a delay was necessary and realized with a Nuclear Instrumentation Module (NIM) electronic device. Those signals are then used to trigger the "stop" signal of the detector readout (working scheme in figure 2).

	generator pulsing	grid pulsing
tube type	Siemens Megalix	Siemens Megalix
	Cat-125/15/40/80	Cat-125/35/80
	(conventional)	(extra grid)
high voltage	60 kV	40 kV
filtration	intrinsic	intrinsic
current	2 mA	10 mA
pulse verification	generator voltage	diode signal
pulse duration	100 ms	1 ms
repetition frequency	1.5 Hz	2 Hz
number of pulses	45 000	1 000
per threshold	150	25
detector distance	384 cm	325 cm
total measuring time	8.3 h	8.3 min
threshold step ΔE_{dig}	$2 \mathrel{\widehat{=}} 0.19$ keV	$10 \mathrel{\widehat{=}} 1.25$ keV

Table 1. Settings of either the X-ray tubes and Timepix detector.

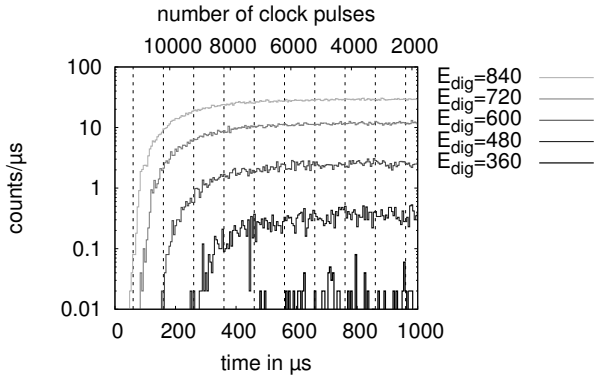

Figure 3. Mean time course of an X-ray pulse (averaged over multiple pulses) for generator pulsing measured at different thresholds (for visibility reasons only an extract of the measured thresholds is shown).

3.2 Measured data

For each threshold used the mean time course of X-ray pulses was measured. In the case of generator pulsing only the rising edge could be measured because of the limitations in the detector counter. Such a time course for an excerpt of the measured thresholds is shown in figure 3. In the graph of figure 3 it is clearly visible that the higher the global threshold energy (the lower the threshold value of E_{dig}), the later the photons arrive at the detector. The visible delay is up to 500 µs. This agrees to the time course of the measured voltage signal of the generator.

In the case of the grid pulsing of the newly developed radiation source, the intensity over time is shown in figure 4a. For comparison with the measured data of the generator pulsing, we had a closer look at the rising edge of the radiation pulse (figure 4b). The rise time of the radiation pulse

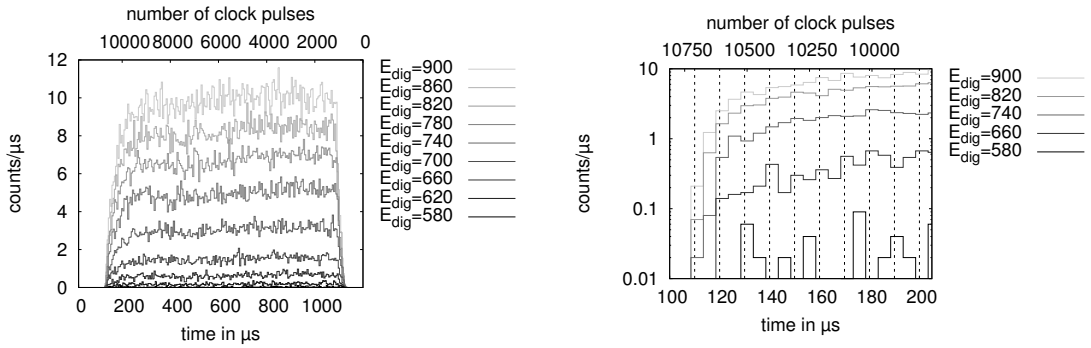

(a) Total pulse.

(b) Zoom into the rising edge.

Figure 4. Mean time course of an X-ray pulse (averaged over multiple pulses) for grid pulsing measured at different thresholds (for visibility reasons only an extract of the measured thresholds is shown).

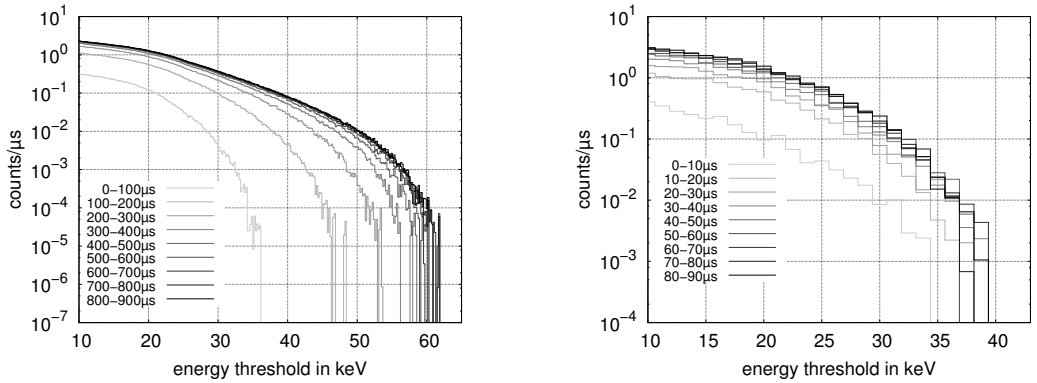

(a) Generator pulsing.

(b) Grid pulsing.

Figure 5. Time-dependent threshold scans analyzed for different time intervals relative to the beginning of the X-ray pulse for both the generator pulsing (a) and for the grid pulsing (b).

decreases for the grid pulsing to about 55 µs. An energy dependence as we have seen it in the case of the generator pulsing (figure 3) is only barely visible.

3.3 Deconvolved spectra

For a further analysis the measured data inside the areas indicated with dashed vertical lines of figures 3 and 4b have been rearranged to obtain time-dependent threshold scans. As the statistics in the measured data is low, a pixel-by-pixel energy calibration introduced in [10] was applied. The resulting threshold scans are shown in figure 5a for the generator pulsing, and for the grid pulsing in figure 5b. Those threshold scans have been deconvolved by applying Bayesian deconvolution [3]. For the generator pulsing this works out very well as shown in figure 6a. In contrast, the deconvolution for the grid pulsing (figure 6b) is not always performing that well as the statistic in the measured data is too low and pushes the method to its limit. This is also due to the higher chosen timing resolution of 10 µs.

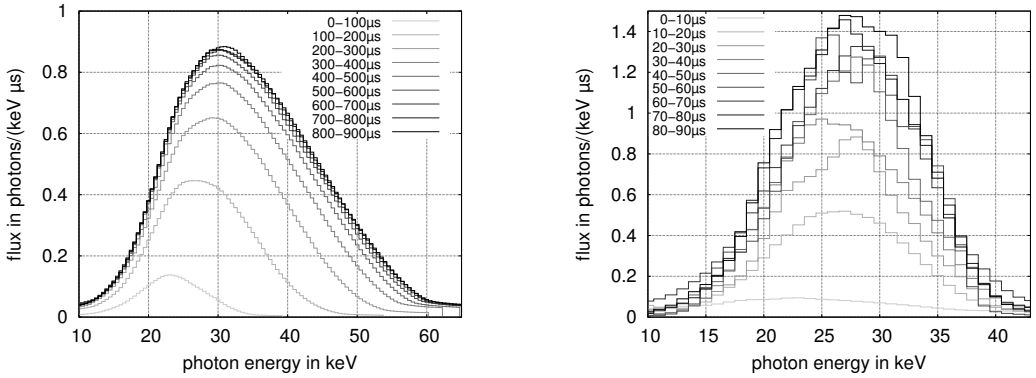

(a) Generator pulsing.

(b) Grid pulsing.

Figure 6. Deconvolved spectra of the time-dependent threshold scans analyzed for different time intervals relative to the beginning of the X-ray pulse for both the generator pulsing (a) and for the grid pulsing (b).

4. Conclusion

We have shown that it is possible to measure the energy-dependent time course of the intensity of an X-ray pulse as well as the time-dependent spectra. This could be achieved with a very precise energy calibration [10] of the Timepix detector. We have shown – for a conventional X-ray tube in generator pulsing mode – that the method and the detector are capable of delivering reasonable results. This method was then successfully used for the novel grid-pulsed X-ray tube at PTB [1]. We can confirm that the spectral change is on a very low timescale and only barely measurable (figure 5b). This gives the possibility of adjusting the pulse duration and the energy independently of each other. It enables defined investigations, such as type testing, as only one parameter is permitted to be changed, e.g. the pulse duration, but not the mean energy E_{mean} of the pulse.

Acknowledgments

This work was carried out within the Medipix Collaboration.

References

[1] J. Klammer, J. Roth, and O. Hupe, *NOVEL REFERENCE RADIATION FIELDS FOR PULSED PHOTON RADIATION INSTALLED AT PTB*, *Radiation Protection Dosimetry* (Apr., 2012) 1–5.

[2] X. Llopart, R. Ballabriga, M. Campbell, L. Tlustos, and W. S.-W. Wong, *Timepix, a 65k programmable pixel readout chip for arrival time, energy and/or photon counting measurements*, *Nuclear Instruments and Methods in Physics Research Section A: Accelerators, Spectrometers, Detectors and Associated Equipment* **581** (Oct., 2007) 485–494.

[3] P. Sievers, T. Weber, T. Michel, J. Klammer, L. Büermann, and G. Anton, *Bayesian deconvolution as a method for the spectroscopy of X-rays with highly pixelated photon counting detectors*, *Journal of Instrumentation* **7** (Mar., 2012) 20.

[4] J. Giersch, A. Weidemann, and G. Anton, *ROSI – an object-oriented and parallel-computing Monte Carlo simulation for X-ray imaging*, *Nuclear Instruments and Methods in Physics Research Section A: Accelerators, Spectrometers, Detectors and Associated Equipment* **509** (Aug., 2003) 151–156.

[5] J. Durst, *Modellierung und Simulation physikalischer Eigenschaften photonenzählender Röntgenpixeldetektoren für die Bildgebung*. PhD thesis, Unversität Erlangen-Nürnberg, 2008.

[6] *Radition protection instrumentation – measurement of personal dose equivalents hp(10) and hp(0.07) for x, gamma neutron and beta radiations – direct reading personal dose equivalent meters and monitors*, standard IEC 61526, International Electrotechnical Commission, 2005.

[7] *Radiation protection instrumentation – electronic counting dosemeters for pulsed fields of ionizing radiation*, standard IEC 62743, International Electrotechnical Commission, draft.

[8] Z. Vykydal, J. Jakubek, and S. Pospisil, *USB interface for Medipix2 pixel device enabling energy and position-sensitive detection of heavy charged particles*, *Nuclear Instruments and Methods in Physics Research Section A: Accelerators, Spectrometers, Detectors and Associated Equipment* **563** (July, 2006) 112–115.

[9] M. Böhnel, P. Sievers, J. Roth, G. Buchholz, O. Hupe, U. Ankerhold, T. Michel, and G. Anton, *Time resolved measurement of a pulsed X-ray source with the Timepix detector*, in *2009 IEEE Nuclear Science Symposium Conference Record (NSS/MIC)*, pp. 1682–1684, IEEE, Oct., 2009.

[10] P. Sievers, J. Klammer, T. Michel, O. Hupe, and G. Anton, *Improving the spectral resolution of a highly pixelated detector by applying a pixel-by-pixel energy calibration for investigating the spectral properties of the anode heel effect*, *Journal of Instrumentation* **7** (July, 2012) P07011–P07011.

4 Summary and outlook

The aim of the work presented here was to measure X-ray spectra with a pixelated detector. Due to effects in the sensor the spectrum cannot be measured directly and has to be calculated by a deconvolution of the measured data. In the scope of this work the deconvolution of the measured spectra could be enhanced considerably by – amongst other things – the introduction of the Bayesian deconvolution method. Those improvements opened the possibilities for further measurements.

For the measurements the detectors of the Medipix family have been used. They are nowadays used for a wide range of applications and scientific research. Their main advantage is the very high position resolution gained by a pixel pitch of 55 µm and a high number of 65 536 pixels. The Timepix detector has, in particular, two special possibilities of measurement: the Time of Arrival mode and the Time over Threshold mode. In Time of Arrival mode the arrival time of an impinging photon is measured and in Time over Threshold mode the amount of deposited charge is measured[1]. The most common method of operation is counting the number of impinging photons that release a charge higher than a preset threshold in each pixel. As this released charge is proportional to the energy deposition of the impinging photon, one can perform energy-sensitive measurements.

To perform the deconvolution of the measured energy distribution there is a need of an energy response matrix describing the detector response on radiation. For some detectors it is possible to obtain an analytic model of the response functions. Due to the high discrepancy between the impinging spectrum and the measured spectrum in case of detectors of the Medipix family, there is so far no analytic model. Thus, the detector response has to be simulated. As I could improve the precision of the measurement quite extensively, I also intended to tune the simulation with more accurate and appropriate models to gain the same level of accuracy. The results of measurement and simulation have then been compared and show a good agreement.

Up to now the measurements of impinging spectra with a Timepix detector have been performed in radiation fields with a relatively high fluence. To cope with the requirement of measuring in radiation fields with a low fluence, there had to be changes in the method of analysis compared to those performed formerly.

[1] The Time over Threshold mode was not the subject of this work.

An important improvement in this context was the employment of the Bayesian deconvolution method. The spectra reconstructed with this method were then compared to the results of two different and established detection systems. Firstly, the shape of the deconvolved spectrum was compared to the one measured with a high-purity germanium detector. Secondly, the calculated value of the kerma rate was compared to the one measured with an ionization chamber. This gave an estimate on the correctness of the absolute number of photons (deviations about 3 %). Both comparisons have shown a good agreement and thus I was able to validate that the method delivers precise results. Compared to the formerly used spectrum-stripping method the Bayesian deconvolution turned out to be very stable and reliable.

This robustness of the deconvolution method and the development of a pixel-by-pixel energy calibration were the keys towards position-resolved spectrometry. With such a precise energy calibration the energy resolution was enhanced by up to 45 %. This improved accuracy in the measurement has been very demanding on the improvements of the simulation of the response matrix needed for deconvolution. Both this enhanced simulation and a pixel-by-pixel calibrated detector opened the possibility of measuring the anode heel effect. Not only the relative angular dependency of the spectrum emitted but also the change in the absolute photon fluence were measured. Furthermore, it is possible to even use small regions of interest down to 4 x 4 pixels to evaluate a spectrum. This was then applied for the spectrometry of small focal spots of a miniature X-ray source used in therapeutics.

Furthermore, the robustness and the stability of the applied Bayesian deconvolution method enabled the possibility of performing time-resolved spectrometric measurements. By measuring in Time of Arrival mode and in parallel performing a threshold scan, it is possible to gain information on both energy and time. This method was then tested for a conventional X-ray tube for measuring the time dependence of the spectrum emitted during the switching-on process of the radiation (the rise time of the HV). As expected, the results showed a relatively long time-dependent change of the spectrum. This method was then applied for proving that a newly developed X-ray source shows a spectral change of the spectrum emitted on a very low time scale only. As this time dependence is much shorter compared to the total pulse duration of the radiation, it is negligible. This result guarantees that both pulse duration and energy can be adjusted independently. This enables further investigations with this new X-ray tube in the field of pulsed radiation and its use for e.g. type tests.

Possible applications of the work presented here are given in the field of quality assurance of X-ray sources. A more sophisticated application would be given in the field of X-ray fluorescence spectrometric imaging as has been described in [OI+11]. Additionally, Bayesian deconvolution opens the possibility of investigations on energy resolved interferometric X-ray imaging. In this context first measurements have been performed to investigate the energy dependence of the so-called darkfield image over a wide energy range [Pel12]. For all those applications – especially for medical imaging – a lower measuring time needed for performing spectrometric measurements is preferable. A promising approach in this direction is the dosepix detector [Böh12; Won12] which is able to measure in 16 energy channels in parallel in each pixel. One should note that the overall dimensions of this detector are 3.5 mm x 3.5 mm and thus one single detector is probably to small for imaging applications. Finally, the methods and results presented here may find their way into the development of new detectors for spectrometric imaging.

Zusammenfassung und Ausblick

Das Ziel der hier vorgestellten Arbeit war, Röntgenspektren mit einem pixelierten Detektor zu messen. Aufgrund von Effekten im Sensor kann das Spektrum nicht direkt gemessen werden und muss deshalb durch Entfaltung der gemessenen Daten berechnet werden. Im Rahmen dieser Arbeit konnte, unter anderem durch die Einführung der Bayes'schen Entfaltungsmethode, die Entfaltung der gemessenen Spektren deutlich verbessert werden. Diese Verbesserungen ermöglichten eine Reihe von Messungen.

Für die Messungen kamen die Detektoren der Medipix-Familie zum Einsatz. Diese werden heutzutage in einem breiten Anwendungsfeld und für wissenschaftliche Forschungen eingesetzt. Ihr größter Vorteil ist die hohe Ortsauflösung, die durch die geringe Pixelgröße von 55 µm, sowie durch die große Anzahl von 65 536 Pixeln erreicht wird. Der Timepix-Detektor hat im speziellen noch zwei zusätzliche Betriebsmodi: den Time of Arrival Modus und den Time over Threshold Modus. Im Time of Arrival Modus wird die Ankunftszeit eines einfallenden Photons gemessen und im Time over Threshold Modus[2] die im Sensor deponierte Ladung. Im Standardbetriebsmodus wird im Pixel die Anzahl an Photonen, deren deponierte Ladung eine voreingestellte Schwelle überschreitet, gezählt. Die im Sensor deponierte Ladung ist abhängig von der Energie des einfallenden Photons. Dies eröffnet Möglichkeiten für energieaufgelöste Messungen.

Zur Durchführung der Entfaltung der gemessenen Energieverteilung wird eine Energieantwortmatrix, welche die Detektorantwort auf Bestrahlung beschreibt, benötigt. Für einige Detektoren ist es möglich ein analytisches Modell der Detektorantwort aufzustellen. Aufgrund der großen Diskrepanz zwischen einfallendem und gemessenem Spektrum für die Detektoren der Medipix-Familie, gibt es für sie bislang jedoch kein solches analytisches Modell. Aus diesem Grund muss die Detektorantwort simuliert werden. Da im Rahmen dieser Arbeit die Präzision der Messungen stark verbessert werden konnte, beabsichtigte ich auch die Simulation mit genaueren und angepassten Modellen auf ein gleichwertiges Niveau zu bringen. Die vorgestellten Ergebnisse von Simulation und Messungen zeigen im direkten Vergleich eine gute Übereinstimmung.

Bis jetzt wurden die Messungen des einfallenden Spektrums mit dem Timepix-Detektor in Photonenfeldern mit einer verhältnismäßig hohen Fluenz durchgeführt. Um auch den Messbedingungen für Photonenfelder mit niedrigem Fluss

[2] Der Time over Threshold Modus war nicht Bestandteil dieser Arbeit.

gerecht zu werden, musste es einige Änderungen in Bezug auf die Methodik der bislang durchgeführten Analysen geben. In dieser Hinsicht war die Einführung der Bayes'schen Entfaltungsmethode eine wichtige Verbesserung. Die mit dieser Methode rekonstruierten Spektren wurden mit den Ergebnissen zweier anderer etablierter Detektoren verglichen. Zuerst wurde die Form des entfalteten Spektrums mit dem Messergebnis eines hochreinen Germaniumdetektors verglichen. Weiter wurde die aus dem entfalteten Spektrum berechnete Luftkerma mit der direkten Messung durch eine Ionisationskammer verglichen. Hieraus konnte ein Eindruck über die korrekte Bestimmung der absoluten Photonenanzahl (Abweichung ca. 3 %) gewonnen werden. Beide Vergleiche zeigten eine gute Übereinstimmung, so dass es mir möglich war, die Präzision der durch die neue Methode gewonnenen Ergebnisse zu validieren. Im Vergleich zur bislang genutzten Spektrum-Stripping-Methode stellte sich die Bayes'sche Entfaltung als sehr stabil und verlässlich heraus.

Die Stabilität der Entfaltung und die Entwicklung einer pixelweisen Energiekalibration waren der Schlüssel zur ortsaufgelösten Spektrometrie. Mit dieser präzisen Energiekalibration konnte die Energieauflösung um bis zu 45 % verbessert werden. Die verbesserte Genauigkeit der Messung stellte eine große Anforderung an die Verbesserung der Simulation zur Gewinnung der Detektorantwortmatrix dar. Beides, die verbesserte Simulation als auch der pixelweise kalibrierte Detektor, eröffneten die Möglichkeit zur Messung des Heel-Effekts. Somit konnte nicht nur die winkelabhängige relative Änderung des emittierten Spektrums gemessen werden, sondern auch die Änderung der absoluten Photonenfluenz. Weiterhin war es nun möglich, kleine Detektorbereiche von bis zu 4 x 4 Pixel für die Bestimmung des Spektrums zu nutzen. Dies fand Anwendung bei der Spektrometrie kleiner Brennpunkte einer therapeutischen Miniaturröntgenquelle.

Weiterhin eröffnete die Stabilität der verwendeten Bayes'schen Entfaltung die Möglichkeit zur Durchführung zeitaufgelöster spektrometrischer Messungen. Bei Messungen im Time of Arrival Modus und einem parallel dazu durchgeführten Schwellen Scan ist es möglich sowohl eine Zeit- als auch eine Energieinformation zu erhalten. Diese Methode wurde an einer konventionellen Röntgenröhre getestet. Es wurde die zeitliche Änderung des emittierten Spektrums während des Einschaltvorgangs der Röntgenröhre (dem Hochfahren der Hochspannung) gemessen. Die Messung ergab, wie erwartet, eine relativ lange zeitabhängige Änderung des Spektrums. Diese Methode wurde daraufhin genutzt, um zu zeigen, dass das emittierte Spektrum einer neu entwickelten Röntgenröhre nur eine minimale Zeitabhängigkeit zeigt. Da diese Zeiten verglichen mit der Pulslänge klein sind, können sie vernachlässigt werden. Diese Ergebnisse garantieren, dass sowohl Energie (bzw. die Hochspannung) als auch die Pulslänge unabhängig

voneinander eingestellt werden können. Dies ermöglicht es, mit dieser Anlage definierte Untersuchungen im Bereich gepulster Strahlung durchzuführen und sie für z.B. Bauartprüfungen einzusetzen.

Mögliche Anwendung können die hier vorgestellten Ergebnisse im Bereich der Qualitätssicherung für Röntgenröhren finden. Eine anspruchsvollere Anwendung liegt im Bereich der spektrometrischen Röntgenfluoreszenz-Bildgebung, wie sie in [OI+11] beschrieben ist. Zusätzlich eröffnet die Bayes'sche Entfaltung die Möglichkeiten zu Untersuchungen der Energieabhängigkeiten in der interferometrischen Röntgenbildgebung. In diesem Zusammenhang wurden erste Messungen zur Untersuchung der Energieabhängigkeit des so genannten Dunkelfeld-Bildes durchgeführt [Pel12]. Für all diese Anwendungen – speziell im Bereich der medizinischen Bildgebung – wäre eine geringere Messzeit zur Durchführung der spektrometrischen Messungen wünschenswert. Als eine erfolgversprechende Entwicklung diesbezüglich sei der Dosepix-Detektor [Böh12; Won12] erwähnt. Mit diesem ist es möglich in jedem Pixel zeitgleich in 16 Energiekanälen zu messen. Zu bemerken bleibt, dass die Sensorfläche dieses Detektors nur 3.5 mm x 3.5 mm beträgt, so dass ein einzelner Detektor für die Bildgebung vermutlich zu klein ist. Schließlich können die hier präsentierten Methoden und Ergebnisse Anwendung finden in der Entwicklung neuer Detektoren für die spektrometrische Bildgebung.

A Tabulated Values

Parameter	Value
Number of pixels	256 x 256
Pixel pitch	55 µm
Modes of operation	counting
	Time over Threshold (ToT)
	ToA
Clock frequency	10 MHz to 100 MHz

Table A.1 Summary of the technical data of the Timepix ASIC [LB+07].

Parameter	Value
Sensor material	silicon (Si)
Sensor area	15.2 mm^2
	effectively 14.08 mm^2
Sensor thickness	303 µm
	effectively 297.4 µm
Width of guard ring	560 µm
Height of passivation layers	2 x 2.8 µm
Collected charge carrier	e^-

Table A.2 Summary of the technical data of the Timepix sensor ([LB+07] and private communication with chip designers at CERN).

Parameter	Value	Reference
Temperature	$T = 297\,\mathrm{K}$	
Depletion voltage	$U_{\mathrm{depletion}} = 25\,\mathrm{V}$	CERN
Relative permittivity	$\epsilon_r = 11.9$	[Sze81]
Pair energy	$3.62\,\mathrm{eV}$	[DCGW06]
Fano factor	0.06	[DCGW06]
Density	$2.33\,\mathrm{g\,cm^{-3}}$	[DCGW06]
Mobility of holes	$\mu_h = 450\,\mathrm{cm^2/(Vs)}$	[Sze81]
Diffusion of holes	$D_h = K_B \cdot T \cdot \mu_h$	[Sze81]
Max. velocity of holes	$v_{h,\mathrm{max}} = 1.62 \times 10^6\,\mathrm{m\,s^{-1}} \cdot \left(\frac{T}{1\,\mathrm{K}}\right)^{-0.52}$	[JCOA77]
Velocity exponent β	$\beta_h = 0.46 \cdot \left(\frac{T}{1\,\mathrm{K}}\right)^{0.17}$	[JCOA77]
Mobility of electrons	$\mu_{e^-} = 1350\,\mathrm{cm^2/(Vs)}$	[Dur08]
Diffusion of electrons	$D_{e^-} = K_B \cdot T \cdot \mu_{e^-}$	[Sze81]
Max. velocity of electrons	$v_{e^-,\mathrm{max}} = 1.53 \times 10^7\,\mathrm{m\,s^{-1}} \cdot \left(\frac{T}{1\,\mathrm{K}}\right)^{-0.87}$	[JCOA77]
Velocity exponent β	$\beta_{e^-} = 2.52 \times 10^{-2} \cdot \left(\frac{T}{1\,\mathrm{K}}\right)^{0.66}$	[JCOA77]

Table A.3 Properties of the Si sensor implemented in the simulation. The lifetime of the charge carriers has not been taken into account as they are orders longer than the maximal drift time.

B Source code

Source code B.1 Bump-bond class

```
1 BumpBond::BumpBond() : CompositeMedium() {
2    const double spacing= (0.01 mum);
3    const double Bump_bbDia = (35.48 mum);
4
5    const double Bump_ASICside_height = (6.28 mum);
6    const double Bump_SensorSide_height = (9.41 mum);
7    const double Bump_height = Bump_ASICside_height+
        Bump_SensorSide_height;
8    const double UBM_Sensor_height = (5.37 mum);
9    const double UBM_Sensor_Dia = (30.26 mum);
10   const double UBM_ASIC_height = (6.26 mum);
11   const double UBM_ASIC_Dia = (30.26 mum);
12   this->setKECutOff(0.1 * 1e-6); // 0.1 keV
13   this->setTitle("Perl");
14   this->setMaterial(Material::hatch("vacuum"));
15   _BumpSetupHeight = UBM_Sensor_height+ spacing +
        Bump_height +spacing + UBM_ASIC_height;
16   this->setVolume(new Box(54 mum, 54 mum, _BumpSetupHeight))
        ;
17
18   CompositeMedium *UBM_Sensor;
19   UBM_Sensor = new CompositeMedium();
20   UBM_Sensor->setKECutOff(0.1 * 1e-6); //0.1 keV
21   UBM_Sensor->setTitle("PartOfASIC");
22   UBM_Sensor->setMaterial(Material::hatch("Ni"));
23   UBM_Sensor->setVolume(new Tube(UBM_Sensor_height, 0,
        UBM_Sensor_Dia / 2.0));
24      Medium *UBM_Sensor2;
25      UBM_Sensor2 = new Medium();
26      UBM_Sensor2->setKECutOff(0.1 * 1e-6); //0.1 keV
27      UBM_Sensor2->setTitle("PartOfASIC");
28      UBM_Sensor2->setMaterial(Material::hatch("Cu"));
29      UBM_Sensor2->setVolume(new Tube(0.2 mum , 0,
           UBM_Sensor_Dia / 2.0));
30      UBM_Sensor2->move(Vector(0, 0, (UBM_Sensor_height -0.2
           mum) / 2.0));
31      UBM_Sensor->addMedium(UBM_Sensor2);
32   UBM_Sensor->move(Vector(0, 0, (UBM_Sensor_height -
        _BumpSetupHeight) / 2.0));
33   this->addMedium(UBM_Sensor);
34
```

```
35     Medium *Bumps;
36     Bumps = new Medium();
37     Bumps->setKECutOff(0.1 * 1e-6); // 0.1 keV
38     Bumps->setTitle("Perl");
39     Bumps->setMaterial(Material::hatch("Sn96.5Ag03.5"));
40     Bumps->setVolume(new SphereSlice(0, Bump_bbDia / 2,
           Bump_ASICside_height , Bump_SensorSide_height));
41     Bumps->move(Vector(0, 0, (Bump_SensorSide_height-
           Bump_ASICside_height)/2.0));
42     Bumps->move(Vector(0, 0, (_BumpSetupHeight-Bump_height) /
           2.0-UBM_ASIC_height-spacing));
43     this->addMedium(Bumps);
44
45     Medium *UBM_ASIC;
46     UBM_ASIC = new Medium();
47     UBM_ASIC->setKECutOff(0.1 * 1e-6); //0.1 keV
48     UBM_ASIC->setTitle("PartOfASIC");
49     UBM_ASIC->setMaterial(Material::hatch("Cu"));
50     UBM_ASIC->setVolume(new Tube(UBM_ASIC_height, 0,
           UBM_ASIC_Dia / 2.0));
51     UBM_ASIC->move(Vector(0, 0, (_BumpSetupHeight-
           UBM_ASIC_height) / 2.0));
52     this->addMedium(UBM_ASIC);
53 }
```

Source code B.2 Iteration step of Bayesian deconvolution

```
1 for (iter = 1; stopping_condition(chi_square, max_chisquare,
      iter, max_iter, error_counter); iter++) {
2     { //iteration step
3         gsl_vector_memcpy(measured_temp, measured);
4         gsl_vector_div_special(measured_temp, measured_virt);
5         gsl_blas_dgemv(CblasTrans, 1.0, R, measured_temp, 0.0,
              impinging);
6         gsl_vector_mul(impinging, impinging_old);
7         gsl_vector_div(impinging, efficiency);
8         gsl_vector_memcpy(impinging_old, impinging);
9         gsl_blas_dgemv(CblasNoTrans, 1.0, R, impinging, 0.0,
              measured_virt);
10    } //iteration step - end
11
12    { //error/chi^2 - calculation
13        calc_chi_square(measured_virt, measured,
              measured_used_counts_gesamterror, chi_square,
              error_counter);
14        chi_square = sqrt(chi_square / anz_zeilen);
15    }
16
17
18    if (chi_square <= max_chisquare) {
19        std::cout << "\t" << iter << " Chi^2: " << chi_square
              << " , errors: " << error_counter << " ,\tStop:
              chi_square" << std::endl;
20    } else if (error_counter == 1.0) {
21        std::cout << "\t" << iter << " Chi^2: " << chi_square
              << " , errors: " << error_counter << " ,\tStop
              error_counter" << std::endl;
22    } else if (iter == max_iter) {
23        std::cout << "\t" << iter << " Chi^2: " << chi_square
              << " , errors: " << error_counter << " ,\tStop
              max_iter" << std::endl;
24    }
25 }
```

Bibliography

[AB99] Ulrike Ankerhold and Rolf Behrens. 'X Ray Spectrometry of Low Energy Photons for Determining Conversion Coefficients from Air Kerma, Ka, to Personal Dose Equivalent, Hp (10), for Radiation Qualities'. In: *Radiation Protection Dosimetry* 81.4 (1999), pp. 247–258.

[Ank00] Ulrike Ankerhold. *Catalogue of X-ray spectra and their characteristic data - ISO and DIN radiation qualities, therapy and diagnostic radiation qualities, unfiltered X-ray spectra*. Wirtschaftsverlag N. W. Verlag für neue Wissenschaft, 2000, p. 124.

[Ans] *American National Standard for Portable Radiation Detection Instrumentation for Homeland Security*. standard ANSI N42.33. 2007.

[BA+98] A Brinkman, H Aarts et al. 'The Reflection Grating Spectrometer on board XMM'. In: *Proceedings of the First XMM Workshop: Science with XMM*. 1998, pp. 1–23.

[BB93] Cliff Bueno and Marion D. Barker. 'High-resolution digital radiography and three-dimensional computed tomography'. In: *Proceedings of SPIE*. Vol. 2009. 1993. SPIE, 1993, pp. 179–191. DOI: 10.1117/12.164737.

[Bfs03] Bundesamt für Strahlenschutz. *Jahresbericht 2003*. Tech. rep. 2003, p. 68.

[BP63] Thomas Bayes and Richard Price. 'An Essay towards Solving a Problem in the Doctrine of Chances. By the Late Rev. Mr. Bayes, F. R. S. Communicated by Mr. Price, in a Letter to John Canton, A. M. F. R. S.' In: *Philosophical Transactions of the Royal Society of London* 53 (Jan. 1763), pp. 370–418. DOI: 10.1098/rstl.1763.0053.

[BS+09] Michael Böhnel, Peter Sievers et al. 'Time resolved measurement of a pulsed X-ray source with the Timepix detector'. In: *2009 IEEE Nuclear Science Symposium Conference Record (NSS/MIC)*. IEEE, Oct. 2009, pp. 1682–1684. DOI: 10.1109/NSSMIC.2009.5402234.

[Böh12] Michael Böhnel. 'Evaluierung und Entwicklung von Röntgendetektoren für die Dosimetrie'. PhD thesis. Unversität Erlangen-Nürnberg, 2012, p. 217.

[Büe] Ludwig Büermann. *Calibration of secondary standards*. retrieved from URL: http://www.ptb.de/en/org/6/62/625/kalibrierung.htm (visited on 21/11/2011).

[Cam11] Michael Campbell. '10 years of the Medipix2 Collaboration'. In: *Nuclear Instruments and Methods in Physics Research Section A: Accelerators, Spectrometers, Detectors and Associated Equipment* 633 (May 2011), S1–S10. DOI: 10.1016/j.nima.2010.06.106.

[DCGW06] R. Devanathan, L.R. Corrales, F. Gao and W.J. Weber. 'Signal variance in gamma-ray detectors – A review'. In: *Nuclear Instruments and Methods in Physics Research Section A: Accelerators, Spectrometers, Detectors and Associated Equipment* 565.2 (Sept. 2006), pp. 637–649. DOI: 10.1016/j.nima.2006.05.085.

[Dur08] Jürgen Durst. 'Modellierung und Simulation physikalischer Eigenschaften photonenzählender Röntgenpixeldetektoren für die Bildgebung'. German. PhD thesis. Unversität Erlangen-Nürnberg, 2008, p. 152.

[D'A95] G D'Agostini. 'A multidimensional unfolding method based on Bayes' theorem'. In: *Nuclear Instruments and Methods in Physics Research Section A: Accelerators, Spectrometers, Detectors and Associated Equipment* 362.2-3 (Aug. 1995), pp. 487–498. DOI: 10.1016/0168-9002(95)00274-X.

[FA70] R. S. Frankel and D. W. Aitken. 'Energy-Dispersive X-Ray Emission Spectroscopy'. In: *Applied Spectroscopy* 24.6 (Nov. 1970), pp. 557–566. DOI: 10.1366/000370270774372308.

[GD08] Jürgen Giersch and Jürgen Durst. 'Monte Carlo simulations in X-ray imaging'. In: *Nuclear Instruments and Methods in Physics Research Section A: Accelerators, Spectrometers, Detectors and Associated Equipment* 591.1 (June 2008), pp. 300–305. DOI: 10.1016/j.nima.2008.03.078.

[GD+11] Ewald Guni, Jürgen Durst et al. 'The Influence of Pixel Pitch and Electrode Pad Size on the Spectroscopic Performance of a Photon Counting Pixel Detector With CdTe Sensor'. In: *IEEE Transactions on Nuclear Science* 58.1 (Feb. 2011), pp. 17–25. DOI: 10.1109/TNS.2010.2095883.

[Gie] Jürgen Giersch. *ROentgen SImulation ROSI*. retrieved from URL: http://www.pi4.nat.uni-erlangen.de/Giersch/ROSI/index.html (visited on 15/06/2012).

[GWA03] Jürgen Giersch, Andreas Weidemann and Gisela Anton. 'ROSI – an object-oriented and parallel-computing Monte Carlo simulation for X-ray imaging'. In: *Nuclear Instruments and Methods in Physics Research Section A: Accelerators, Spectrometers, Detectors and Associated Equipment* 509.1-3 (Aug. 2003), pp. 151–156. DOI: 10.1016/S0168-9002(03)01564-X.

[ICRU57] *Conversion Coefficients for use in Radiological Protection against External Radiation*. ICRU Report. 1994.

[Iso] *X and gamma reference radiation for calibrating dosemeters and doserate meters and for determining their response as a function of photon energy – Part 1: Radiation characteristics and production methods*. standard ISO 4037-1. 1996.

[JCOA77] C Jacoboni, C Canali, G. Ottaviani and A. Alberigi Quaranta. 'A review of some charge transport properties of silicon'. In: *Solid-State Electronics* 20.2 (Feb. 1977), pp. 77–89. DOI: 10.1016/0038-1101(77)90054-5.

[KDMA08] Björn Kreisler, Jürgen Durst, Thilo Michel and Gisela Anton. 'Generalised adjoint simulation of induced signals in semiconductor X-ray pixel detectors'. In: *Journal of Instrumentation* 3.11 (Nov. 2008), P11002–P11002. DOI: 10.1088/1748-0221/3/11/P11002.

[Kha11] Mayeen Uddin Khandaker. 'High purity germanium detector in gamma-ray spectrometry'. In: *International Journal of Fundamental Physical Sciences* 1.2 (2011), pp. 42–46.

[Kor07] Alexander Korn. 'Spektrale und bildgebende Eigenschaften photonenzählender Röntgendetektoren am Beispiel des Medipix-Detektors'. German. PhD thesis. Unversität Erlangen-Nürnberg, 2007, p. 127.

[KPR78] T Kennett, W Prestwich and A Robertson. 'Bayesian deconvolution I: Convergent properties'. In: *Nuclear Instruments and Methods* 151.1-2 (May 1978), pp. 285–292. DOI: 10.1016/0029-554X(78)90502-5.

[KRH12] Jana Klammer, Jürgen Roth and Oliver Hupe. 'Novel reference radiation fields for pulsed photon radiation installed at PTB'. In: *Radiation Protection Dosimetry* (Apr. 2012), pp. 1–5. DOI: 10.1093/rpd/ncs043.

[LB+07] Xavier Llopart, R. Ballabriga et al. 'Timepix, a 65k programmable pixel readout chip for arrival time, energy and/or photon counting measurements'. In: *Nuclear Instruments and Methods in Physics Research Section A: Accelerators, Spectrometers, Detectors and Associated Equipment* 581.1-2 (Oct. 2007), pp. 485–494. DOI: 10.1016/j.nima.2007.08.079.

[LC+02] Xavier Llopart, Michael Campbell et al. 'Medipix2: A 64-k pixel readout chip with 55-μm square elements working in single photon counting mode'. In: *IEEE Transactions on Nuclear Science* 49.5 (Oct. 2002), pp. 2279–2283. DOI: 10.1109/TNS.2002.803788.

[LE+96] Peter Lechner, Stefan Eckbauer et al. 'Silicon drift detectors for high resolution room temperature X-ray spectroscopy'. In: *Nuclear Instruments and Methods in Physics Research Section A: Accelerators, Spectrometers, Detectors and Associated Equipment* 377.2-3 (Aug. 1996), pp. 346–351. DOI: 10.1016/0168-9002(96)00210-0.

[LP+08] Derek Liu, Emily Poon et al. 'Spectroscopic characterization of a novel electronic brachytherapy system.' In: *Physics in medicine and biology* 53.1 (Jan. 2008), pp. 61–75. DOI: 10.1088/0031-9155/53/1/004.

[MA+06] Thilo Michel, Gisela Anton et al. 'A fundamental method to determine the signal-to-noise ratio (SNR) and detective quantum efficiency (DQE) for a photon counting pixel detector'. In: *Nuclear Instruments and Methods in Physics Research Section A: Accelerators, Spectrometers, Detectors and Associated Equipment* 568.2 (Dec. 2006), pp. 799–802. DOI: 10.1016/j.nima.2006.08.115.

[MB+09] Thilo Michel, Michael Böhnel et al. 'Low Energy Dosimetry With Photon Counting Pixel Detectors Such as Medipix'. In: *IEEE Transactions on Nuclear Science* 56.2 (Apr. 2009), pp. 417–423. DOI: 10.1109/TNS.2009.2015229.

[Med] Medipix Collaboration. *Medipix homepage*. retrieved from URL: http://medipix.web.cern.ch (visited on 15/08/2012).

[Mos03] M. Moszyński. 'Inorganic scintillation detectors in γ-ray spectrometry'. In: *Nuclear Instruments and Methods in Physics Research Section A: Accelerators, Spectrometers, Detectors and Associated Equipment* 505.1-2 (June 2003), pp. 101–110. DOI: 10.1016/S0168-9002(03)01030-1.

[MTT+09] Thilo Michel, Patrick Takoukam-Talla et al. 'Reconstruction of X-ray spectra with the energy sensitive photon counting detector Medipix2'. In: *Nuclear Instruments and Methods in Physics Research Section A: Accelerators, Spectrometers, Detectors and Associated Equipment* 598.2 (Jan. 2009), pp. 510–514. DOI: 10.1016/j.nima.2008.09.049.

[NH00] Y. Namito and H. Hirayama. *LSCAT: Low-Energy Photon-Scattering Expansion for the EGS4 Code (Inclusion of Electron Impact Ionization)*. Tech. rep. High Energy Accelerator Research Organization (KEK), 2000.

[NHR85] Walter R. Nelson, Hideo Hirayamal and David W.O. Rogers. *THE EGS4 CODE SYSTEM*. Tech. rep. Stanford: SLAC National Accelerator Laboratory, 1985, p. 398.

[OI+11] I. Ordavo, S. Ihle et al. 'A new pnCCD-based color X-ray camera for fast spatial and energy-resolved measurements'. In: *Nuclear Instruments and Methods in Physics Research Section A: Accelerators, Spectrometers, Detectors and Associated Equipment* 654.1 (Oct. 2011), pp. 250–257. DOI: 10.1016/j.nima.2011.05.080.

[Ort] Ortec. *Ortec Homepage*. retrieved from URL: http://www.ortec-online.com/Solutions/RadiationDetectors/semiconductor-photon-detectors.aspx (visited on 17/07/2012).

[Pel12] Georg Pelzer. 'Experimente und Simulationen zur Steigerung der Bildqualität in der Phasenkontrast-Röntgenbildgebung'. Master's thesis. Universität Erlangen-Nürnberg, 2012.

[Pod10] Ervin B. Podgorsak. *Radiation Physics for Medical Physicists*. 2nd. Biological and Medical Physics, Biomedical Engineering. Berlin, Heidelberg: Springer Berlin Heidelberg, 2010, p. 745. DOI: 10.1007/978-3-642-00875-7.

[RS92] M Richter and P Siffert. 'High resolution gamma ray spectroscopy with CdTe detector systems'. In: *Nuclear Instruments and Methods in Physics Research Section A: Accelerators, Spectrometers, Detectors and Associated Equipment* 322.3 (Nov. 1992), pp. 529–537. DOI: 10.1016/0168-9002(92)91227-Z.

[SA+10] Peter Sievers, Ulrike Ankerhold et al. 'Charakterisierung einer Miniatur-Röntgenröhre mit dem Medipix2-Detektor'. In: *Medizinische Physik 2010*. Ed. by Norbert Hodapp, Jürgen Hennig and Michael Mix. 2010, pp. 496–497.

[SK+12a] Peter Sievers, Jana Klammer et al. 'Improving the spectral resolution of a highly pixelated detector by applying a pixel-by-pixel energy calibration for investigating the spectral properties of the anode heel effect'. In: *Journal of Instrumentation* 7.07 (July 2012). DOI: 10.1088/1748-0221/7/07/P07011.

[SK+12b] Peter Sievers, Jana Klammer et al. 'Time-resolved spectrometry for the characterization of a reference field for pulsed radiation'. In: *Journal of Instrumentation* (Manuscript accepted for publication).

[SSMA11] Peter Sievers, Thorsten Schneider, Thilo Michel and Gisela Anton. 'X-ray spectroscopy with photon counting imaging detectors such as Timepix'. In: *2011 IEEE Nuclear Science Symposium Conference Record*. IEEE, Oct. 2011, pp. 1826–1828. DOI: 10.1109/NSSMIC.2011.6154692.

[SW+12a] Peter Sievers, Thomas Weber et al. 'Bayesian deconvolution as a method for the spectroscopy of X-rays with highly pixelated photon counting detectors'. In: *Journal of Instrumentation* 7.03 (Mar. 2012). DOI: 10.1088/1748-0221/7/03/P03003.

[SW+12b] Peter Sievers, Thomas Weber et al. 'Erratum: Bayesian deconvolution as a method for the spectroscopy of X-rays with highly pixelated photon counting detectors'. In: *Journal of Instrumentation* 7.08 (Aug. 2012). DOI: 10.1088/1748-0221/7/08/E08001.

[Sze81] S.M. Sze. *Physics of Semiconductor Devices*. 2nd. Wiley-Interscience, 1981, p. 868.

[TT11] Patrick Takoukam-Talla. 'Investigation of photon counting pixel detectors for X-ray spectroscopy and imaging'. PhD thesis. Universität Erlangen-Nürnberg, 2011, p. 150.

[TTM+09] Patrick Takoukam-Talla, Thilo Michel et al. 'Exploiting the MEDIPIX2 detector for the reconstruction of X-ray spectra'. In: *Nuclear Instruments and Methods in Physics Research Section A: Accelerators, Spectrometers, Detectors and Associated Equipment* 607.1 (Aug. 2009), pp. 103–106. DOI: 10.1016/j.nima.2009.03.138.

[UHJ10] J. Uher, G. Harvey and Jan Jakubek. 'X-ray fluorescence imaging with the Medipix2 single-photon counting detector'. In: *IEEE Nuclear Science Symposium & Medical Imaging Conference*. IEEE, Oct. 2010, pp. 1067–1073. DOI: 10.1109/NSSMIC.2010.5873930.

[VJP06] Zdenek Vykydal, Jan Jakubek and Stanislav Pospisil. 'USB interface for Medipix2 pixel device enabling energy and position-sensitive detection of heavy charged particles'. In: *Nuclear Instruments and Methods in Physics Research Section A: Accelerators, Spectrometers, Detectors and Associated Equipment* 563.1 (July 2006), pp. 112–115. DOI: 10.1016/j.nima.2006.01.114.

[WA+11] Winnie Sze-Wing Wong, Gisela Anton et al. 'A pixel detector asic for dosimetry using time-over-threshold energy measurements'. In: *Radiation Measurements* 46.12 (Dec. 2011), pp. 1619–1623. DOI: 10.1016/j.radmeas.2011.06.061.

[Won12] Winnie Sze-Wing Wong. 'A Hybrid Pixel Detector ASIC with Energy Binning for Real-Time, Spectroscopic Dose Measurements'. PhD thesis. Mid Sweden University, 2012, p. 170.

[Xof] Xoft. *Xoft Homepage*. retrieved from URL: http://www.xoftinc.com/products_hdrsource.html (visited on 29/07/2012).

[Zei] Zeiss. *Zeiss Homepage*. retrieved from URL: `http://www.meditec.zeiss.com/C1256CAC0038CEFF/ContainerTitel/Intrabeam/\$File/healthcare3.html` (visited on 25/06/2012).

Danksagung

Am Ende dieser Arbeit möchte ich die Gelegenheit nutzen und mich an dieser Stelle bei den vielen Personen, die mir in den letzten Jahren und speziell im Rahmen meiner Dissertation zur Seite standen, bedanken. Wenngleich die folgende Liste nie vollständig sein kann, so ergeht doch ein herzliches Dankeschön an:

- Die Physikalisch-Technische Bundesanstalt (PTB) und das Erlangen Centre for Astroparticle Physics für die interessante Themenstellung und insbesondere an die PTB für die Finanzierung meiner Stelle.
- Prof. Dr. Gisela Anton für eine sehr gute und angenehme Betreuung der Arbeit, Dr. Thilo Michel für die vielen fachlichen Diskussionen und auch für all die anderen Gespräche, Dr. Jürgen Durst für die große Hilfe bei all den programmiertechnischen Fragen – insbesondere zu Fragen der Simulation.
- Die Kollegen der PTB aus den Fachbereichen 6.3 und 6.2: Dr. Peter Ambrosi, Dr. Ulrike Ankerhold, Sabrina Balg, Dr. Rolf Behrens, Carolyn Eckerleben, Christian Fuhg, Dr. Oliver Hupe, Dieter Jahns, Simone Janssen, Patrik Kramer, Dr. Jana Klammer, Andreas Lachmann, Markus Meier, Jürgen Roth, Dr. Thorsten Schneider und Dr. Hayo Zutz (in alphabetischer Reihenfolge). Herzlichen Dank für die angenehme und erfolgreiche Zusammenarbeit.
- Die RaDphys-Gruppe incl. Ehemaligen: Peter Bartl, Florian Bayer, Benedikt Bergmann, Michael Böhnel, Mykhaylo Filipenko, Thomas Gabor, Ulrike Gebert, Thomas Gleixner, Ewald Guni, Wilhelm Haas, Björn Kreisler, Georg Pelzer, Jens Rieger, André Ritter, Ina Ritter, Tilman Rügheimer, Patrik Takoukam, Thomas Weber und Andrea Zhang (in alphabetischer Reihenfolge). Vielen Dank für die vielen fachlichen und außerfachlichen Gespräche und für die schöne Zeit innerhalb und außerhalb des Instituts.
- Die Medipix/Timepix-Entwickler am CERN für die gute Zusammenarbeit.
- Die Mitarbeiter der Werkstätten für die kompetente und hilfsbereite Bearbeitung meiner Anfragen und Aufträge.
- Alle meine Mitstudenten der letzten Jahre, vor allem Edmund Menge, Hans Knörr, Nicolai Granzow und Kathrin Nowak, die mir während der Studienzeit sehr gute Freunde waren und immer noch sind.
- Meine Familie und besonders meine Eltern, die mich jederzeit unterstützen.

— Danke —